Samples Collected from the Floor of Jezero Crater with the Mars 2020 Perseverance Rover

J. I. Simon[1*], K. Hickman-Lewis[2,3], B. A. Cohen[4], L.E. Mayhew[5], D.L. Shuster[6], V. Debaille[7], E. M. Hausrath[8], B.P. Weiss[9], T. Bosak[9], M.-P. Zorzano[10], H. E. F. Amundsen[11], L.W. Beegle[12]†, J.F. Bell III[13], K. C. Benison[14], E. L. Berger[15], O. Beyssac[16], A.J. Brown[17], F. Calef[12], T. M. Casademont[11], B. Clark[18], E. Clavé[19], L. Crumpler[20], A. D. Czaja[21], A. G. Fairén[10,22], K. A. Farley[23], D. T. Flannery[24], T. Fornaro[25], O. Forni[26], F. Gómez[10], Y. Goreva[12], A. Gorin[7], K. P. Hand[12], S.-E. Hamran[11], J. Henneke[27], C. D. K. Herd[28], B. H. N. Horgan[29], J. R. Johnson[30], J. Joseph[31], R. E. Kronyak[12], J. M. Madariaga[32], J. N. Maki[12], L. Mandon[33], F. M. McCubbin[34], S. M. McLennan[35], R. C. Moeller[12], C. E. Newman[36], J. I. Núñez[29], A. C. Pascuzzo[37], D. A. Pedersen[28], G. Poggiali[38], P. Pinet[26], C. Quantin-Nataf[39], M. Rice[40], J. W. Rice Jr.[13], C. Royer[19], M. Schmidt[41], M. Sephton[42], S. Sharma[12], S. Siljeström[43], K. M. Stack[12], A. Steele[44], V. Z. Sun[12], A. Udry[8], S. VanBommel[45], M. Wadhwa[12,13], R. C. Wiens[29], A. J. Williams[46], K. H. Williford[47]

[1]Center for Isotope Cosmochemistry and Geochronology, Astromaterials Research and Exploration Science, NASA Johnson Space Center, Houston, TX, USA.
[2]The Natural History Museum, London, UK.
[3]Dipartimento BiGeA, Università di Bologna, Bologna, Italy.
[4]NASA Goddard Space Flight Center, Greenbelt, MD, USA.
[5]University of Colorado Boulder, Dept. of Geological Sciences, Boulder, CO, USA.
[6]University of California at Berkeley, Berkeley CA, USA.
[7]Universitélibre de Bruxelles, Belgium.
[8]Department of Geosciences, University of Nevada Las Vegas, Las Vegas, NV, USA.
[9]Dept. of Earth, Atmospheric, and Planetary Sciences, Massachusetts Institute of Technology, Cambridge, MA, USA.
[10]Centro de Astrobiologia (CAB), CSIC-INTA, Carretera de Ajalvir km 4, 28850 Torrejón de Ardoz, Madrid, Spain.
[11]University of Oslo, Norwegian Research Council, Oslo, Norway.
[12]Jet Propulsion Laboratory – California Institute of Technology, Pasadena, CA, USA.
[13]Arizona State University, Tempe, AZ, USA.
[14]West Virginia University, Morgantown, WV, USA.
[15]Texas State University – Jacobs JETS – NASA Johnsons Space Center, Houston, TX, USA.
[16] Institut de Minéralogie, Physique des Matériaux et Cosmochimie, CNRS UMR 7590, Sorbonne Université, Muséum National d'Histoire Naturelle, Paris, France.
[17]Plancius Research, Severna Park, MD, USA.
[18]Space Science Institute, Boulder, CO, USA.
[19]CELIA - Université de Bordeaux, CNRS, CEA, France.
[20]New Mexico Museum of Natural History & Science, Albuquerque, NM, USA.
[21]University of Cincinnati, Department of Geology, Cincinnati, OH, USA.
[22]Dept. Astronomy, Cornell University, Ithaca, NY, USA.
[23]California Institute of Technology, Pasadena, CA, USA.
[24]Queensland University of Technology, Brisbane, Australia.
[25]INAF-Astrophysical Observatory of Arcetri, Largo E. Fermi 5, 50125 Florence, Italy.
[26]Institut de Recherche en Astrophysique et Planétologie (IRAP), Université de Toulouse, CNRS, UPS, CNES, Toulouse, France.

[27]Danmarks Tekniske Universitet, National Space Institute, Lyngby, Denmark.
[28]Department of Earth and Atmospheric Sciences, University of Alberta, Edmonton, Canada.
[29]Department of Earth, Atmospheric, and Planetary Sciences, Purdue University, West Lafayette, IN, USA.
[30]Johns Hopkins University Applied Physics Laboratory, Laurel, MD, USA.
[31]Cornell University, Ithaca, NY, USA.
[32]Department of Analytical Chemistry, University of the Basque Country (UPV/EHU), 48940 Leioa, Spain.
[33]LESIA, Observatoire de Paris, Université PSL, CNRS, Sorbonne Université, Université de Paris, Meudon, France.
[34]Astromaterials Research and Exploration Science, NASA Johnson Space Center, Houston, TX, USA.
[35]Department of Geosciences, Stony Brook University, Stony Brook, USA.
[36]Aeolis Research, Chandler, AZ, USA.
[37]Malin Space Science Systems, San Diego, CA, USA.
[38]INAF-Astrophysical Observatory of Arcetri, Firenze, Italia, USA.
[39]Laboratoire de Géologie de Lyon, Université Lyon, Bâtiment Géode, Villeurbanne, France.
[40]Western Washington University, Bellingham, WA, USA.
[41]Department of Earth Sciences, Brock University, St. Catharines, ON, Canada.
[42]Department of Earth Science and Engineering, Imperial College London, London, UK.
[43]RISE Research Institutes of Sweden, Stockholm, Sweden.
[44]Earth and Planetary Laboratory, Carnegie Institution for Science, Washington D.C., USA.
[45]McDonnell Center for the Space Sciences, Department of Earth and Planetary Sciences, Washington University in St. Louis, St. Louis, MO, USA.
[46]Department of Geological Sciences, University of Florida, Gainesville, FL, USA.
[47]Blue Marble Space Institute of Science, Seattle, WA, USA.

* Corresponding author: Justin I. Simon (justin.i.simon@nasa.gov)
†formerly

Key Points:

- Nine samples, consisting of four pairs of rock cores and a tube of atmospheric gas, were collected from the floor of Jezero Crater, Mars.
- *In situ* observations of crater floor outcrops, used as proxies for the samples, reveal aqueously altered igneous lithologies.
- Perseverance will leave one sample from each pair at the Three Forks depot and retain a second to be cached with future samples.

Abstract

The first samples collected by the Mars 2020 mission represent units exposed on the Jezero Crater floor, from the potentially oldest Séítah formation outcrops to the potentially youngest rocks of the heavily cratered Máaz formation. Surface investigations reveal landscape-to-microscopic textural, mineralogical, and geochemical evidence for igneous lithologies, some possibly emplaced as lava flows. The samples contain major rock-forming minerals such as pyroxene, olivine, and feldspar, accessory minerals including oxides and phosphates, and evidence for various degrees of aqueous activity in the form of water-soluble salt, carbonate, sulfate, iron oxide, and iron silicate minerals. Following sample return, the compositions and ages of these variably altered igneous rocks are expected to reveal the geophysical and geochemical nature of the planet's interior at the time of emplacement, characterize martian magmatism, and place timing constraints on geologic processes, both in Jezero Crater and more widely on Mars. Petrographic observations and geochemical analyses, coupled with geochronology of secondary minerals, can also reveal the timing of aqueous activity as well as constrain the chemical and physical conditions of the environments in which these minerals precipitated, and the nature and composition of organic compounds preserved in association with these phases. Returned samples from these units will help constrain the crater chronology of Mars and the global evolution of the planet's interior, for understanding the processes that formed Jezero Crater floor units, and for constraining the style and duration of aqueous activity in Jezero Crater, past habitability, and cycling of organic elements in Jezero Crater.

Plain language summary

Here we provide a narrative of sample collection and associated *in situ* rover observations for the rocks collected by the Perseverance rover to provide a preliminary description of the first samples of the Mars 2020 mission. These rocks collected in Jezero Crater represent the first samples from Mars with a known geologic context, the first collected with the potential to be returned to Earth for laboratory analysis, and the first cores from rock outcrops on another planet. Remote and proximal analyses indicate that all crater floor outcrops investigated are igneous in origin. Laboratory analyses of these rocks will be useful to study the planet's interior at the time of emplacement, characterize martian magmatism, and place timing constraints on

geologic processes, both in Jezero Crater and more widely on Mars. All collected rocks have interacted with water and contain secondary geochemical and mineralogical evidence that can be used to understand aqueous environments in the crater and the potential conditions of habitability for ancient life on Mars.

1. Mars Sample Return from Jezero Crater

Mars 2020 has successfully collected eight rock cores from several locations on the crater floor and an atmospheric sample (Figure 1), all described herein. These samples collected during the Crater Floor Campaign, the first Science Campaign of the Perseverance rover (see Sun et al. 2022), will be returned to Earth as part of the Mars Samples Return Program and studied to address high-priority science questions posed by the Mars science community (*cf.* Beaty et al., 2019).

1.1 Mars Sample Return

The Mars 2020 mission is the first step in a multi-stage international effort towards Mars sample return, which has been a high priority of the international planetary science community for decades (*e.g.,* Meyer et al. 2022; Kminek et al., 2022). While several different approaches to Mars Sample Return (MSR) have been considered in the past, the National Research Council (2011) Vision and Voyages for Planetary Science in the Decade 2013-2022 recommended the collection of well-documented samples from a selected site on Mars by a rover capable of mineralogic and geochemical characterization. These MSR decadal survey plans enable the planetary science community to better develop methods and approaches for sample analyses on Earth.

The principal objective of the Mars 2020 mission is to create high science value sample caches for potential return to Earth (Farley et al., 2020). A scientifically return-worthy sample cache will include distinct sample suites or individual samples selected to represent the diversity of the area explored by the Perseverance rover. This cache will address the science objectives of MSR described by iMOST (2018), in general, and, more specifically, the astrobiological potential, geologic history, and evolution of Mars as reflected in the Jezero Crater region. The scientific aim for MSR is to maximize the science return and to go beyond the minimal scientifically return-worthy sample collection. This could include returning a sample collection that contains complementary samples, *e.g.,* one that constrains the emplacement timing of a second sample with high astrobiological potential, a suite of samples that record changing conditions through time, or rocks from outside Jezero Crater that improve our understanding of those collected in Jezero (see description of scientifically return-worthy sample cache in MEPAG at https://mepag.jpl.nasa.gov/announcements/SRW_Intro_Eval.pdf). Future elements of the MSR Campaign include the MSR Program, which is tasked with the goal of bringing a scientifically return-worthy set of martian samples to Earth, and the Sample Receiving Project, which would coordinate preliminary sample analyses (*e.g.,* Haltigin et al., 2022; Tait et al., 2022), including those required for sample safety assessment (Kminek et al., 2022) within a Sample Receiving Facility.

1.2 Science rationale

The selection of Jezero Crater as the landing site was guided by several factors. First, the biosignature preservation potential of shallow subaqueous sedimentary environments (including lakes) is known to be high (Wacey et al., 2009; Westall et al., 2015; Hays et al. 2017), and Jezero is a depositional basin with one or more stages of fluvial activity during the Noachian and the Hesperian (Schon et al., 2012; Goudge et al., 2012). Second, the delta stratigraphy in Jezero contains diverse geologic units with a clear stratigraphic context (Ehlmann et al., 2008; Goudge et al., 2015; ground-truth evidence reported by Mangold et al. 2021), therefore providing a record of environmental conditions during formation/deposition. Third, the inlet river channels from the outside Jezero watershed were active during the valley network-forming era on early Mars (Goudge et al., 2015), and therefore the delta stratigraphy provides a record of environmental conditions during the time when river valley networks existed on Mars. Fourth, the Fe/Mg-smectite-rich delta stratigraphy at Jezero may have exceptionally high biosignature preservation potential and may provide an ideal location to explore for concentrated and preserved martian organic carbonaceous materials (*e.g.,* Summons et al., 2011; McMahon et al., 2018). Fifth, although carbonates are generally scarce on Mars, orbital reflectance spectra of the Jezero area show strong absorptions from carbonate minerals (Ehlmann et al. 2008, Brown et a. 2010; Goudge et al., 2015; Horgan et al., 2020; Zastro and Glotch 2021); carbonates are known to be powerful archives of paleodepositional geochemistry and may also preserve biosignatures with high fidelity (Bosak et al., 2021). Finally, the sedimentary geology is superimposed upon bedrock exposures of the Jezero Crater floor that have been hypothesized to be igneous in origin and therefore, collectively, reflect a diversity of rock types and geological processes (Goudge et al., 2015; Horgan et al., 2020; Schon et al., 2012; Shahrzad et al., 2019). This general geology has been broadly confirmed by observations made thus far during the Mars 2020 mission (Mangold et al. 2021; Farley et al., 2022; Wiens et al., 2022; Liu et al., 2022; Bell et al., 2022).

This ensemble of criteria strongly suggest that variably altered igneous samples the Mars 2020 mission has collected from the floor of Jezero Crater are valuable members of a scientifically return-worthy cache. These Crater Floor Campaign samples are well suited for returned sample science studies that will satisfy several important MSR objectives: (1) to better understand the differentiation and magmatic history of early Mars, (2) to determine the geochronology of the Jezero Crater floor and therefore the lake and delta timing, and (3) to address questions surrounding astrobiology, paleoenvironment and paleoclimate, based on the presence of minerals produced by the interactions of igneous minerals with water (including some carbonates, sulfates, and smectites) and the presence of organic materials.

The initial working hypothesis regarding geochronology proposed that the currently-exposed crater floor had an igneous origin, and a similar composition to other martian basalts, but was emplaced ~2.5 to 4.0 Ga ago, a time currently unrepresented in meteorite collections (*e.g.,* Udry et al., 2020). Support for this hypothesis comes from spectral signatures consistent with other exposures of Hesperian ridged plains (mixtures of olivine and pyroxene; Goudge et al., 2012), the range of crater retention ages spanning ~2.5 to 3.5 Ga (Goudge et al., 2012; Sharzhad et al., 2019), and a younger inferred age of the crater floor compared to the implied cessation age of valley network activity at ~3.8 Ga (Fassett and Head, 2008). The spectral signatures of igneous rocks are common for Mars and not diagnostic of age. Returned sample analysis is thus required to obtain critical evidence related to the petrogenesis, composition, age, cooling rates, alteration, and ultimately the origin, of these units.

1.3 Exploration of crater floor geology

Remote sensing and *in situ* science conducted by the Mars 2020 Perseverance rover show that the rocks exposed at the floor of Jezero Crater are in fact igneous, but have distinct formation histories (Farley et al., 2022; Liu et al. 2022; Wiens et al., 2022; Scheller and Razzel Hollis et al.; 2022, Bell et al., 2022; Tice et al. 2022). Hypotheses related to the origin of Mars and the evolution of its interior and surface motivated by both meteorite and Mars mission work will be further tested by Earth-based analyses of rock samples collected by Perseverance following MSR (Meyer et al. 2022, Kminek et al., 2022). As presented below and detailed in supporting studies contained in this special volume, the analyses conducted by Perseverance, particularly on abrasion sites, show that the bedrock units in Jezero are igneous in origin. Rocks of the Séítah formation represent an olivine-rich cumulate formed from the differentiation of an intrusive body or thick lava flow or impact melt (Farley et al., 2022; Liu et al., 2022; Wiens et al., 2022). By contrast, the much more ferroan rocks of the Máaz formation, rich in pyroxene and plagioclase, may represent either the differentiated upper portion of the Séítah magma body or a separate, younger series of lavas emplaced on top of the Séítah formation (Farley et al. 2022; Wiens et al., 2022). These bedrock units were variably altered by aqueous processes (Farley et al. 2022, Tice et al, 2022; Scheller and Razzell Hollis et al., 2022) and were likely covered by sediment at an ancient shoreline (Mangold et al., 2021; Sholes et al., 2022) and possibly a crater lake. The igneous bedrock may have erupted from a vent within the crater but could also include contributions from volcanism originating outside of Jezero. These materials could have been transported into the crater either as primary eruptions or as volcanoclastic materials, although the latter is not supported by Perseverance observations described herein and in this volume. Regardless, laboratory analysis of these samples will provide critical geochemical and geochronological evidence for reconstructing the history of Mars, and will help constrain the regional geology, potentially including the timing of younger depositional episodes and aqueous events in the crater and potential crater lake.

2. The collection of Jezero Crater floor samples

2.1 Overview of Mars 2020 operations in Jezero Crater

The Perseverance rover landed in Jezero Crater on February 18, 2021 and completed ~90 days of commissioning activities (Fig. 1). The Mars 2020 team conducted its first science campaign, the Crater Floor Campaign, to explore the units currently exposed on the Jezero Crater floor. This campaign explored the region to the south and east of the landing site for approximately 10 months, ending on sol 380, as described in detail by Sun et al. (2022, this volume). During the Crater Floor Campaign, four pairs of rock cores were collected, two each from four distinct outcrops; and one atmospheric sample was collected (Fig. 2). Pairs of samples were collected so that one sample from each pair can be deposited in a "contingency" cache on the crater floor while the rover continues to collect samples beyond the delta front and outside

Jezero Crater. Each sample target, sample core, and associated outcrop abrasion site was named (see sample stratigraphy in Fig. 2, sampling protocol outlined in Table 1, and complete list of rock unit, target, core, and abrasion site names in Table 2).

Starting from the Octavia E. Butler (OEB) landing site, Perseverance drove south towards its first sampling location in the lower Máaz formation. On sol 120 the bit carousel witness tube assembly that recorded contamination during final assembly, testing, launch, cruise, and landing was sealed. Between sols 159 and 168, Perseverance successfully conducted the Guillaumes abrasion and attempted to drill the Roubion target, although no rock was acquired in the sample tube due to the weak nature of the rock and its presumed disaggregation during drilling. Nonetheless, this sample tube was retained as an atmospheric sample, which is considered a high-priority science target for MSR (*e.g.,* Swindle et al., 2022). Subsequently, Perseverance continued west along the contact between the Máaz and Séítah formations, partly defined by the Artuby Ridge, *en route* to a location where outcrops of the Séítah formation could be accessed and investigated. Between sols 181 and 199, Perseverance attempted sampling again, this time in the Rochette member at the Citadelle locality, representing a resistant caprock layer within the Máaz formation. This resulted in successful abrasion of the Bellegarde target and acquisition of the mission's first two rock cores—Montdenier and Montagnac. Perseverance then drove further westward and northeast into the Séítah formation, where the target Garde was abraded on sol 206, shortly before a pause in operations due to solar conjunction. Perseverance thereafter drove further into Séítah and between sols 250 and 277 abraded the Dourbes target, acquiring two more rock cores—Salette and Coulettes—from the Bastide member of the Séítah formation. Between sol 286 and 290, Perseverance performed the Quartier abrasion on the Issole outcrop (Issole member, Séítah formation) and acquired a second Séítah sample pair—Robine and Malay—near the Séítah-Máaz contact as it headed south and exited the South Séítah region. In order to efficiently complete the Crater Floor Campaign and to take the quickest route to the location at which the Delta Campaign would begin, Perseverance then retraced its path toward the OEB landing site. *En route*, Perseverance collected a final crater floor sample pair from the crater-retaining Ch'ał member within Máaz. This last pair of rock cores—Hahonih and Atsah—along with a corresponding abrasion site named Alfalfa, were collected between sols 371 and 377 just east of the OEB.

2.2 Notional Mars 2020 standardized observation protocol for sample collection

During mission operations, a standardized set of minimum required activities and observations are undertaken to fully document a sample, once the sampling target has been identified (Table 1). These activities are termed the Standardized Observation Protocol, or STOP list. The STOP list includes imagery at multiple scales along with chemical and mineralogical analyses of the outcrop surface. Outcrop characterization is performed utilizing several payload instruments on the rover and is primarily focused on imaging (workspace context, targeted, and multispectral), compositional (X-ray fluorescence, laser induced breakdown spectroscopy, and luminescence), and mineralogical (Raman and VISIR) observations. The full names and a detailed discussion of the instrumentation used to explore and sample the rock targets, *e.g.,* Mastcam-Z, PIXL, SCS, SuperCam, RIMFAX and WATSON/SHERLOC, can be found in the following overviews: PIXL, Allwood et al. (2020); Mastcam-Z, Bell et al. (2021) and Maki et al. (2020); SHERLOC, Bhartia et al. (2021); RIMFAX, Hamran et al. (2020); SuperCam, Maurice et al. (2021) and Wiens et al. (2021); and SCS, Moeller et al. (2021). Because rock surfaces are frequently coated with dust or other materials, an approximately 1 cm deep and 5 cm diameter wide abrasion is created within a few tens of centimeters of each sample target in the same lithology. In this "sample proxy" site, high-resolution images and detailed maps of elemental composition, mineralogy, and potential organic matter are obtained. After coring, an image is taken of the sample in the tube (Fig. 2), the amount of sample is estimated, and the tube is hermetically sealed (Moeller et al. 2021). Unique serial numbers are readily visible on the tube and seal exteriors to ensure confident identification even decades after acquisition.

Each sample is documented in two main products: The Sample Dossier and the Initial Report. The Sample Dossier contains all observations from the STOP list, along with relevant rover data (*e.g.,* temperatures, rover location, rover arm position and actions, etc.). Uploaded to the NASA Planetary Data System (PDS) with a regular cadence, the Sample Dossier primarily consists of instrument-specific and engineering data products. These data are independently delivered to the PDS, and thus the dossier acts as a "one stop shop" for sample-specific results. The Initial Report is a description of each sample in a standardized narrative format, written by the Science Team. This initial report is written within weeks of sample acquisition to capture the reasoning for sampling and to describe the interpretations available at the time of sampling and at the completion of the STOP list. The Initial Report should be thought of as a set of field notes associated with each sample. Initial Reports are archived in the NASA PDS as an element of each Sample Dossier, providing critical inputs to the sample catalogs that will ultimately be produced for each of the samples when they return to Earth.

3. Geological context of Jezero Crater floor samples

During the Crater Floor Campaign, the eight core samples were collected from rocks that are interpreted to be stratigraphically below (*i.e.,* older than) the delta sediments, from regions initially identified as within either the Crater floor fractured (Cf-f1/2) or Crater floor fractured rough (Cf-fr) units of Stack et al. (2020). Proximal and remote analyses suggest that all crater floor outcrops investigated are igneous in origin and dominantly ultramafic to mafic in composition. The stratigraphically lower Séítah formation (*i.e.,* Cf-f1/2) is an olivine and pyroxene-bearing unit containing minor amounts (<10%) of secondary Mg-Fe carbonates. It is interpreted as a coarsely crystalline olivine cumulate. The overlying pyroxene- and plagioclase-dominated Máaz formation (*i.e.,* Cf-fr) is interpreted to be a sequence of basaltic to basaltic andesite lava flows (Farley et al., 2022; Liu et al., 2022; Wiens et al. 2022). The following section describes the geologic context of the samples collected, a narrative of the "fieldwork" that includes some first-time mission activities, and examples in which rover operations deviated from the STOP list during sample collection. Some of these details may be important for interpretation of sample analyses in the future.

3.1 Séítah outcrop targets

The Séítah formation comprises an irregular region of the crater floor consisting of NE–SW-trending ridges surrounded by megaripples, loose rocks, and boulders (Fig. 1). "Séítah" is the Navajo language term for "amidst the sands". The topography of the Séítah region was largely considered unacceptable for rover traversability, therefore rover observations were limited to a narrow corridor, approximately 200 m in length, in southern Séítah. Three outcrops (Bastide, Brac and Issole) were investigated; of these, Brac and Issole were chosen as localities for sampling. Most outcrops in the Bastide member of the Séítah formation exhibit tabular layers with relatively consistent thickness on the centimeter–decimeter scale. No layers were noted in the overlying Content member, outcrops of which overlie a possible angular unconformity, but are comparably rubbly and exhibit pits that might represent vesicles. No proximity analyses were conducted on Content member materials. SuperCam remote micro-imager (RMI) images of Séítah outcrops show a rock texture comprised of relatively equant 1.0–3.5 mm dark grey-green particles separated by interstitial lighter-toned materials. This texture is particularly evident at Bastide (see Wiens et al. 2022; Beyssac et al., this volume).

Following the Garde abrasion of Bastide, its outcrop geometry and relief were considered unsuitable to conduct the full suite of proximity science required prior to sampling (*i.e.,* the STOP list), and thus the decision was made to seek another, similar, outcrop for the next sampling attempt. A suitable candidate (Brac, within the Bastide member) was identified near the contact with the overlying Content member (Fig. 3, anaglyph Supplement I, outcrop map Supplement II). Based on its morphology, concordance with surrounding outcrops, and estimated dip consistent with that of the wider Séítah region, the Brac outcrop was confidently interpreted to be a portion of the Séítah bedrock. Perseverance conducted outcrop analysis, abrasion (the Dourbes abrasion site), and sampling at Brac, leading to the acquisition of the two rock cores – Salette and Coulettes. The Salette core is a full-length sample (~6 cm), whereas the Coulettes core is considerably shorter (~3.5 cm). A disc-shaped fragment detached from the base of the Salette core after sampling, perhaps due to fracturing along a layer boundary or other plane of weakness.

The second Séítah sampling locality, the Issole outcrop, is located near the boundary between the underlying Séítah and overlying Máaz formations; because the boundary is covered by regolith, the nature of the contact remains unknown (Fig. 4, anaglyph Supplement I, outcrop map Supplement II). Perseverance conducted outcrop analysis, abrasion (the Quartier abrasion site) and sampling at Issole, leading to the acquisition of the two cores–Robine and Malay. Following the sampling of Robine, the acquisition of the planned second core Pauls was prevented by a fault during the transfer of the sample tube into the Adaptive Caching Assembly, precluding its processing. Subsequently, it was found that a few fragments of the Pauls core had become lodged in the bit holder, likely having fallen out of the sample tube. These fragments prevented the coring bit from being fully seated into the bit holder and the team decided to expel the Pauls core and re-sample the adjacent Malay region using the same sample tube. The Robine core is a full-length sample (~6.5 cm), whereas the Malay core is considerably shorter (~3 cm). CacheCam images of both cores suggest that they are intact and unfractured (see Fig. 1).

The interpreted subsurface stratigraphy from estimated permittivity values of the RIMFAX radargram of Séítah targets on the 201 and 237-238 sol paths are shown in Figures 3 and 4. Estimated densities around 3.5 g/cm^3 are in accordance with the olivine-rich Séítah lithology observed at all three outcrops studied (Hamran et al., 2022). The subsurface appears to represent a sequence of SW-dipping to subhorizontal rocks from approximately 3 m below the surface level to > 8 m burial depth interpreted as an extension of the Issole member that also appears to extend below Artuby Ridge further south. This lower unit appears to be truncated by an angular unconformity. The potential unconformity is overlain by a 2-3 m thick sequence that is more clearly bedded and that outcrops at the surface as the Bastide member (containing the Bastide and Brac outcrops).

3.2 Máaz *outcrop targets*

The Máaz formation, named for Navajo language term for "Mars", is a widespread unit in the crater that, from High Resolution Imaging Science Experiment (HiRISE) camera orbital views, appears fractured in a distinctive meter-scale polygonal pattern. Broadly, the Máaz formation exhibits a smooth lower morphology and a rougher, more massive, rubbly, and cratered upper morphology. The Máaz formation stratigraphy varies from layered, to homogenous and massive in nature and has been subdivided into five members: Roubion, Artuby, Rochette, Nataani, and Ch'ał (see Sun et al., 2022). Several possibilities exist for the Máaz stratigraphy, including one that is largely based on elevation (the sequence as listed above, from bottom to top) and one in which Roubion is stratigraphically between Rochette/Artuby ("lower Máaz") and Nataani/Ch'ał ("upper Máaz"). This grouping is supported by spectral and compositional similarities within the upper and lower groups, where lower Máaz members are more mafic and pyroxene-dominated, and upper Máaz members are more silicic and plagioclase-dominated, with Roubion exhibiting intermediate properties (see Horgan et al. 2022). In this model, Roubion and some portions of upper Máaz are found at elevations below Rochette and Artuby due to infill by "upper Máaz" of paleotopography carved into the "lower Máaz". This supports the hypothesis that, at least locally, upper Máaz may fill an eroded surface, *i.e.,* a "paleovalley", in lower Máaz near the Séítah "Thumb" area (Fig. 1). Another common feature of the Máaz formation is that it is observed at elevations that are below the highest portions of the putatively older Séítah rocks.

The Roubion coring attempt, the Guillaumes abrasion site, and the associated STOP list activities, were undertaken on a very low relief rock (Fig. 5, anaglyph Supplement I, outcrop map Supplement II) selected largely to meet first-time engineering requirements for sampling. Coring at Roubion produced a hole and tailings pile, and the entire coring and sealing process completed nominally. However, the Perseverance volume probe indicated no sample, this was confirmed by CacheCam images documenting an empty sample tube (Figure 2), *i.e.,* no core was recovered. In the absence of a core or core fragments on the ground, the most likely explanation is that the rock disaggregated during coring and either contributed to the tailings pile or fell back to the bottom of the borehole. Further coring at this location was abandoned. Although no rock core was obtained, the tube has several dozen ~10 μm sized particles and the sealed Roubion sample inadvertently provides a returnable sample of approximately 4.9 μmol of martian atmosphere.

The interpreted subsurface stratigraphy from estimated permittivity values of the RIMFAX radargram for the 157-168 sol path are shown in Figure 5. The ~2.5 to 2.8 g/cm^3 densities estimated are similar to that of basaltic material (Hamran et al., 2022). The radargram shows surface parallel reflectors and fine-scale layering below the smooth morphology down to a burial depth of approximately one meter. Arcuate structures observed in radargrams may represent small, buried impact craters. Deeper reflectors (>3 m into the subsurface) appear to dip southward and may be associated with Séítah sequences.

After an unsuccessful first attempt to collect a rock sample from low-lying Máaz outcrops at Roubion, Perseverance traversed approximately 450 m NW along the base of Artuby Ridge, a ~1 km long NW-SE trending linear ridge exposing on its NE side a several meter high cliff of the crater floor stratigraphy (Fig. 1). In HiRISE images, the trough at the base of Artuby defines the morphological boundary between the southern edge of Séítah and exposures of Máaz. The team decided to target the relatively high-standing Máaz formation rocks along the top of Artuby, which define the Rochette member for sampling.

The rocks forming Artuby Ridge are variably layered to massive. Thick (10s of cm), laterally discontinuous layered rocks occur along the NE-facing slope of Artuby Ridge; thin (cm-scale), planar layered rocks are observed near the crest of Artuby Ridge. These layered rocks appear to transition into more massive exposures both laterally and up-section within Artuby Ridge (see Alwmark et al., this volume). The appearance of thin, laterally continuous layering within the rocks of Artuby Ridge indicates a notable transition from the apparently massive rocks observed from OEB to Roubion, *i.e.,* in the upper Ch'ał member.

The interpreted subsurface stratigraphy from estimated permittivity values of RIMFAX radargrams acquired during the rover's drive along Artuby Ridge (sol 177), ascent of Artuby Ridge and arrival at Citadelle (sol 178), and after the short bump to Rochette (sol 180), are shown in Figure 6 (see anaglyph Supplement I, outcrop map Supplement II). While driving along the base of Artuby Ridge, RIMFAX observed a sequence of SW-dipping reflectors that dominate the subsurface stratigraphy from approximately surface levels to >10 m burial depth. Starting on sol 178, the radargram shows a relatively thin horizontal capping layer, consistent with the Rochette outcrop at the surface. It remains unclear whether the deeper layers, south of Rochette, are horizontal like the surface layer or SW-dipping. The estimated permittivity suggests that the horizontal, near surface layers are similar to basaltic material whereas those at depth exhibit greater density consistent with an olivine-rich lithology (Hamran et al., 2022), suggesting that rocks similar to Séítah (*e.g.,* Issole member?) are present at depth (see Fig. 6 caption for details).

The first fully successful sampling event occurred at Citadelle where Montdenier and Montagnac, the pair of rock cores representing the second sample target of the Mars 2020 mission, were collected (Fig. 6, anaglyph Supplement I, outcrop map Supplement II). The cores, and their companion Bellegarde abrasion site, were acquired on a small tabular boulder (Rochette, ~40 cm across) forming part of a NW—SE-trending band of similar boulders and outcrops on the SW side of the Artuby Ridge crest. These blocks appear morphologically consistent with a degraded lava flow (Fig. 6). Rochette (the block from which the samples were acquired) moved slightly during coring, confirming that it is not currently anchored to in-place outcrop. Although Rochette may have been displaced from its original location, the lateral extent and similarity of the blocks near Rochette suggest that this displacement is likely small, and an estimated emplacement position may still provide a useful constraint for some studies. Rochette was selected in part because it is stratigraphically higher than Séítah on Artuby Ridge, and therefore likely younger. As discussed above, the capping layer of Artuby Ridge that contains Rochette is located at a higher elevation than Roubion where the Guillaumes abrasion was made, but it remains unclear whether the Rochette member is actually younger or whether the Roubion member, along with upper Máaz formation material, filled paleotopography of eroded Rochette and Artuby member stratigraphy of the lower Máaz formation near Mure and the Thumb of Séítah.

Given the unexpected outcome of the Roubion sampling attempt, coring of Montdenier included an unusual step to confirm the presence of a sample in the tube with Mastcam-Z images prior to tube sealing. In the intervening 4-sol period, the sample was exposed to the martian environment. This exposure is a notable deviation from the notional sampling sol path in which the tube is sealed autonomously within hours of coring. The paired core Montagnac was collected and sealed on sol 196 following the normal automated procedure and without visual confirmation prior to acquisition. Coring of Montagnac produced a hole and tailings pile of expected appearance, and the entire coring and sealing process completed nominally. The volume probe indicated full length, *i.e.,* ~6.0 cm or ~8.5 cm^3, cores in each sample tube.

The final pair of rock cores from the crater floor was collected from the morphologically rough upper Ch'ał member of the Máaz formation. The Ch'ał member comprises massive rocks that form hummocks and ridges outcropping east of the OEB and the southward traverse to Séítah. The Ch'ał member was recognized early in the mission as a morphologically distinct unit from the low-lying, polygonally jointed rocks (Nataani member) on which the rover landed and traversed. Named for a large rock observed on Sol 78, the Ch'ał member generally presents as angular, massive, cobble to boulder-sized, dark-hued rocks with scattered pits, which might represent vesicles, but otherwise little apparent internal structure. Ch'ał-type rocks are observed to overlie Nataani member rocks and, in many places, dark-hued, ventifacted "nubs" project upward from Nataani member outcrops (Fig. 7). These nubs may be residual products of in-place weathering of Ch'ał rocks. The Ch'ał rocks were known from the early part of the mission to have the most evolved compositions of those observed on the crater floor (Wiens et al. 2022).

Several locations and rock types were considered for Ch'ał sampling as the rover traversed north in the last leg of the Crater Floor Campaign. Throughout the campaign, exposures of the Ch'ał unit were observed in east-facing viewsheds, for example, east of the Roubion sample location. The expression of these topographic highs and their visible/near-infrared spectral properties in Mastcam-Z multispectral images can be clearly tied to at least one well-defined cratered region on the surface of the Máaz formation to the south and east in HiRISE and CRISM images (Fig. 1). The team evaluated candidates for sampling based on their morphologic and topographic similarities to the Ch'ał archetype and evidence that the rock was in place. As the rover passed southeast of OEB, the team identified several blocks of Ch'ał-type material in direct contact with underlying Nataani rocks, including a boulder named Sid (Fig. 7, anaglyph Supplement I, outcrop map Supplement II). The relatively large size of Sid and other rocks in the area, and their direct contact with the underlying flat rocks of the Nataani member, imply that Sid may be derived directly from the receding Ch'ał member and may not have been moved or rotated significantly after deposition. This satisfied the above criteria for collecting a sample.

Outcrops of Ch'ał member blocky material at topographic highs overlying the recessive polygonal rocks, such as Nataani and Roubion, appear to form a coherent layer in subsurface sounding in RIMFAX radargrams (Fig. 7). In the subsurface, the uppermost ~2 m represents the Máaz formation, where the deposits are dominated by horizontal layering and polygons visible at the surface. Intra-polygon fractures are not visible in the radargram, suggesting that these fractures may be very shallow. Bowl-shaped reflector geometries in the Máaz formation are interpreted to represent remnant impact structures. Based on density estimates and interpretations of subsurface radargram geometry, underlying Séítah formation strata potentially lie between ~2 and 7 m burial depth (*e.g.,* Hamran et al. 2022). To avoid traversability hazards, the rover avoided high standing Ch'ał member outcrops; as such, the sample target was not directly characterized by RIMFAX radar observations.

4. *In situ* analyses of sampled outcrops

In the following section, we present the main observations made on the abrasion sites and associated natural surfaces of the sampled outcrops, which are intended to serve as proxies for the rock samples collected. We present key data highlighting the textures, compositions, and mineralogies of the crater floor bedrock to enable comparisons among the collected rock samples and those to be collected later in the mission. Table 3 lists the key attributes of the crater floor samples available for return to Earth.

4.1 Primary rock type of sampled Séítah outcrops

Identification of large (~1-3.5 mm) olivine crystals exposed on relatively fresh natural surfaces of Séítah rocks were confirmed in the Dourbes and Quartier abraded sites at Brac and Issole, respectively (Figs. 8 and 9). This cumulate texture includes euhedral to subhedral olivine crystals surrounded by intercumulus pyroxene. Co-registered WATSON images and PIXL X-ray fluorescence maps on abraded surfaces reveal a concentrated network of olivine crystals that accounts for up to 60% of the rock (Fig. 9). These observations are expanded on by coordinated SHERLOC (plus the Autofocus and Context imager, ACI), SuperCam-LIBS/VISIR spectroscopy, and Mastcam-Z multispectral observations. In Dourbes (and Garde), the crystals are equant, whereas in Quartier some olivine crystals appear more elongated (Liu et al., 2022; Wiens et al. 2022).

PIXL X-ray element maps indicate Fo_{55} olivine compositions and intercumulus material that is dominated by monocrystalline and crystallographically oriented augitic pyroxenes that grew around and among the olivine grains (Liu et al., 2022; Tice et al. 2022), which is within the range of Fo_{44-66} calculated using CRISM orbital data (Brown et al., 2020). At grain boundaries and within interstitial spaces defined by the olivine and pyroxene crystals, Na-rich and K-rich feldspar, as well as accessory Fe-Cr-Ti oxides and Ca-phosphates were observed. More detailed and refined mineral compositions are presented in Liu et al. (2022) and Wiens et al. (2022). The mesostasis likely represents crystallization of late-stage melt enriched in incompatible elements (Liu et al. 2022), but some of the phases may be secondary.

Bulk sum analysis of the PIXL mapping data obtained in selected scans of the Dourbes (Garde) and Quartier abrasion sites (Fig. 10; PIXL scans in Fig. 9) are shown in Table 4. These analyses include a mixture of likely primary igneous mineralogy together with secondary phases arising from later alteration. PIXL mapping focused on the primary mineralogy of abrasion sites shows that the SiO_2 contents of 30–50 wt.% and Na_2O+K_2O contents of ~0-2 wt.% are relatively constant across the Dourbes and Quartier sites. SuperCam-LIBS analyses were undertaken on both the natural surfaces and abraded sites of Séítah. SuperCam-LIBS analyses of the natural surfaces indicate SiO_2 contents of ~45 wt.% and Na_2O+K_2O contents ~2 wt.%. Although the SiO_2 abundance is approximately the same in the abraded sites, alkalis measured using SuperCam-LIBS on the abraded Séítah sites (<1 wt.%) are generally lower than the natural surfaces. SuperCam-LIBS and Raman spectra indicate olivine Fo_{55-60} (Wiens et al. 2022; Beyssac et al., this volume). As shown by the oxide ternary diagram (PIXL data, Fig. 10) and total alkali versus silica diagram (SuperCam-LIBS data, Fig. 11), the bulk compositions of the Séítah targets are consistent with an ultramafic rock modified by some degree of aqueous alteration.

4.2 Primary rock type of sampled Máaz outcrops

Rock textures observed in the Guillaumes, Bellegarde, and Alfalfa abrasion sites of Máaz formation rocks indicate grain sizes that vary between ~0.2 and 0.5 mm for Rochette, ~0.5 and 1.0 mm for Roubion, and ~0.5 and 3.5 mm for Sid (Figs. 12 and 13). Light and dark grains or crystals comprise most of the abraded surfaces. The light materials have at least two distinct morphologies and tones: some have angular shapes, including potential elongated feldspar laths, whereas others (especially those that are brightest white) have a more irregular outline. The latter suggests a secondary cavity-filling or replacement phase. Excluding evidence of secondary alteration, the light and dark grains appear roughly equal in size with an obvious spatial heterogeneity in relative abundance. There is little evidence of a fine-grained "microlite" matrix in the Máaz rocks, but rather a more uniform grain size distribution. There is no compelling evidence of the intergranular porosity or cements common to many sedimentary rocks. Taken together, these observations are consistent with fine-grained gabbro or holocrystalline basalt. The exception is the porphyritic texture observed in Alfalfa of the upper Máaz, Ch'ał member that exhibits relatively large euhedral feldspar crystals, several millimeters in length, within a finer-grained feldspar- and pyroxene-dominated matrix. Although the matrix observed in Alfalfa is similarly coarse to that of other Máaz rocks, its grains are more elongated than those in Guillaumes and Bellegarde. Collectively, these observations suggest that Alfalfa represents a more rapidly cooled lava (see Fig. 13). In all Máaz rock targets, abrasion surfaces exhibit evidence for a homogeneous distribution of interlocking grains suggesting textures consistent with crystallization from a magma (Fig. 13).

Coordinated PIXL X-ray mapping and WATSON images, SuperCam-LIBS, SHERLOC-Raman spectroscopy, and Mastcam-Z multispectral data indicate that the minerals present in Máaz rocks include at least two pyroxene compositions, likely an Fe-rich augitic and an Fe-rich but less Ca-rich pyroxene like pigeonite, plagioclase feldspar, a third mafic silicate phase (olivine or orthopyroxene?), and Fe-Ti-oxides, together with secondary iron oxides and/or silicates, sulfates, Na-Cl and/or $Na\text{-}ClO_4$ salts, and phosphates (Figs. 9-13; see Clavé et al., 2022, this volume; Meslin et al., 2022, this volume). More detailed and refined mineral compositions are presented in Udry et al. (2022); Tice et al. (2022); and Fe-bearing minerals detected by Mastcam-Z multispectral data and CRISM hyperspectral data in Máaz are presented in Horgan et al. (2022, this volume). Accessory phases occur at grain boundaries between plagioclase and pyroxene and may be late-stage primary, secondary, or both (Kizovski et al., 2022).

X-ray fluorescence mapping by PIXL was undertaken in selected areas of the Guillaumes, Bellegarde, and Alfalfa abrasion sites (Fig. 10; PIXL scans in Figs. 9 and 13). The bulk sum analysis of each scanned abrasion surface is shown in Table 4. Note, as for the Séítah observations, that these analyses include a mixture of what are likely primary igneous mineral grains along with secondary phases suggestive of later alteration. PIXL analyses of abrasion sites show SiO_2 contents of 30–70 wt.% and Na_2O+K_2O contents of ~2-9 wt.%. These data, especially those for Guillaumes and Bellegarde, show considerable spread, likely attesting to a significant salt contribution to their bulk compositions. These are therefore unreliable for an igneous rock classification as presented. SuperCam-LIBS analyses undertaken on natural surfaces and abraded sites at each sampled Máaz formation locality also show considerable spread in composition, but the targeting nature of the LIBS approach appears to reflect a more representative analysis of the primary rocks and indicates that Ch'ał is relatively evolved (see Fig. 11; Wiens et al., 2022).

The Máaz rock compositions span from basaltic to andesitic with evidence of some addition of salt and aqueous activity recorded in the bulk chemical signatures, as shown by the oxide ternary diagram (PIXL data, Fig. 10) and total alkali versus silica diagram (SuperCam-LIBS data, Fig. 11). Although no abrasion or sample core was collected from the Content member atop Séítah rocks, its composition as determined by SuperCam-LIBS generally matches other Máaz units, is distinct from Séítah, and therefore may have implications for the hypothesized stratigraphy and formation of crater floor rock (*cf.* Wiens et al. 2022).

4.3 Alteration of crater floor rocks

Both the Séítah and Máaz formations have undergone variable degrees of post-emplacement aqueous alteration. The presence of reddish-brown staining and the identified SCAM VISIR hydration peaks are consistent with aqueous deposition of iron oxides or Fe silicate (see section 5.2; Mandon et al., 2022, this volume). Surface coatings are common on Jezero Crater floor rocks (Bell et al., 2022; Wiens et al. 2022). Mastcam-Z and SuperCam RMI images reveal several brown to reddish domains, ranging in areal extent from patches to regions with more continuous coatings. Some areas have thicker coating layers. These coatings are spectrally and thus compositionally distinct from the underlying rock (*e.g.,* see Garczynski et al., 2022, this volume). The elemental compositions of the coatings are similar to those of Mars global dust.

Although natural surfaces of Séítah appear to have elevated alkalis compared to the corresponding abraded surfaces in SuperCam-LIBS observations (see Fig. 11), the degree of alteration of samples collected from Séítah appears relatively minor because much of the geochemistry and textures of the primary rocks have been retained, *i.e.,* the dissolution of olivine crystals, if it occurred at all, is minimal (Liu et al., 2022).

Imaging and chemical investigations of the Brac outcrop indicate the presence of multiple, varied alteration phases. High-resolution WATSON imaging of the Dourbes abraded surface reveals a reddish, likely Fe-bearing, secondary phase filling interstitial spaces among primary minerals (Figs. 8 and 9). Mastcam-Z multispectral imaging of the natural surface mainly reflects the dust coverage on the outcrop while similar analyses of the Dourbes abrasion site reveals spectral signatures of a secondary phase, likely ferric oxides (Fig. 8). SuperCam-VISIR data suggest the presence of Fe- and Mg-bearing phyllosilicates (Fig. 14). Both the ferric oxide and Fe-bearing phyllosilicate phases are consistent with WATSON observations. Mineral compositions inferred from PIXL data, while dominated by primary phases, also show evidence of secondary phases, such as sulfate, calcite, and halite (Fig. 10). Spots of concentrated $CaSO_4$ and $MgSO_4$*nH_2O as well as an occurrence of perchlorate were documented by PIXL (Tice et al., 2022). Similarly, a carbonate phase in the abrasion site was also identified by SuperCam-LIBS/VISIR and SHERLOC-Raman (Figs. 14 and 15). A hydration signature consistent with Fe-(hydr)oxide and phyllosilicate phases, is also apparent in SHERLOC-Raman and SuperCam-VISIR data (see Mandon et al., 2022, this volume).

The Quartier abrasion site on Issole shows characteristics of alteration similar to those observed in Dourbes on Brac (Figs. 8, 14, and 15). Purple-hued areas in WATSON images of the natural surface, which are likely indicative of a surface coating, have a spectral signature consistent with ferric iron. The reddish-brown material in the abrasion sites (Fig. 8) attributed to Fe-oxyhydroxides via Mastcam-Z multispectral data appears to surround a pale-brown/white phase, which has been identified as a sulfate (possibly Mg/Ca/Fe-bearing) by SHERLOC (Fig. 15). Similar to Dourbes, possible Fe-phyllosilicates, Mg-phyllosilicates, and carbonate were detected by SuperCam-VISIR (Fig. 14). Raman data from SHERLOC also point to the presence of carbonate and Mg-sulfate in these rocks, particularly in the Quartier abrasion site (Fig. 15). A large (approximately 4 mm^2) area of what is thought to be nearly pure Mg/Ca-sulfate was detected in one PIXL scan, but a second scan of a more representative portion of primary mineralogy of the Quartier abrasion site resulted in much lower average SO_3 concentrations, in-family with Jezero samples analyzed to this point (Cl/S ratio [atom/atom] > 1.0).

The samples from the Máaz formation (Montdenier, Montagnac, Hahonih, Atsah), as well as the three Máaz abrasion sites (Bellegarde, Alfalfa, and Guillaumes) all share some common evidence of alteration, but also possess evidence of alteration that is specific to individual samples, best described as variability in their degree of alteration. The Roubion target extends this range as it exhibits pervasive alteration and secondary mineralogy; this factor may have led to its disaggregation during coring. Reddish staining is present in all Máaz abrasion sites (Fig. 9) and is consistent with iron oxide detected by Mastcam-Z, PIXL, and SuperCam-LIBS. This phase often occurs as an alteration rind around grains and/or voids. The degree of oxidation in Máaz abrasion sites varies significantly, as shown based on 525 nm band depth in Figure 12. Clear signatures of fine-grained hematite are detected in Alfalfa, while oxidation consistent with nanophase hematite is detected in Bellegarde, and no significant oxidation is detected in Montpezat (an abrasion within the Artuby member of Máaz formation at the base of Artuby Ridge), suggesting highly variable oxidation during emplacement or later weathering.

Spectral signatures of Fe- and/or Mg-phyllosilicates and a hydration signal are also evident in SuperCam-VISIR data from all abrasion sites (Fig. 14). Analysis presented in Wiens et al. (2022) indicates that from the observations across the Máaz formation, up to 20-25% of the MgO and a lower percentage of the CaO are due to accumulation of sulfates and other precipitates. Bellegarde and Alfalfa contain possible Al-phyllosilicates evidenced in data from PIXL and SuperCam, respectively (see Fig. 5 and Wiens et al. 2022). The Guillaumes and Bellegarde abrasion sites contain voids that are sometimes filled with white materials as seen in WATSON images (Figs. 12 and 13). The Guillaumes abrasion site appears particularly flaky and granulated compared to the other abrasions. Voids are noticeably absent from the Alfalfa abrasion site.

Ca-sulfates, perchlorates, silicates, carbonates, and phosphates are potential void-filling secondary phases detected in abrasion sites from the Máaz formation. All of these phases were identified by SHERLOC while detections of sulfates are supported by SuperCam-VISIR data (Fig. 14) and PIXL data suggest the presence of carbonates, halides, sulfates, and perchlorate (Fig. 10). The average S and other elemental abundances for Bellegarde, Rochette, and Guillaumes are approximately equivalent (Table 4) with the exception of the Guillaumes abrasion site, which indicates a much higher (>2x) concentration of Na and Cl. Sulfate and perchlorate salts occupied the largest volume in the Guillaumes abrasion site (*i.e.,* the unsuccessful rock core sample), where perchlorate, including sodium perchlorate, was also detected by SuperCam-Raman (see Meslin et al., 2022, this volume) and SHERLOC-Raman (see Murphy et al., 2022 and Corpolongo et al., this volume). The oxidized anions in these salts indicate a later origin relative to the deposition of the primary igneous minerals that contain reduced iron such as pyroxene and olivine and the spatially and volumetrically limited precipitation of iron(II)-containing carbonate in Séítah. In other abrasion sites, significant concentrations of Cl at the sub-mm scale were detected with PIXL scans, but correlations with Na were weak or absent, whereas a weak association with Fe was sometimes indicated. Most of the salt phases identified elsewhere were not detected in Alfalfa and voids are noticeably absent, further attesting to its minimal degree of alteration.

Visible and IR spectroscopy of the crater floor rocks and the compositional and Raman spectroscopic maps of all abraded sites from Séítah did not reveal any veins or even mm-scale accumulations of salts with sulfate or oxychlorine anions. PIXL and SHERLOC detected smaller sites of sulfate and oxychlorine salts in the rocks sampled from both Máaz and Séítah (Figs. 9, 13, and 15). The coexistence of oxidized and reduced phases in the same rocks suggests multiple episodes of aqueous alteration under changing redox conditions or electrochemical reactions occurred that were capable of producing both such phases from a single fluid (*e.g.,* Steele et al., 2018). Analyses in Earth-based laboratories are required to address when these episodes occurred, whether they involved fluids with different organic contents and whether and how they preserved organics.

Fluorescence spectroscopy, as obtained with SHERLOC, can be used to detect and characterize diverse aromatic compounds within samples and perform preliminary classification based on number of rings (Bhartia et al 2008). Abrasion sites in both Máaz and Séítah show similar fluorescence features (single band at 270-295 nm, single band at 335-350 nm, and doublet at ~303 and 325 nm, two peaks at ~290 and 330 nm) (Fig. 15). The 270-295 nm feature likely originates from single-ring aromatics, and in many cases is co-located with the single band at 335-350 nm. The 335-350 nm features likely originate from double-ring aromatics and/or Ce^{3+} fluorescence emissions from inorganic mineral phases like phosphates (Scheller and Razzell Hollis et al., 2022). The doublet at 303 and 325 nm most likely originates from single- or double-ring aromatics, though the possibility of mineral (Ce^{3+}) fluorescence emission contribution is still being investigated. The two peaks at ~290 and 330 nm could represent a one- or two-ringed aromatic compound. The fluorescence spectra may be attributed to aromatic organic compounds with a fairly low average abundance, comparable to detections in some martian meteorites (*e.g.,* Steele et al., 2012; 2016; 2018; 2022; Koike et al., 2020; Jaramillo et al., 2019). The most significant difference in fluorescence signals between the two formations is the close to order of magnitude more detections in Máaz versus Séítah (see Sharma et al., 2022). The 335-350 nm feature is observed in all targets while the fluorescence doublet at 305 and 325 nm is only detected in the Bellegarde and Quartier targets, in which it is associated with sulfates, and the 290 and 330 nm features are found associated with carbonates and silicates. The other two fluorescence features (270-295 nm, 335-350 nm) have less clear associations with minerals although the 335-350 nm feature seems to be preferentially associated with grain and 270-295 nm with brown-toned alteration material.

SHERLOC deep UV Raman analysis also detected peaks that may be due to organic carbon on multiple targets. Raman spectroscopy is less sensitive than fluorescence spectroscopy, so the signal-to-noise ratio and number of detections is expectedly lower. In two of the targets, Garde and Quartier, the Raman detections were correlated with the strongest fluorescence detections. In the third, Montpezat, a possible G band (*i.e.,* C-C bond) was detected.

5. Returned sample science potential

The Mars 2020 Science Team has prioritized key science questions to be addressed by the samples collected by Perseverance upon their return to Earth. As the first suite of samples returned to Earth from a known locality on Mars, these samples represent the opportunity for the global scientific community to address major outstanding questions relating to geochemistry, geochronology, petrogenesis, paleomagnetism, planetary evolution, paleoenvironments, and potentially astrobiology from the early history of Mars (*i.e.,* the Noachian-Hesperian period).

Scientific rationales for the return of each collected sample are listed in Table 3. These mission goals align with longstanding MSR science objectives held by the international planetary science community. Earth-based analysis of igneous rocks of the Jezero Crater floor sample suite, described herein, will provide important constraints on a number of these questions as discussed below.

5.1 Igneous Jezero Crater floor bedrock samples

Surface operations of the Mars 2020 mission have provided exceptional geological context for the igneous samples collected. From orbital observations, crater floor rocks are suggested to be related to widespread lithologies outside of Jezero (*e.g.,* Mandon et al., 2020; Brown et al., 2020). Determination of similar (or distinct) lithologies and/or ages in Jezero and outside of Jezero rocks would help to constrain aspects of the regional geologic history, and potentially the planetary evolution of Mars, as described below (section 5.4). Future rover operations outside Jezero Crater will further clarify these lithological relationships, but Earth-based analyses of the igneous lithologies from Jezero and samples from their plausible outside Jezero equivalents (*i.e.,* the "olivine-carbonate" and/or "mafic cap" units of Mandon et al., 2020) would lead to a more comprehensive and robust reconstruction of regional geologic history and planetary evolution.

5.1.1 A collection of igneous olivine cumulate and basaltic to andesitic samples

Typical igneous minerals and textures, ranging from cumulate with adcumulus growth in Séítah to aphanitic and porphyritic in Máaz, have been observed. The eight cores collected contain varying amounts of olivine, plagioclase, ortho- and clinopyroxene, as well as minor minerals such as oxides and phosphates. Textures and mineralogies of the samples can be used to partially constrain their petrogenesis; however, compositions, atomic structure, and bonding within individual minerals, as well as trace element and isotopic signatures widely used to constrain specific formation temperatures, pressures, source volatile contents, and ages will require levels of analytical precision and spatial resolution only afforded by returned sample laboratory analyses.

5.1.2 The first rocks from Mars with geologic context

The age and composition of rocks from Mars provide insights into the geology of its surface and interior. More than 175 distinct martian meteorite samples (Udry et al., 2020) have been collected on Earth, and while they have greatly enhanced our understanding of the geological evolution of Mars, they are an inferior archive compared to samples collected directly by the Mars 2020 mission. The majority of martian meteorites (~88%) have crystallization ages of <600 Ma; this is at odds with the fact that >75% of the martian surface rocks date to the Noachian or Hesperian Periods (≥3.2 Ga; Tanaka et al., 2014). Based on a few dominant cosmogenic exposure age populations, most martian meteorites likely represent less than approximately one dozen launch sites (*e.g.,* McSween, 2015, and references therein). A vast majority of martian meteorite bulk compositions do not match compositions of martian terrains investigated to date by either remote sensing or rover exploration (McSween, 2015). These three issues imply that martian meteorites represent neither the diversity of the martian surface nor that of the interior. This is further corroborated by considerations of the impact process by which martian meteorites are delivered to Earth, which demonstrate a bias towards younger, more competent igneous rocks (*e.g.,* Warren, 1994; Walton et al., 2008; Udry et al. 2020, and references therein). Finally, no definitive link has yet been made between any of the martian meteorites and their source craters.

Although the emplacement timing of the crater floor rocks needs to be more precisely constrained, comparisons of the mineralogy, petrology, and geochemistry of the returned samples with martian meteorite lithologies also has the potential to provide fundamental insights into the range of mantle source compositions and conditions of melting present within Mars over time, and to elucidate the variety (or lack thereof) of eruptive compositions. It will place valuable constraints on the composition of the martian interior at a rather early to intermediate stage of chemical differentiation (Pinet and Chevrel, 1990; Clenet et al., 2013). The olivine cumulate lithology represented by samples from Séítah (Salette, Coulettes, Robine, and Malay cores) appears to have similarities to the considerably younger chassignite and poikilitic shergottite subgroup of martian meteorites, at least at first look (Liu et al., 2022). The Máaz lithologies bear some similarities to basaltic shergottites, augite-rich shergottites, and alkali-rich igneous clasts found within NWA 7034 (*e.g.,* Rubin et al., 2000; Herd et al., 2017; Santos et al., 2015; Tait and Day, 2018; Udry et al., 2017; 2022), although they are significantly more ferroan than all known martian meteorites (*cf.* Udry et al. 2020).

The apparent similarity between the preliminary composition of the Séítah formation and some martian meteorite lithologies suggests that similar conditions and mantle compositions existed during magmagenesis at the time of the formation of these units despite the large difference in likely formation age. However, the observation that Máaz formation rock lithologies are more ferroan than most martian meteorites suggests that some, if not all of the igneous rocks in Jezero, have distinct magmatic histories, perhaps derived from mantle source(s) with different bulk compositions, differing conditions of partial melting, ascent and emplacement, crustal assimilation, and/or involving melts produced by impact of altered surface rocks.

In addition to bulk mineral and major element analyses, trace element analyses will be crucial for constraining the possible source reservoirs of Jezero rocks and testing their magmatic petrogenesis. For example, trace element data may distinguish between a single differentiated system or separate magma generation events (*cf.* Farley et al. 2022). Trace element geochemistry can also be employed to understand why these rocks are so ferroan; rare earth elements could be used to test whether crustal assimilation was important to magmagenesis (Peters et al. 2018), and siderophile element abundances may denote the assimilation of chondritic meteorite materials and thus be used to test an impact melt origin hypothesis (*e.g.,* Day et al., 2016; Goderis et al., 2016).

Investigating the petrogenetic history of samples from the Máaz and Séítah formations by trace element analyses (*e.g.,* REE abundances) can help us better understand the igneous evolution of Mars. *In situ* analyses on Mars cannot distinguish whether Bellegarde or Dourbes are derived from depleted or enriched shergottite-like or nakhlite/chassignite-like mantle sources, or from entirely distinct mantle source types. This can only be determined in terrestrial laboratories.

5.1.3 Potential isotopic record of Jezero Crater floor igneous rocks

In addition to trace elements, isotopic analyses will help to better constrain the number of source reservoirs in the martian interior (including the mantle and crust), their compositions, and possible mixing phenomena. Meteorite studies demonstrate the great possibility to perform high-precision analyses of martian materials in Earth-based laboratories; for example, isotopic analyses help to constrain processes relating to the geodynamical evolution of Mars (*e.g.,* Harper et al., 1995; Borg et al., 1997; Debaille et al., 2007; Borg et al., 2016; Moriwaki et al., 2020). Measuring the radiogenic ingrowth of elements such as Ca, Sr, Nd, Hf, and W provide constraints on both the differentiation of the planet into several internal reservoirs and the timing of such events (Fig. 16). Such analyses require not only ultrasensitive instruments that need to be operated at conditions met only in specialized laboratories, but also highly specialized sample preparation prior to analysis. Although the absolute chronology of Mars may require calibration (see section 5.5), it is expected that the returned igneous samples from the Jezero Crater floor would be between ~3.7 Ga (as indicated by the crater counting ages of the inlet valley; Fasset and Head, 2008) and ~3.96 Ga (crater counting of the Isidis basin age; Werner, 2008), hence they will help to fill in a large temporal gap observed in martian meteorites between ~2.4 Ga (Herd et al., 2017) and ~4.1 Ga (Lapen et al., 2010). This will place new constraints on the geodynamical evolution of the martian mantle, better defining our view of the geological evolution of the interior of Mars.

It has also been proposed from the study of martian meteorites that the early (and present?) martian mantle was much more chemically heterogeneous than Earth's mantle (Blichert-Toft et al., 1999; Barnes et al., 2020), likely related to the lack of martian plate tectonics (Debaille et al., 2013). The ancient igneous rocks collected by Perseverance can be used to probe the early stages of planetary differentiation, a record that no longer exists on Earth. Several major questions remain unresolved, for example what is the duration of the magma ocean stage, which is estimated to have lasted from 35 Ma (Borg et al., 2003) to 100 Ma (Debaille et al., 2007), how this timing compares to the fast differentiation hypothesized for Mars (Dauphas and Pourmand, 2011), and/or why did Mars transition into a "rigid-lid planet" (Moore et al. 2017). Also, igneous samples representative of a time and location distinct from that recorded by the meteorite record will provide a critical test of the "planetary-scale" mixing line observed in shergottites (Lapen et al. 2017), and whether it actually has global significance, and to address whether or not the origin of the enriched endmember is the martian crust (Humayun et al., 2013; Moriwaki et al. 2017), the late cumulates resulting from the magma ocean solidification (Armytage et al., 2017), or something else entirely.

Future insights from isotopic measurements of these martian rocks can be gained from the variations of stable isotopes of certain metals and halogens (*e.g.,* Li, Cl, Mg, Ca, Fe, and Zn; see Johnson et al. 2004; Teng et al. 2017). These isotopic systems are sensitive to processes such as fractional crystallization, volatile degassing, and hydrothermal alteration and recorded by mass-dependent isotope fraction in igneous rocks (*e.g.,* Tomascak, 2004; Walkins et al. 2009; Teng et al., 2011; John et al. 2012; Paniello et al., 2012; Kang et al. 2017; Bellucci et al. 2017; Simon, 2022). Recent work measuring Ca isotopes, an element that has both multiple stable and radiogenic isotopes, exemplifies the emerging applications of non-traditional stable isotope studies, as Ca isotopes can be used to test interpretations related to both thermal and chemical equilibrium by recording the degree of thermal and/or chemical metamorphism potentially modifying the original composition of the igneous rocks (Antonelli and Simon, 2020). Likewise, the combined measurement of non-traditional and traditional radiogenic elements such as Ca and Nd, that have distinct chemical behaviors, has been used recently to distinguish different planetary source reservoirs (*e.g.,* mantle versus crust) in some terrestrial igneous rocks where the isotopic signature of neither element alone can unambiguously be used to define their source reservoir (Mills et al. 2018).

5.1.4 Volatile abundances in the mantle source region of Jezero Crater floor igneous rocks

The abundance and distribution of H_2O and other volatiles, in the martian interior is a key factor in understanding the thermochemical and geodynamic evolution of Mars (Breuer et al., 2016; Dreibus and Wänke, 1985; Elkins-Tanton, 2008; McCubbin et al., 2008; Ruedas et al., 2013). Additionally, the effects of magmatic degassing are important to climate change and thus planetary habitability. Studies of martian meteorites have demonstrated that H-bearing mineral phases, such as glass within olivine-hosted melt inclusions and the minerals apatite and amphibole, can be used to constrain the abundances of H_2O in martian magmas and magmatic source regions when the hydrous phases can be measured with high-precision methods such as secondary ion mass spectrometry (Usui et al., 2012; McCubbin et al., 2010; McCubbin et al., 2012; Gross et al., 2013). Based on study of martian meteorites, the martian mantle is considered heterogeneous with respect to H_2O abundances (McCubbin et al., 2016; Filiberto et al., 2016; Black et al., 2022), and the prevailing hypothesis is that the martian mantle became progressively drier throughout its history (Balta and McSween, 2013).

Nearly all H_2O estimates from the martian interior come from samples with igneous crystallization ages ≤1.3 Ga. The Noachian ages of the ultramafic-mafic rocks in the collected Máaz and Séítah samples could help to establish additional estimates of the H_2O content of martian magmatic source region(s) at a time for which estimates do not currently exist for Mars. Both phosphates and olivine-hosted melt inclusions have been detected in rocks from Máaz and Séítah (Liu et al., 2022), providing at least two potential pathways to determine parental magmatic water abundances depending on the fidelity of any glass or phosphate phases in the returned samples. Additionally, H_2O abundances in nominally anhydrous minerals, such as the olivine and pyroxene observed in Máaz and Séítah, have been used to study the water contents of mantle source(s), *e.g.,* Peslier et al. (2010). Similar types of volatile measurements in igneous feldspar have been used to estimate magmatic volatile abundances, *e.g.,* Mosenfelder et al. (2015). In combination with other trace element data, the parental magmatic H_2O abundances could be used to estimate H_2O abundances in the mantle source of Mars, similar to H_2O estimates in the interiors of other planetary bodies like the Moon and asteroid 4Vesta (*e.g.,* Saal et al., 2002; Hauri et al., 2015; Simon et al., 2020; McCubbin et al., 2021).

5.2 Secondary mineralogy and geochemistry of Jezero Crater floor bedrock

5.2.1 Aqueous activity recorded by Jezero Crater floor rocks

Investigating the alteration minerals in the returned samples using laboratory-based analyses that have a higher spatial resolution and particular sensitivity to minor phases, trace elements, and isotopes will be key to answering additional questions related to the aqueous activity in both the Séítah and Máaz formations. A better understanding of the samples will allow constraints to be placed upon the past aqueous history of Jezero Crater floor including the timing of this activity in absolute terms as well as relative to the duration of lacustrine activity in Jezero Crater and the conditions of aqueous activity including temperature(s), fluid sources, as well as water distribution, cycling and storage during alteration episodes.

Evidence of aqueous alteration preserved in samples from the crater floor and investigated with high resolution laboratory techniques may indicate a number of generations of fluid alteration (Scheller and Rzzell Hollis et al., 2022; Tice et al., 2022). The primary ultramafic lithology of the Séítah formation appears to have undergone at least three separate episodes of alteration: (1) an earlier carbonation event followed by (2) a later brine event that partially filled the rocks with a complex mixture of sulfate and perchlorate minerals, finely crystalline and possibly amorphous silicates, and chloride minerals, and finally, (3) more recent surface oxidation. Given that olivine was identified as a primary phase in rocks of the Séítah formation (Figs. 8 and 9) and that carbonate was detected as a secondary phase, the Fe- and Mg-phyllosilicates, carbonates, and possible amorphous silica may have resulted from an early stage of water-rock reaction (Brown et al., 2010). Deposition of salt phases is detailed below. The recent surface oxidation is apparent across Séítah (see Rice et al., 2022, this volume) and may be preserved as a weathering rind in the core samples. At least three separate episodes of alteration events are also identified in the primary mafic lithology of the Máaz formation: (1) formation of phyllosilicates, (2) salt precipitation including void filling, and (3) later oxidative weathering.

The relative abundances and compositions of the secondary mineralogy in the Máaz formation appear to be distinct from the Séítah formation, and more variable. The deposition of salt phases varies within the Maaz formation with most of the salts identified in the lower Máaz formation absent from the upper Máaz formation (*i.e.,* Alfalfa). In contrast to the Séítah formation, the Fe- and Mg-phyllosilicates detected in the Máaz formation are likely to be serpentine group minerals and are found in association with fayalite and there is little to no associated carbonate.

Observations of salt minerals indicate the presence of saline solutions at some point in the geologic history of both the Séítah and Máaz units. Such solutions may have resulted from concentration by evaporation and these salt mineral phases may be the last evidence of water in Jezero Crater. If true, trace element and isotopic analyses of the salt minerals that appear more abundant in the lower Máaz members, possibly exemplified by those seen in the disaggregated Roubion target, will provide important constraints for the past aqueous environment(s) within Jezero Crater. Jezero samples generally have a Cl/S ratio (atom/atom) greater than 1.0; this is in contrast to martian global soils and almost all previous rocks and sediments analyzed on Mars which have Cl/S ~ 0.25 or lower (Yen et al. 2006). The predominance of chlorine over sulfur may indicate the progressive enrichment in residual brines of highly soluble chlorides and oxychlorines following sulfate deposition in the Jezero lacustrine environment. Mineral dissolution rates in the presence of brines have been shown to be much slower than in more dilute waters (Pritchett et al., 2012; Olsen et al., 2015; Steiner et al., 2016). Therefore, the rate of alteration of these rocks is dependent on the chemistry of the reacting fluid. Laboratory analyses that can help determine characteristics of the reacting fluids will help constrain the rate of alteration (Fig. 17).

The record of distinct aqueous environments, such as brines versus dilute waters, can be interpreted by examining returned samples. If the voids present in the sampled rocks formed by dissolution, estimates of the duration of the presence of liquid water can be calculated under different conditions using mineral lifetimes after Lasaga (1998) (Eq. 1; Fig. 17).

$$T = \frac{d}{Vr} \qquad \text{(Eq. 1)}$$

where t = the mineral lifetime in years, d = the grain diameter in m, V = the molar volume of the mineral, and r = the mineral dissolution rate. For the calculations presented in Figure 17, grain diameters were assumed to be 1 mm, the molar volume of forsterite and fayalite were taken from

Robie et al., (1979), and dissolution rate laws of forsterite were taken from Bandstra and Brantley (2008), based on rates and published activation energies for olivine (Oelkers, 2001 and references therein). These results clearly show that olivine is expected to persist for different lengths of time under different pH and temperature conditions, as well as different conditions such as the activity of water, grain size, and the lab-field effect.

5.2.2 Planetary evolution of aqueous environments

The study of secondary mineral phases can also provide insights into planetary-scale processes and environments where rocks interact with water. The ability to interpret the geochemical processes and paleoenvironments of Jezero Crater from mineral assemblages and compositions may provide direct links to understanding similar rocks and mineral assemblages outside of the crater. Similarly, if investigation of orbital data and/or data from the extended mission were to reveal a stratigraphic relationship between units inside and outside of Jezero, the geochemical and environmental interpretations made from alteration phases in returned samples could help to constrain the broader geographic distribution of water.

The extent of interconnectivity of the hydrologic system at different points in martian history, including the potential for communication between surface and subsurface components of the system, remains an open question in planetary science (Carr and Head, 2010). Higher resolution investigation of the secondary mineral assemblages in the returned samples and the elemental composition of those minerals may reveal the presence of mineral phases and/or relationships between mineral phases that were not observable by the *in situ* instrumentation. This information will help address whether the samples experienced open or closed system alteration, *cf.* Clavé et al. (2022, this volume). Further constraining the fluid source and environment of alteration is key for understanding the potential habitability of any past water/rock systems. Sample measurements that would help constrain the near surface environmental conditions of Jezero Crater include: (1) Isotopic measurements of secondary minerals in returned samples to potentially distinguishing the source of reactant fluids (*e.g.,* magmatic, groundwater, atmospheric). (2) Robust determination of alteration by atmospherically derived fluids would provide insights into the martian climate. (3) Measurement of alteration by groundwater to constrain the duration of the presence of groundwater and the temperatures at which alteration occurred, with implications for the potential habitability (section 5.4) of subsurface water/rock systems. (4) Comparison of the aqueous alteration in returned samples with aqueous alteration observed in other locations on Mars (*e.g.,* salts and veins observed with Mars Science Laboratory) to help shed light on the past global history of Mars.

5.3 Martian atmospheric composition

The relatively thin modern atmosphere of Mars evolved from one that was thick enough, in the past, to have supported liquid water at the surface. Its evolving elemental and isotopic compositions reflect the cumulative history of planetary outgassing, atmospheric escape, volatile-bearing mineral precipitation, and impacts (Lammer et al. 2013). There is an inherent scientific interest in returning an atmospheric sample (Jakosky et al 2021; Swindle et al., 2022), as well as, ancient rocks that likely contain a record of this history, *e.g.,* Usui et al. (2012, 2015). The analysis of the martian gas will allow comparisons of noble gases (Xe, Kr, Ar, Ne) and light elements such as H, C, N, and O to the values of the elements in the solid samples of ancient Mars returned to Earth within the same cache collection, analyzed in martian meteorites, and studied by surface landers such as MSL (SAM *in situ* analysis). Although we have volatile measurements in recently (< 1 Ma) formed impact glasses contained within martian meteorites, the gases sampled do not reflect unadulterated atmosphere–they include a combination of atmospheric, mantle, and spallation (in space) contributions (Bogard and Johnson, 1983; Bogard et al., 2001; Usui et al., 2012, 2015).

All sealed tubes contain a small amount of headspace gas, above the rock sample, captured inside the tube as the sample is sealed. During the attempt to seal the Roubion sample, no core was acquired, and the contents of this sealed tube thus consists only of martian air (with the exception of a few grains/dust remnants from the drilled rock). The estimated amount of martian atmosphere gas in the Roubion sample is: $4.9x10^{-6}$ mol, whereas for the other samples, with a full length (~6 cm) core, the number of moles may be approximately 1.0 to 1.3×10^{-6} mol (see Table 2, Supplement III). Although relatively small for many current analytical methods, future advancements in sample analyses are expected to maximize sample return science of gas volumes of this size.

5.4 Habitability and astrobiological potential

5.4.1 Organic materials in Jezero igneous rocks

The structure, abundances, distribution, and isotopic composition of organic compounds in samples returned from Jezero Crater will be examined with the goal of understanding the martian carbon cycle and assessing the possibility of a past martian biosphere. Organic compounds have been detected in various martian meteorites (McKay et al., 1996; Sephton et al., 2002; Steele et al., 2012; 2016; 2022) and materials and lithologies from Gale Crater that were analyzed *in situ* (Freissinet et al., 2015; Eigenbrode et al., 2018; Millan et al., 2022). Although not considered the prime astrobiology targets of the mission, analyses of Jezero Crater floor samples may nonetheless enable the reconstruction of abiotic, prebiotic or biological processes that either synthesized the organics *in situ* or delivered them to the samples from endogenous (*i.e.,* martian) or exogenous (*i.e.,* asteroids and comets) sources (Flynn, 1996).

The collected cores, like igneous rocks studied from Earth, can preserve organic compounds primarily in the zones altered by fluids (*e.g.,* Klein et al., 2015), or as minute fluid inclusions that contain methane with a high-temperature origin (Klein et al., 2019; Zhang et al., 2021; Etiope and Whiticar, 2019; Reeves and Fiebig, 2020). The crater floor samples have measurable abundances of organics: deep UV fluorescence measured by the SHERLOC instrument shows evidence of possible single- and double-ring aromatic organic compounds (Farley et al., 2022; Scheller and Razzell Hollis et al., 2022). Multiple possible detections of aromatic organic materials have also been made by SHERLOC deep-UV Raman spectroscopy. Overall, Raman and fluorescence spectra revealed very low abundances of organics, where detected, comparable to those detected in Gale Crater, and often in association with salts and grain boundaries, suggesting the emplacement of organics during diagenetic episodes (see Sharma et al., 2022; Murphy et al. 2022; Corpolongo et al., this volume). These results provide insight into the distribution of minor/trace amounts of organics, but more robust interpretations based on mapping the distribution and characterizing the composition of organic matter present in either igneous or alteration phases of the samples from Jezero Crater floor will require techniques with nano- to micrometer scale spatial resolution and the ability to detect and determine the chemistry and structure of organic molecules. This highlights the need for return of these samples to interrogate the molecular structure of these compounds within, thereby understanding their formation, alteration, and degradation histories. Laboratory analyses of these samples and collected witness tubes could also help to establish the background content of organic material at the martian surface and in the subsurface. Such samples are required for comparisons of processes that have cycled carbon in the biosphere, hydrosphere and geosphere on Earth and any counterparts on Mars.

5.4.2 Astrobiological potential of observed salts

Phanerozoic salts such as sulfate and chloride on Earth can preserve organic compounds and fossils (*e.g.,* Benison and Bowen, 2006). They can also reliably archive characteristics of the paleo-depositional environment, as evidenced by the more than one-billion-years-old Paleoproterozoic sulfate deposits that have been used to probe seawater chemistry (*e.g.,* Blattler et al 2018). Salts, including those implicated in prebiotic surface-based chemical reactions on Earth (*e.g.,* Benner et al., 2018), are typically found in large scale evaporite deposits that have not, thus far, been detected in Jezero Crater. Salts in the returned samples from Séítah (namely from Issole, the Robine and/or Malay cores) should be examined for the presence of fluid inclusions and organic matter. The potential of salts to record past fluid chemistry and preserve inclusions also motivates the search for more extensive salt deposits in the delta stratigraphy and areas outside of the Jezero Crater floor.

5.4.3 Carbonated olivine, source of H_2 and energy for life

Olivine carbonation-serpentinization processes occurring where water interacts with igneous minerals and changes the redox state of iron to generate hydrogen occur on Earth and are thought to be common throughout the Solar System, including Mars (Steele et al., 2022). These processes are indicated by *in situ* observations of Séítah rocks. Molecular hydrogen produced by these reactions can serve as an electron donor for microbial metabolic activities such as sulfate reduction and methanogenesis (Madigan et al., 2017). Exploration for environments and samples that were extensively altered in this manner will continue as Perseverance traverses the marginal deposits and portions of the delta that contain carbonate.

5.5 Geochronology and paleomagnetism recorded in altered igneous rocks

Many of the science questions at Jezero Crater involve sequences of events and temporal evolutions over geologic timescales; these can be addressed with geochronology and paleomagnetic observations of returned samples of igneous rocks and their alteration products. For example: What is the history of igneous differentiation on Mars? What was the timing of aqueous activity in the Jezero Crater region? What is the history of the magnetic field on Mars, and how does the occurrence of a dynamo correlate with our knowledge of the martian atmosphere through time? What is the erosional and exhumation history of Nili Planum? What is the erosional history of the Jezero delta since its deposition?

5.5.1 Timing of igneous activity

The genetic relationship between Máaz and Séítah and between both units and the deltaic rocks is uncertain. The most straightforward interpretation is one where Séítah represents the oldest exposed crater floor unit. An alternate interpretation, consistent with its coarse-grained texture, is that Séítah represents an igneous sill or laccolith (Farley et al., 2022; Liu et al. 2022). In this case, Séítah could be younger than overlying Máaz, and injected into or below it. Whether an intrusion or slowly cooled lava, it is also unclear from field observations whether the contact between Séítah and Máaz represents a disconformity, or instead whether Máaz is a cogenetic, less mafic complement to a more mafic Séítah (Farley et al., 2022; Wiens et al. 2022). Furthermore, it is unknown whether Máaz and Séítah underlie or embay/intrude the delta. These issues can be directly tested by quantifying the crystallization ages of each formation. Since both formations are very likely to have crystallized after Jezero Crater formed, their crystallization ages will also provide a lower bound on the age of Jezero Crater itself.

The igneous rock samples collected from the Jezero Crater floor are each well-suited for geochronology and can therefore help to establish the absolute and relative timing of igneous activity in the region. Interpreted as primary igneous rocks, these samples each contain a diversity of minerals and grain sizes (Farley et al. 2022; Liu et al., 2022, Wiens et al. 2022); including pyroxene, plagioclase, and likely accessory minerals that can be used to quantify the timing of their crystallization using parent-daughter systems such as K-Ar and U-Th-Pb. In addition, these same phases should enable thermochronology studies, *e.g.,* $^{40}Ar/^{39}Ar$ and (U-Th)/He), for quantitative constraints on post-crystallization cooling rates and exhumation history, which can inform models of their original emplacement depths.

5.5.2 Timing of aqueous history

The temperatures and pressures at the surface of Mars today preclude the stability of liquid water for all but brief durations, yet there is clear evidence that liquid water has substantially modified the surface topography of Mars in the geologic past (*e.g.,* Carr and Head, 2010), including the inlet and outlet channels and delta sedimentary deposits observed at Jezero Crater (*e.g.,* Mangold et al., 2021). Because extended durations of liquid water stability are understood to be a requirement of the emergence of biological activity (Westall and Brack, 2018), some of the most important science questions at Jezero Crater relate to when, and for how long, liquid water was present: When were the delta sediments deposited, and thus, when was a lake present? How many sediment-delivery and lake-filling events occurred? Over what duration was the delta sediment deposited? In addition to these questions on the geomorphic evolution of the Jezero lake and delta, the timing of the secondary aqueous activity that appears to have modified the igneous rocks exposed at the crater floor will be addressed. Science questions include: When and over what durations did these aqueous alteration occur? Did chemical alteration of crater floor rocks occur when, or shortly after, the lake was present, or much later? Could the local conditions involving aqueous activity and rock alteration have supported biological activity?

Quantifying the timing, duration(s) and frequency of aqueous activity within Jezero Crater are among the most important objectives to be addressed with return sample science. These directly relate to questions on when, and for how long, environmental conditions for prebiotic activity, and potentially microbial life itself, may have once existed at Jezero. The samples collected from Séítah and Máaz can be used to quantify the timing of aqueous activity in two distinct ways: (i) by providing bounds on delta deposition timing, thus the timing of Jezero lake filling event(s); and (ii) via geochronology applied to secondary chemical alteration phases present in the samples, such as oxides and carbonates.

Regional observations from orbit (Gouge et al., 2015) and rover observations indicate that the Séítah formation most likely underlies the main Jezero delta. The occurrence of Séítah rocks between the main delta and its remnant Kodiak, and a lack of obvious high-temperature alteration or related geomorphic expressions at the contact/zone between Séítah and the delta front support the interpretation that Séítah crystallization predated the delta deposition. If so, the crystallization age of Séítah will provide an upper bound on the timing of deposition of the main delta. Further, this assumed stratigraphic relationship can be tested using returned sample analyses of delta sediments collected near the contact, *i.e.,* high-temperature contact alteration/metamorphism, partially reset parent-daughter systems (*e.g.,* K-Ar) in detrital phases, and by paleomagnetic “conglomerate” tests.

The stratigraphic relationship between Máaz and the delta is presently less clear (*e.g.,* Farley et al. 2022, Wiens et al. 2022). If Máaz is shown to also occur below the delta, its crystallization age would also provide an upper bound on delta deposition timing; however, if Máaz formed much later than Séítah, it possibly embayed a pre-existing delta, in which case its crystallization timing would provide a lower bound on delta emplacement. Observations of detrital delta sediments near Máaz can be used to test these competing relationships by seeking evidence of high-temperature alteration and/or partially reset geochronology systems near the contact. If Máaz emplacement occurred after delta deposition, we would expect thermochronological observations of proximal detrital sediments to be concordant with, or trending towards, the timing of Máaz crystallization, as determined by methods listed above in section 5.5.1.

Geochronology applied to secondary phases (*e.g.,* Fe-oxides, carbonates, phyllosilicates) interpreted as post-crystallization alteration products (Tice et al. 2022; Scheller and Razzell Hollis et al. 2022), could quantify the timing of the alteration conditions. Laboratory applications of geochronology to such secondary alteration phases has been successful, but also involves complexities of polymineralic materials and open system behavior (*e.g.,* Shuster et al., 2005; Shuster et al., 2012). However, if the alteration conditions involved liquid water, such geochronology could quantify the timing, and possibly duration, of late-stage aqueous activity at the Jezero floor. For example, geochronology using returned samples could establish whether that alteration occurred shortly after igneous emplacement (in which case, we expect concordance between secondary and primary phase crystallization timing), or much later than the original Séítah and Máaz crystallization, perhaps associated with water delivery during delta emplacement.

5.5.3 Mars cratering chronology calibration

With the exception of *in situ* geochronology conducted at Gale Crater (Farley et al., 2014), all absolute knowledge of the timing of geologic events and features observed at the surface of Mars depends on impact cratering chronology functions that have been empirically determined from observation of the lunar surface and geochronology of returned Apollo samples, then extrapolated to Mars. This extrapolation depends critically on several assumptions about: (i) the relative fluxes of bolides to Mars and the Moon, (ii) the relative crater diameters formed on

Mars and the Moon for a given bolide size, and (iii) that the time dependency of martian cratering history relative to the Moon.

Samples collected from Jezero crater can help to test these important assumptions and possibly provide opportunities to empirically determine the assumed parameters used for Moon-Mars extrapolations. Such tests will be important for all quantitative applications of the martian cratering chronology across the entire planet. However, such tests require knowledge of how long a particular surface was exposed to crater-forming impact events; this will not generally be equal to the time since an igneous rock crystallized on a planetary surface that has experienced active geomorphic processes. Indeed, the spatial distribution of crater densities observed at the Jezero crater floor clearly indicates that the igneous rocks have also experienced a complex exhumation history, both spatially and temporally, with lowest densities observed near the delta, highest to the NE of the landing site (Quantin-Nataf et al., 2021). Any tests or calibrations of the crater chronology function will require knowledge of when, and at what rate, this post-crystallization exhumation occurred, and more generally, how a rock crystallization age can be related to the duration of crater accumulation at a particular surface.

As the highest stratigraphic expression of the crater floor rocks observed by Perseverance, the Máaz formation (*i.e.,* Ch'ał member) is most closely associated with crater densities observed across the crater floor. Thus, the timing of Máaz crystallization, which should be readily determinable using numerous methods of geochronology (*e.g.,* U-Pb, $^{40}Ar/^{39}Ar$) will provide an important upper bound on the duration of crater accumulation, assuming the rocks exposed across the crater floor, off to the East of the region explored by Perseverance, are equivalent. However, since the crater floor has likely experienced post-crystallization exhumation, sedimentary burial, and subsequent exhumation, the quantitative relationship between the Máaz crystallization age and a crater accumulation duration is non-trivial; these two timescales may differ by orders of magnitude. Because the highest crater densities on the Jezero Crater floor, *i.e.,* the mapped Cf-Fr unit (*cf.* Stack et al., 2020), occur farthest from the delta (near Hartwell Crater; Quantin-Nataf et al., 2021), it is likely that this surface experienced the least burial and subsequent exhumation since crystallization. Thus, assuming the rocks exposed near Hartwell Crater are equivalent to upper Máaz, use of the crater density and size distribution observed near Hartwell with the crystallization age of Máaz would provide quantitative constraints on two of the key assumptions in the Mars cratering chronology, specifically the ratios of the bolide fluxes and crater diameters, respectively, between Mars and the Moon. However, due to complexities and uncertainty on the exhumation history and rates of aeolian processes that have modified the surface through time, such an analysis using the Máaz crystallization timing would provide lower bounds on these ratios. In addition, if the Séítah rocks are shown to be the equivalent of the regional olivine carbonate (Goudge et al., 2015; Mandon et al. 2020; Brown et al., 2020), other potential cratering chronology constraints may be possible using crater densities on surfaces outside Jezero Crater.

5.5.4. Dynamo history

Mars today does not have a dynamo (a global magnetic field inductively generated by convection of its metallic core); however, the discovery of remanent magnetization in the martian crust by the Mars Global Surveyor and the Mars Atmosphere and Volatile Evolution mission (MAVEN) spacecraft and in martian meteorites from laboratory measurements indicate that Mars once had a dynamo early in its history. Crater counting age estimates of surfaces of the magnetized crust (Vervelidou et al. 2017) and $^{40}Ar/^{39}Ar$ ages of the martian meteorite Allan Hills 84001 (Weiss et al. 2004) suggest that a dynamo may have been present from the pre-Noachian until the Early Hesperian. At present, however, the intensity of the dynamo is essentially unconstrained and its lifetime uncertain by at least hundreds of Ma.

Determining the history and nature of the dynamo is important for several reasons. First, a strong dynamo may have prevented atmospheric loss, such that its decline may have played a central role in the transition from warmer and wetter conditions, *i.e.,* possibly more habitable conditions in the Noachian, eventually reaching the cold and dry conditions of today. Second, the dynamo history reflects the thermal evolution of the planetary interior including the crystallization of the core and mantle convection. Finally, the direction of the magnetic field as recorded by rocks can be used to test the hypothesis that Mars experienced plate tectonics and true polar wander, and to determine whether its dipole component underwent reversals. As such, establishing the history of the intensity and direction of the magnetic field through combined geochronology and paleomagnetic datasets using oriented rock cores from the Jezero Crater is a key goal of future returned sample studies.

The science objectives for paleomagnetic investigations require samples containing sufficiently abundant ferromagnetic minerals that can acquire remanent magnetization that is stable over billions of years. Laboratory analyses of martian meteorites (Gattacceca et al. 2014), and *in situ* compositional (Wiens et al. 2022), mineralogical (Morris et al. 2006), and magnetic properties measurements (Madsen et al. 2009) suggest that the mafic and ultramafic lithologies of Máaz and Séítah likely contain abundant minerals, *e.g.,* magnetite, that should be capable of recording stable paleomagnetic records. If all these samples retain primary igneous ferromagnetic oxides, this will enable paleointensity studies. Furthermore, the six cores taken from likely in-place bedrock (but even potentially the two collected at Rochette that appear to have small likely quantifiable displacement), can be used for paleodirectional studies of the magnetic field. Given that the 6 (+2?) samples were collected from bedrock with varying attitudes (with surface normals ranging over ~15 degrees), the relative age of their remanent magnetization relative to bedrock tilting could be established using a fold test: if the magnetization directions of samples of similar formation age are more (or less) clustered after tilt correction, this would be consistent with the hypothesis that their magnetization predates (or postdates) tilting.

6. Summary

The Perseverance rover recently completed a traverse of the floor of Jezero Crater, Mars, characterizing and collecting samples from the Séítah and Máaz formations. Eight rock samples and one atmospheric sample were collected and stored in the rover. Accompanying *in situ* science observations using the rover's onboard payload offer information about the composition, mineralogy, and texture of the sampled rocks. These rocks represent the first samples from Mars with known and characterized geologic context, the first collected with potential to be returned to Earth for laboratory analysis, and the first samples from rock outcrop collected on another planet.

The suite of the Séítah and Máaz formation samples collected by Perseverance represents a paradigm-shifting outcome of the Perseverance Crater Floor Campaign that will address several important objectives of the Mars Sample Return Campaign, including magmatic history, water-rock interactions, environmental conduciveness to life, and isotopic ages for geologic events. Perseverance is now beginning its exploration of the delta facies and is expecting to make a cache that includes a representative set of Jezero Crater floor samples at the Three Forks depot by early 2023.

Acknowledgements

The authors thank editor Bradley Thomson and reviewers Nicole E. Moore, Jade Star Lackey, and Allan Treiman for their many constructive comments. We are grateful to the entire Mars 2020 team. The Mars 2020 mission and Return Sample Science Participating Scientist Program are supported by NASA Mars Exploration Program. K.H.-L. acknowledges a UK Space Agency Aurora Research Fellowship (grant no. ST/V00560X/1). M.-P.Z. is supported by Grant PID2019-104205GB-C21 funded by MCIN/AEI/ 10.13039/501100011033. J.F.B. is supported by NASA/JPL, grant 1511125. A.G.F is supported by European Research Council, Grant #818602; F.G. is supported by INTA internal project DAXE (SIGS22001) and Italian Space Agency (ASI) grant agreement ASI/INAF n. 2017-48-H-0. C.D.K.H. and M.S. are supported by Canadian Space Agency Mars 2020 Participating Scientist Grants. S.S. is supported by Swedish National Space Agency (contracts 137/19 and 2021-00092). A.U. is supported by NASA Mars 2020 Participating Scientist program 80NSSC21K0330 (AU). S.V. is supported by NASA Mars 2020 Participating Scientist Program (Grant: 80NSSC21K0328). A.J.W. is supported by NASA Mars 2020 Participating Scientist Program (Grant: 80NSSC21K0332).

Open Research

This contribution includes a variety of geospatially located data, including context far-field and workspace images (Mastcam-Z, Figs. 3-7; Figs. S2-10 color anaglyphs, Fig. S11 context mapping, NASA PDS doi:10.17189/q3ts-c749), subsurface radar data (RIMFAX, Figs. 3-7, NASA PDS doi:10.17189/1522644), rock target close up images (WATSON, Figs. 8, 9, 12, and 13; Table S1, NASA PDS doi:10.17189/1522643), sample core images (CacheCam, Fig. 2, NASA PDS doi:10.17189/q3ts-c749), major element compositional laser ionization breakdown spectroscopy (SuperCam-LIBS, Fig. 11, Tables S2-6, NASA PDS doi:10.17189/1522646), X-ray fluorescence measurements that allow compositional mapping (PIXL, Figs. 9, 10, and 13; Figs. S12-16 distorted WATSON ACIs merged with X-ray fluorescence maps of SiO_2, Al_2O_3, and SO_3 abundance and distribution; and bulk sum analyses, Table 4, NASA PDS doi:10.17189/1522645), hydration and alteration phase identification by visible and infrared spectroscopy (SuperCam-VISIR, Fig. 14, NASA PDS doi:10.17189/1522646), mineral and organic compound identification and mapping (SHERLOC-Raman/Fluorescence, Fig. 15, NASA PDS doi:10.17189/1522643), and atmospheric conditions at the time of sampling Roubion, the atmospheric sample (MEDA, Fig. S1, NASA PDS doi:10.17189/1522849). All of the information and data presented in this contribution are included in the main text and associated supplemental information. Rover instrument and calibration details can be found in the instrument payload citations included in the primary text (and references therein). Operational details, initial sample reports, and all *in situ* payload measurements are uploaded to NASA Planetary Data System.

Figures

Figure 1. Crater Floor Science Campaign area explored by the Perseverance rover: (A) Inset shows western edge of Jezero Crater, location of Three Forks sample depot, and explored region in yellow box. (B) HiRISE image shows the location of outcrop sample targets and rover path. Octavia E. Butler (OEB) landing site, first witness sample location, and prominent crater floor features are labeled.

Figure 2. Samples from Jezero Crater floor collected by Perseverance: CacheCam images of rock sample cores from Séítah and Máaz units and tube of atmospheric gas prior to sealing. Core diameters are approximately 1.3 cm. Notional and alterative crater floor stratigraphic relationships of sampled units shown for reference (see Crumpler et al., 2022; Horgan et al., 2022).

Figure 3. Mastcam-Z workspace mosaics and interpreted RIMFAX subsurface for Brac: The Séítah formation outcrop target at the highest elevation reached by Perseverance and possibly the oldest sample collected. (A) View looking north of the Content member that appears to be lying unconformably on top of the Bastide member (see text). (B) Sloped-surface within Brac where Dourbes abrasion was made is approximately 10 cm from top-to-bottom.

Figure 4. Mastcam-Z workspace mosaics and interpreted RIMFAX subsurface for Issole: The Séítah formation outcrop target near the Séítah/Máaz contact. (A) Sample borehole (~1.3 cm diameter) and Quartier abrasion site (~5 cm diameter) in workspace image provide scale of targeted outcrop features. (B) View of Issole looking south from Séítah towards base of the Artuby Ridge (not seen).

Figure 5. Mastcam-Z workspace mosaics and interpreted RIMFAX subsurface for Roubion: The Máaz formation outcrop target at the lowest elevation reached by Perseverance and the first sample target where the sample disaggregated, and an atmospheric sample was collected. (A) Shows low-lying Roubion member and exposure of rough, layered, and rubbly upper Máaz outcrop named Mure in the distance. (B) Nearfield outcrop scale indicated by Guillaumes abrasion and borehole of Roubion as in Fig. 4.

Figure 6. Mastcam-Z workspace mosaics and interpreted RIMFAX subsurface for Rochette: The Máaz formation outcrop target on top of Artuby Ridge and the first successful sample collected. (A) Shows Rochette that forms part of a NW—SE-trending band of similar boulders. (B) Rochette in which Bellegarde abrasion site and boreholes provide scale as in Fig. 4.

Figure 7. Mastcam-Z workspace mosaics and interpreted RIMFAX subsurface for Sid: The uppermost Máaz formation outcrop target that lies directly on top of Nataani and likely represents the youngest sample collected. (A) View looking east shows massive rocks of the Ch'ał member that form hummocks and ridges outcropping east of the OEB and the southward traverse to Mure. (B) Nearfield outcrop scale of Sid indicated by Alfalfa abrasion as in Fig. 4.

Figure 8. WATSON (~25 cm standoff) image paired with a quad of Mastcam-Z multispectral images for Séítah formation abrasion sites: (A): L256 enhanced color, where white indicates abraded olivine or salts, red indicates oxidized grains, and dark blue to gray grains are unaltered mafic minerals (olivine, pyroxene, and oxides). (B): L256 decorrelation stretch highlights these color differences. (C): Band depth in L5 (528 nm) relative to shoulders at L6 (442 nm) and L4 (605 nm), typically indicating iron oxides (crystalline and nanophase). (D): Mafic parameter combination, where red = R0R/R1 (630/800 nm); green = band depth at 910 nm; blue = R1/R5 (800/978 nm). Dourbes shows clear rounded olivine grains (magenta) surrounded by pyroxene (blue). Quartier shows similar relationships but with possible cm-scale layering, based on the strong dark stripe with more pyroxene signatures across the center of the site, indicating layer-to-layer differences in olivine versus pyroxene abundances.

Figure 9. Close up observations of Séítah abrasion sites by WATSON (~4 cm standoff), ACI, and PIXL: Compositional X-ray map of SO_3 (red), SiO_2 (green), Al_2O_3 (blue) concentrations, generally correspond to primary olivine (ol) = dark green and pyroxene (pyx) =

light green, compositionally evolved intercumulus mesostasis (meso) = blue and secondary sulfate (s) = red, respectively (see text and Appendices IV & V for additional information).

Figure 10. Abrasion site PIXL data: Plotted by pixel and as bulk sum composition (blue circle) on a ternary diagram of molar abundances Al_2O_3–(CaO+Na_2O+K_2O)–(FeO_T+MgO). Common primary igneous minerals (olivine, pyroxene, feldspar, Fe-Ti-oxides) are typically found within dashed red inner triangle area whereas common clay minerals fall above the upper red dashed line. Several additional secondary minerals (*e.g.,* Fe-Mg-Ca-sulfates/carbonates, halite) are also plotted for reference.

Figure 11. SuperCam-LIBS total alkalis versus silica plots for natural and abraded surfaces of rocks sampled during the Crater Floor Campaign: (A) laser spot data from natural surfaces of "upper Máaz", "lower Máaz", Séítah, and Content. (B) laser spot data from within abrasion sites. The individual data points represent ~250 μm LIBS laser spots and therefore represent a mixture of one or more primary and secondary minerals. Endmember igneous mineral compositions shown as diamonds and lines for those with solid solution for reference. The underlying igneous classification scheme does not apply to the individual data points and simply provides a frame of reference for comparing samples (data included in Supplement VI). Color coding of sample symbols matched to those of stratigraphic column units shown in Fig. 2.

Figure 12. WATSON (~25 cm standoff) image paired with a quad of Mastcam-Z multispectral images for Máaz formation abrasion sites: (A): L256 enhanced color, where red indicates oxidized grains, light-toned grains are salts or feldspar, and dark blue to gray grains are unaltered mafic minerals (pyroxene and oxides). (B): L256 decorrelation stretch highlights these color differences. (C): Band depth in L5 (528 nm) relative to shoulders at L6 (442 nm) and L4 (605 nm), typically indicating iron oxides (crystalline and nanophase). (D): Mafic parameter combination, where red = R0R/R1 (630/800 nm); green = band depth at 910 nm; blue = R1/R5 (800/978 nm). Alfalfa is dominated by hematite and unoxidized pyroxenes (green and magenta/blue), Guillaumes exhibits low spectral contrast due to weathering (black), and Bellegarde is dominated by Fe-rich pyroxenes (magenta/red).

Figure 13. Close up observations of Máaz abrasion sites by WATSON (~4 cm standoff), ACI, and PIXL: Compositional X-ray map of SO_3 (red), SiO_2 (green), Al_2O_3 (blue)

concentrations, generally correspond to primary pyroxene (pyx) = light green, plagioclase (pl) = blue, and Fe-silicate/alt. olivine (Fe/alt) = green and secondary sulfate (s) = red, respectively (see text and Supplement IV & V for additional information). Colorized ACI used to improve image clarity for Guillaumes because of lighting conditions.

Figure 14. SuperCam mean visible and infrared reflectance spectra of the abraded rocks sampled during the Crater Floor Campaign: The main band attributions are annotated (see Mandon et al., 2022, this volume). Parts of the spectra are shown at lower opacity near ~2 µm owing to possible residual atmospheric CO_2 bands and past ~2.5 µm where calibration is uncertain (Royer et al., 2022, this volume).

Figure 15. SHERLOC analysis of abrasion targets: (A) Bellegrade, (B) Quartier, and (C) Guillaumes showing a diversity of organic and alteration minerals detected in Máaz and Séítah. Panels (A) and (B) starting top left show colorized ACI (red squares indicate outlines of scan areas and white circles regions of interests), fluorescence maps with region of interest (ROIs), fluorescence spectra from ROIs, and Raman maps with confidently detected minerals indicated by colored circles. In panel (C), the top image is a colorized ACI image (the red square indicate outline of the scan area), while the bottom is a Raman map with confidently detected minerals indicated by colored circles. In each of the Raman maps, note that the filled colored circles are much larger than the ~100 µm analysis spots (indicated by the small, unfilled red circles).

Figure 16. Schematic geodynamical evolution of the martian interior: Radiogenic ingrowth of $^{143}Nd/^{144}Nd$ depends on the variation in Sm/Nd in the reservoirs. The progressive solidification of the magma ocean resulted in several depleted reservoirs (in green) and ended up with enriched late cumulates (in brown), after Debaille et al. (2007). From the depleted martian mantle, a crust has been extracted, that is enriched in incompatible trace elements, as observed in NWA 7034 (Armytage et al., 2018). Depleted shergottites (in blue) directly sample a depleted reservoir while the enriched shergottites (in violet) represent a mixture (in pink) between depleted and enriched reservoirs.

Figure 17. Plot of mineral lifetimes for waters of varying pH: For 1 mm diameter grains of forsterite (Fo) and fayalite (Fa) at temperatures of 0, 25, and 50 degrees C at pH values ranging from 1 to 12 based on laboratory dissolution rates, also showing the effect of grain size, activity

of water, and the lab-field effect. These types of calculations indicate the range of mineral lifetimes that can persist under different aqueous conditions.

References

Allwood, Abigail C., Lawrence A. Wade, Marc C. Foote, William Timothy Elam, Joel A. Hurowitz, Steven Battel, Douglas E. Dawson, et al. (202) "PIXL: Planetary Instrument for X-Ray Lithochemistry." *Space Science Reviews* 216, 134. https://doi.org/10.1007/s11214-020-00767-7.

Antonelli, M.A., Simon, J.I. (2020) Calcium isotopes in high-temperature terrestrial processes, *Chemical Geology* 548, 119651.

Armytage, R.M.G., Debaille, V., Brandon, A.D., Agee, C.B. (2018) A complex history of silicate differentiation of Mars from Nd and Hf isotopes in crustal breccia NWA 7034. *Earth and Planetary Science Letters* 502, 274-283.

Alwmark, S, Horgan, B., Udry, A., Bechtold, A., Fagents, S., Ravanis, E., Crumpler, L., Schmitz, N., Cloutis, E., Brown, A., Flannery, D., Gasnault, O., Grotzinger, J., Gupta, S., Kah, L., Kelemen, P., Kinch, K., Núñez, J. (submitted) Diverse Lava Flow Morphologies in the Stratigraphy of the Jezero Crater Floor, *J. Geophy. Res.*, this volume.

Balta, J.B. and McSween, H.Y. (2013) Water and the composition of Martian magmas. *Geology* 41, 1115-1118.

Bandstra, J.Z., Brantley, S.L. (2008) Data Fitting Techniques with Applications to mineral dissolution kinetics, in: Brantley, S.L., Kubicki, J.D., White, A.F. (Eds.), Kinetics of Water-Rock Interaction, pp. 211-257.

Barnes, J.J., McCubbin, F.M., Santos, A.R., Day, J.M.D., Boyce, J.W., Schwenzer, S.P., Ott, U., Franchi, I.A., Messenger, S., Anand, M. and Agee, C.B. (2020) Multiple early-formed water reservoirs in the interior of Mars. *Nature Geoscience* 13, 260-264.

Beaty, D.W., Grady, M.M., McSween, H.Y., Sefton-Nash, E., Carrier, B.L., Altieri, F., Amelin, Y., Ammannito, E., Anand, M., Benning, L.G., Bishop, J.L., Borg, L.E., Boucher, D., Brucato, J.R., Busemann, H., Campbell, K.A., Czaja, A.D., Debaille, V., Des Marais, D.J., Dixon, M., Ehlmann, B.L., Farmer, J.D., Fernandez-Remolar, D.C., Filiberto, J., Fogarty, J., Glavin, D.P., Goreva, Y.S., Hallis, L.J., Harrington, A.D., Hausrath, E.M., Herd, C.D.K., Horgan, B., Humayun, M., Kleine, T., Kleinhenz, J., Mackelprang, R., Mangold, N., Mayhew, L.E., McCoy, J.T., McCubbin, F.M., McLennan, S.M., Moser, D.E., Moynier, F., Mustard, J.F., Niles, P.B., Ori, G.G., Raulin, F., Rettberg, P., Rucker, M.A., Schmitz, N., Schwenzer, S.P., Sephton, M.A., Shaheen, R., Sharp, Z.D., Shuster, D.L., Siljeström, S., Smith, C.L., Spry, J.A., Steele, A., Swindle, T.D., ten Kate, I.L., Tosca, N.J., Usui, T., Van Kranendonk, M.J., Wadhwa, M., Weiss, B.P., Werner, S.C., Westall, F., Wheeler, R.M., Zipfel, J. and Zorzano, M.P. (2019) The potential science and engineering value of samples delivered to Earth by Mars sample return. Meteoritics & Planetary Science 54, S3-S152.

Bell, J. F., J. N. Maki, G. L. Mehall, M. A. Ravine, M. A. Caplinger, Z. J. Bailey, S. Brylow, et al. (2020) "The Mars 2020 Perseverance Rover Mast Camera Zoom (Mastcam-Z) Multispectral, Stereoscopic Imaging Investigation." *Space Science Reviews* 217, 24. https://doi.org/10.1007/s11214-020-00755-x.

Bell, J.F., Maki, J.N., Alwmark, S., Ehlmann, B.L., Fagents, S.A., Grotzinger, J.P. Gupta, S., …Yingling, R. (2022) Geological and Meteorological Imaging Results from the Mars 2020 Perseverance Rover in Jezero Crater, *Science Advances* Vol. 8, No. 47, DOI: 10.1126/sciadv.abo4856.

Bhartia, Rohit, Luther W. Beegle, Lauren DeFlores, William Abbey, Joseph Razzell Hollis, Kyle Uckert, Brian Monacelli, et al. (2020) "Perseverance's Scanning Habitable Environments with Raman and Luminescence for Organics and Chemicals (SHERLOC) Investigation." *Space Science Reviews* 217, 58. https://doi.org/10.1007/s11214-021-00812-z.

Bellucci, J.J. Whitehouse, M.J., John, T., Nemchin, A.A., Snape, J.F., Bland, P.A., Benedix, G.X. (2017) Halogen and Cl isotopic systematics in Martian phosphates: Implications for the Cl cycle and surface halogen reservoirs on Mars, *Earth and Planetary Science Letters* 458, 192-202.

Benison, K.C., Bowen, B.B. (2006) Acid saline lake systems give clues about past environments and the search for life on Mars. *Icarus* 183, 225-229.

Benner, S.A., Kim, H.-J., Biondi, E. (2018) Mineral-Organic Interactions in Prebiotic Synthesis. In: Menor-Salván, C. (eds) Prebiotic Chemistry and Chemical Evolution of Nucleic Acids. Nucleic Acids and Molecular Biology, vol 35. Springer, Cham. https://doi.org/10.1007/978-3-319-93584-3_3.

Beyssac O. et al. (submitted) Petrological traverse of an olivine-pyroxene cumulate on the floor of Jezero Crater, Mars: a perspective from SuperCam onboard Perseverance, *J. Geophys. Res.*, this volume.

Black, B.A., Manga, M., Ojha, L., Longpre, M.-A., Karunatillake, S. and Hlinka, L. (2022) The history of water in Martian magmas from thorium maps. *Geophysical Research Letters,* In Press, e2022GL098061.

Blattler, C.L., Claire, M.W., Prave, A.R., Kirsimae, K., Higgins, J.A., Medvedev, P.V., Romashkin, A.E., Rychanchik, D.V., Zerkle, A.L., Paiste, K., Kreitsmann, T., Millar, I.L., Hayles, J.A., Bao, H., Turchyn, A.W., Warke, M.R., Lepland, A. (2018) Two-billion-year-old evaporties capture Earth's great oxidation. *Science* 360, 320-323, DOI: 10.1126/science.aar268.

Blichert-Toft, J., Gleason, J.D., Telouk, P. Albarede, F. (1999) The Lu-Hf isotope geochemistry of shergottites and the evolution of the Martian mantle-crust system. *Earth and Planetary Science Letters* 173, 25-39.

Bogard, D.D., Johnson, P. (1983) Martian gases in an Antarctic meteorite? *Science* 221, 651-654.

Bogard, D.D., Clayton, R.N., Marti, K., Owen, T., Turner, G. (2001) Martian Volatiles: Isotopic Composition, Origin, and Evolution. In: Kallenbach, R., Geiss, J., Hartmann, W.K. (eds) Chronology and Evolution of Mars. Space Sciences Series of ISSI, vol 12. Springer, Dordrecht. https://doi.org/10.1007/978-94-017-1035-0_17.

Borg, L.E., Nyquist, L.E., Taylor, L.A., Wiesmann, H., Shih, C.-Y. (1997) Constraints on Martian differentiation processes from Rb-Sr and Sm-Nd isotopic analyses of the basaltic shergottite QUE 94201. *Geochimica et Cosmochimica Acta* 61 (22), 4915-4931.

Borg, L.E., Nyquist, L.E., Wiesmann, H., Shih, C.-Y., Reese, Y. (2003) The age of Dar al Gani 478 and the differentiation history of the martian meteorites inferred from their radiogenic isotopic systematics. *Geochimica et Comochimica Acta* 67, 3519-3536.

Borg, L.E., Brennecka, G.A., Symes, S.J.K. (2016) Accretion timescale and impact history of Mars deduced from the isotopic systematics of martian meteorites. *Geochimica et Cosmochimica Acta* 175, 150-167.

Bosak, T., Moore, K.R., Gong, J., Grotzinger, J.P. (2021) Searching for biosignatures in sedimentary rocks from early Earth and Mars. *Nature Reviews Earth & Environment* 2(7), 490-506.
Brady, P.V., Walther, J.V. (1989) Controls on silicate dissolution rates in neutral and basic pH solutions at 25°C. *Geochimica et Cosmochimica Acta* 53, 2823-2830.
Breuer, D., Plesa, A.-C., Tosi, N., Grott, M. (2016) Water in the Martian interior—the geodynamical perspective. *Meteoritics & Planetary Science* 51, 1959-1992.
Brown, A. J., Hook, S. J., Baldridge, A. M., Crowley, J. K., Bridges, N. T., Thomson, B. J., et al. (2010) Hydrothermal formation of clay-carbonate alteration assemblages in the Nili Fossae region of Mars. *Earth and Planetary Science Letters* 297(1–2), 174–182. https://doi.org/10.1016/j.epsl.2010.06.018
Brown, A. J., Viviano, C. E., Goudge, T. A. (2020) Olivine-carbonate mineralogy of the Jezero crater region. *J. Geophysical Res. Planets* 125(3), e2019JE006011. https://doi.org/10.1029/2019JE006011.
Brown, A.J., Kah, L., Mandon, L., Wiens, R., Pinet, P., Clavé, E., Le Mouélic, S., Udry, A., Gasda, PJ., Royer, C., Hickman-Lewis, K., Cousin, A., Simon, J.I., Comellas, J, Cloutis, E., Fouchet, T., Fairén, A.G., Connell, S., Flannery, D., Horgan, B., Mayhew, L., Treiman, A., Núñez, J. I., Wogsland, B., Benzerara, K., Amundsen, H.E.F., Quantin-Nataf, C., Hand, K.P., Debaille, V., Essunfeld, A., Beck, P., Tosca, NJ., Madariaga, J.M., Ravanis, E. (submitted) Properties of the Nili Fossae olivine-clay-carbonate lithology: orbital and in situ at Séítah, *J. Geophysical Res. Planets*, this volume.
Calef III, F.J., Alwmark, S., Amundsen, H.E.F., Bechtold, A., Bell, J., Quantin, C., Dypvik, H, Hamran, S.-E., Schmitz, N., Simon, J.I., Stack, K.M. (2021) Visiting a fresh crater in Jezero with the Mars 2020 Perseverance Rover, GSA, Portland, Oregon, USA. Doi: 10.1130/abs/2021AM-370948.
Carr, M.H., Head III, J.W. (2010) Geologic history of Mars. *Earth and Planetary Science Letters* 294, 185-203.
Clavé, E., Benzerara, K., Beck, P., Meslin ,P.-Y., Beyssac, O., Forni, O., Cousin, A., Bosak, T., Bousquet, B., Castro, K., Clegg, S., Cloutis, E., Gasnault, O., Lopez-Reyes, G., Madriaga, J.M., Mandon, L., Maurice, S., Le Mouélic, S., Ollila, A., Pilorget, C., Pinet, P., Quantin-Nataf, C., Schröder, S., Wiens, R.C. and the SuperCam Team (2022) Carbonate detection

with SuperCam in the Jezero Crater, Mars, In Proceedings of the 53rd Lunar and Planetary Science Conference (LPSC). Lunar and Planetary Institute, United States of America.

Clenet, H., Pinet, P., Ceuleneer, G., Daydou, Y., Heuripeau, F., Rosemberg, C., Bibring, J.-P., Bellucci, G., Altieri, F., Gondet, B. A. (2013) A systematic mapping procedure based on the Modified Gaussian Model to characterize magmatic units from olivine/pyroxenes mixtures: Application to the Syrtis Major volcanic shield on Mars, https://doi.org/10.1002/jgre.20112.

Corpolongo, A. et al. (submitted) SHERLOC Raman mineral detections of the Mars 2020 Crater Floor Campaign, *J. Geophys. Res.*, this volume.

Crumpler, L. S., Horgan, B., Simon, J. I., Stack, K., Gilles, D., Wiens, R., Brown, A., Russel, P., Amundson, H., Bell III, J., Calef, F., Cohen, B., Flannery, D., Hand, K., Maki, J., Schmidt, M., Golombek, M., Williams, N. (submitted) In situ Geologic Context Mapping (GXM) Transect on the Jezero Crater Floor from Mars 2020/Perseverance Rover Observations, *J. Geophysical Res. Planets,* this volume.

Day, J.M.D., Brandon, A.D. and Walker, R.J. (2016) Highly Siderophile Elements in Earth, Mars, the Moon, and Asteroids. *Reviews in Mineralogy and Geochemistry* 81, 161-238.

Dauphas, N., Pourmand, A. (2011) Hf-W-Th evidence for rapid growth of Mars and its status as a planetary embryo. *Nature* 473, 489-492.

Debaille, V., Brandon, A.D., Yin, Q.Z., Jacobsen, B. (2007) Coupled ^{142Nd}-^{143}Nd evidence for a protracted magma ocean in Mars. *Nature* 450, 525-528.

Debaille, V., O'Nell, C., Brandon, A.D., Haenecour, P. Yin, Q.-Y., Mattielli, N., Trieman, A.H. (2013) Stagnant-lid tectonics in early Earth revealed by ^{142}Nd variations in late Archean rocks. *Earth and Planetary Science Letters* 373, 83-92.

Dreibus, G., Wanke, H. (1985) Mars, a volatile-rich planet. *Meteoritics* 20 (2), 365-381.

Ehlmann, B.L., Mustard, J.F., Fassett, C.I., Schon, S.C., Head III, J.W., Des Marais, D.J., Grant, J.A., Murchie, S.L. (2008) Clay minerals in delta deposits and organic preservation potential on Mars. Nature Geoscience 1, 355-358.

Eigenbrode, J.L., Summons, R.E., Steele, A., Freissinet, C., Millan, M., Navarro-Gonazlez, R., Sutter, B., McAdam, A.C., Franz, H.B., Glavin, D.P., Archer, P.D., Mahaffy, P.R., Conrad, P.G., Hurowitz, J.A., Grotzinger, J.P., Gupta, S., Ming, D.W., Sumner, D.Y., Szopa, C., Malespin, C., Buch, A., Coll, P. (2018) Organic matter preserved in 3-billion-year-old mudstones at Gale crater, Mars. *Science* 360, 1096-1101, DOI: 10.1126/science.aas918.

Elkins-Tanton, L.T. (2008) Linked magma ocean solidification and atmospheric growth for Earth and Mars. *Earth and Planetary Science Letters* 271, 181-191.

Etiope, G., Whiticar, M.J. (2019) Abiotic methane in continental ultramafic rock systems: Towards a genetic model. *Applied Geochemistry* 102, 139-152.

Fassett, C.I., Head III, JW. (2008) The timing of martian valley network activity: Constraints from buffered crater counting. *Icarus* 195 (1) 61-89.

Farley, K.A., Malespin, C., Mahaffy, P., Grotzinger, J.P. Vasconcelos, P.M., et al. and the MSL Science Team (2014) In situ radiometric and exposure age dating of the martian surface. *Science* 343, DOI: 10.1126/science.1247166

Farley, K. A., Williford, K. H., Stack, K. M., Bhartia, R.,Chen, A. dela Torre, M., Hand, K., Goreva, Y., Herd, C. D. K., Hueso, R., Liu, Y., Maki, J. N., Martinez, G., Moeller, R.C., Nelessen, A., Newman, C. E., Nunes, D., Ponce, A., Spanovich, N., Willis, P.A., Beegle, L. W., Bell, J.F., Brown, A.J., Hamran, S.-E., Hurowitz, J.A., Maurice, S. Paige, D.A., Rodriguez-Manfredi, J.A., Schulte, M., Wiens, R.C. (2020) Mars 2020 Mission Overview, *Space Science Reviews*, 216 (8) doi.org/10.1007/s11214-020-00762-y

Farley K. A., Stack, K. M., Shuster, D. L., Horgan, B. H. N., Hurowitz, J. A., Tarnas, J. I. Simon, ... & Zorzano, M. P., (2022) Aqueously altered igneous rocks on the floor of Jezero crater, Mars, *Science* 377, DOI: 10.1126/science.abo2196.

Filiberto, J., Gross, J. and McCubbin, F.M. (2016) Constraints on the water, chlorine, and fluorine content of the Martian mantle. *Meteoritics & Planetary Science* 51, 2023-2035.

Flynn, G.J. (1996). The Delivery of Organic Matter from Asteroids and Comets to the Early Surface of Mars. In: Rickman, H., Valtonen, M.J. (eds) Worlds in Interaction: Small Bodies and Planets of the Solar System. Springer, Dordrecht. https://doi.org/10.1007/978-94-009-0209-1_58.

Freissinet, C., Glavin, D. P., Mahaffy, P. R., Miller, K. E., Eigenbrode, J. L., Summons, R. E., Brunner, A. E., Buch, A., Szopa, C., Archer Jr., P. D., Franz, H. B., Atreya, S. K., Brinckerhoff, W. B., Cabane, M., Coll, P., Conrad, P. G., Des Marais, D. J., Dworkin, J. P., Fairén, A. G., François, P., Grotzinger, J. P., Kashyap, S., ten Kate, I. L., Leshin, L. A., Malespin, C. A., Martin, M. G., Martin-Torres, F. J., McAdam, A. C., Ming, D. W., Navarro-González, R., Pavlov, A. A., Prats, B. D., Squyres, S. W., Steele, A., Stern, J. C., Sumner, D.

Y., Sutter, B., Zorzano, M.-P., and the MSL Science Team (2015) *J. Geophysical. Res. Planets* 120, 595-514.

Garczynski, B.J., Bell III, J.F., Horgan, B.H.N., Johnson, J.R., Rice, M.S., Vaughan, A., Núñez, J.I., Herd, C.D.K. (2022) Perseverance and the purple coating: a Mastcam-Z multispectral story, In Proceedings of the 53rd Lunar and Planetary Science Conference (LPSC). Lunar and Planetary Institute, United States of America.

Gattacceca, J., Rochette, P. Scorzelli, R.B., Munayco, P., Agee, C., Quesnel, Y., Cournede, C., Geissman, J. (2014) Martian meteorites and Martian magnetic anomalies: A new perspective from NWA 7034. *Geophysical Research Letters* 41, 4,859-4,864.

Goderis, S., Brandon, A.D., Mayer, B. and Humayun, M. (2016) Ancient impactor components preserved and reworked in martian regolith breccia Northwest Africa 7034. *Geochimica et Cosmochimica Acta* 191, 203-215.

Goudge, T.A., Head, J.W., Mustard, J.F., Fassett, C.I. (2012) An analysis of open-basin lake deposits on Mars: Evidence for the nature of associated lacustrine deposits and post-lacustrine modification processes, *Icarus* 219 (1), 211-229.

Goudge, T.A., Mustard, J.F., Head, J.W., Fassett, C.I., Wiseman, S.M. (2015) Assessing the mineralogy of the watershed and fan deposits of the Jezero crater paleolake system, Mars, *J. Geophysical Res. Planets*, 120, 775–808, doi:10.1002/2014JE004782.

Gross, J., Filiberto, J. and Bell, A.S. (2013) Water in the martian interior: Evidence for terrestrial MORB mantle-like volatile contents from hydroxyl-rich apatite in olivine–phyric shergottite NWA 6234. *Earth and Planetary Science Letters* 369–370, 120-128.

Haltigin, T.H., Hauber, E., Kminek, G., Meyer, M.A., Agee, C.B., Busemann, H., Carrier, B.L., Glavin, D.P., Hays, L.E., Marty, B., Pratt, L.M., Udry, A., Zorzano, M.-P., Beaty, D.W., Cavalazzi, B., Cockell, C.S., Debaille, V., Grady, M.M., Hutzler, A., McCubbin, F.M., Regberg, A.B., Smith, A.L., Smith, C.L., Summons, R.E., Swindle, T.D., Tait, K.T., Tosca, N.J., Usui, T., Velbel, M.A., Wadhwa, M. and Westall, F. (2022) Rationale and Proposed Design for a Mars Sample Return (MSR) Science Program. *Astrobiology* 22, S-27-S-56.

Hamran, Svein-Erik, David A. Paige, Hans E. F. Amundsen, Tor Berger, Sverre Brovoll, Lynn Carter, Leif Damsgård, et al. (2020) Radar Imager for Mars' Subsurface Experiment—RIMFAX. *Space Science Reviews* 216, 128. https://doi.org/10.1007/s11214-020-00740-4.

Hamran, S.-E., Paige, D.A., Allwood, A., Amundsen, H.E.F., Berger, T., Provoll, S., Carter, L., Casademont, T.M., Damsgard, L., Dypvik, H., Eide, S., Fairen, A.G., Ghent, R., Kohler, J., Mellon, M.T., Nunes, D.C., Plettemeier, D., Russell, P., Siegler, M., Oyan, M.J. (2022) Ground penetrating radar observations on subsurface structures in the floor of Jezero crater, Mars. *Science Advances* 8, DOI: 10.1126/sciadv.abp8564.

Harper, C.L. Jr., Nyquist, L.E., Bansal, B., Wiesmann, H., Shih, C.-Y. (1995) Rapid accretion and early differentiation of Mars indicated by $^{142}Nd/^{144}Nd$ in SNC meteorites, *Science* 267 (5195), 213-217.

Hauri, E.H., Saal, A.E., Rutherford, M.J. and Van Orman, J.A. (2015) Water in the Moon's interior: Truth and consequences. *Earth and Planetary Science Letters* 409, 252-264.

Hays, L., Graham, H.V., Des Marais, D. J., Hausrath, E. M., Horgan, B., McCollom, T.M., Parenteau, M. N., Potter-McIntyre, S. L., Williams, A. J., Lynch, K. L. (2017) *Astrobiology*, doi.org/10.1089/ast.2016.1627

Herd, C.D.K., Walton, E.L., Agee, C.B., Muttik, N., Ziegler, K., Shearer, C.K., Bell, A.S., Santos, A.R., Burger, P.V., Simon, J.I., Tappa, M.J., McCubbin, F.M., Gattacceca, J., Lagroix, F., Sanborn, M.E., Yin, Q.-Z., Cassata, W.S., Borg, L.E., Lindvall, R.E., Kruijer, T.S., Brennecka, G.A., Kleine, T., Nishiizumi, K. and Caffee, M.W. (2017) The Northwest Africa 8159 martian meteorite: Expanding the martian sample suite to the early Amazonian. *Geochimica et Cosmochimica Acta* 218, 1-26.

Horgan, B.H.N., Anderson, R.B., Dromart, G., Amador, E.S., Rice, M.S. (2020) The mineral diversity of Jezero crater: Evidence for possible lacustrine carbonates on Mars, *Icarus* 339 (15), 113526.

Horgan B., Rice M., Garczynski B., Johnson J., StackMorgan, K., Vaughan A., Wogsland B., Bell III J.F., Crumpler L., Ehlmann B., Holm-Alwmark S., Farley K., Fagents S., Núñez J., Paar G., Ravanis E., Shuster D., Simon J.I., Udry A., Wadhwa M., Wiens R. (2022) Mineralogy, Morphology, and geochronological significance of the Máaz formation and the Jezero crater floor, In Proceedings of the 53rd Lunar and Planetary Science Conference (LPSC). Lunar and Planetary Institute, United States of America.

Humayun, M., Nemchin, A., Zanda, B., Hewins, R.H., Grange, M., Kennedy, A., Lorand, J.-P., Gopel, C., Fieni, C., Pont, S., Deldicque, D. (2017) Origin and age of the earliest Martian crust from meteorite NWA 7533. *Nature* 503, 513-516.

iMOST (2018), The Potential Science and Engineering Value of Samples Delivered to Earth by Mars Sample Return, (co-chairs D. W. Beaty, M. M. Grady, H. Y. McSween, E. Sefton-Nash; documentarian B.L. Carrier; plus 66 co-authors), 186 p. white paper. Posted August, 2018 by MEPAG at https://mepag.jpl.nasa.gov/reports.cfm.

Jakosky B, Amato M, Atreya S, Marais, D.D., Mahaffy, P., Mumma, M., Tolbert, M., Toon, B., Webster, C., Zurek, R. (2021) Scientific value of returning an atmospheric sample from Mars. Bulletin of the AAS 53(4). Whitepaper #159 submitted to the Planetary Science and Astrobiology Decadal Survey 2023-2032. Topics: atmospheric/exospheric evolution; life and prebiotic organics.

Jaramillo, E.A., Royle, S.H., Claire, M.W., Kounaves, S.P. and Sephton, M.A. (2019) Indigenous Organic-Oxidized Fluid Interactions in the Tissint Mars Meteorite. *Geophysical Research Letters* 46, 3090-3098.

John, T., Gussone, N., Padladchikov, Y.Y., Bebout, G.E., Dohmne, R., Halama, R. , Klemd, R., Magna, T., Seitz, H.-M. (2012) Volcanic arcs fed by rapid pulsed fluid flow through subducting slabs, *Nature GeoScience* 5, 489-492. https://doi.org/10.1038/ngeo1482

Johnson, C.M, Beard, B.L., & Francis Albarède (2004) Geochemistry of Non-traditional stable isotopes, in Reviews in Mineralogy and Geochemistry 55 (1), 1–24. https://doi.org/10.2138/gsrmg.55.1.1

Jonckbloedt, R.C.L. (1998) Olivine dissolution in sulphuric acid at elevated temperatures: implications for the olivine process, an alternative waste acid neutralizing process. *Journal of Geochemical Exploration* 62, 337-346.

Kang, J. T., Ionov, D. A., Liu, F., Zhang, C. L., Golovin, A. V., Qin, L. P., Zhang, Z.-F., Huang, F. (2017). Calcium isotopic fractionation in mantle peridotites by melting and metasomatism and Ca isotope composition of the bulk silicate Earth, *Earth and Planetary Science Letters* 474, 128– 137. https://doi.org/10.1016/j.epsl.2017.05.035

Kizovski, T.V., Schmidt, M.E., Liu, Y., Clark, B.C., Tice, M., Herd, C.D.K., Hurowitz, J., VanBommel, S., Henley, T., Allwood, A. (2022) Minor minerals analyzed by PIXL—a major part of igneous rock petrogenesis at Jezero Crater, In Proceedings of the 53rd Lunar and Planetary Science Conference (LPSC). Lunar and Planetary Institute, United States of America.

Klein, F., Grozeva, N.G., Seewald, J.S., McCollom, T.M., Humphris, S.E., Moskowitz, B., Berquó. T.S., Kahl, W.-A. (2015) Experimental constraints on fluid-rock reactions during incipient serpentinization of harzburgite. *American Mineralogist* 100 (4), 991-1002.

Klein, F., Grozeva, N.G., Seewald, J.S. (2019) Abiotic methane synthesis and serpentinization in olivine-hosted fluid inclusions. *PNAS* 116 (36) 17,666-17,672.

Koike, M., Nakada, R., Kajitani, I., Usui, T., Tamenori, Y., Sugahara, H. and Kobayashi, A. (2020) In-situ preservation of nitrogen-bearing organics in Noachian Martian carbonates. *Nature Communications* 11, 1988.

Kminek, G., Benardini, J.N., Brenker, F.E., Brooks, T., Burton, A.S., Dhaniyala, S., Dworkin, J.P., Fortman, J.L., Glamoclija, M., Grady, M.M., Graham, H.V., Haruyama, J., Kieft, T.L., Koopmans, M., McCubbin, F.M., Meyer, M.A., Mustin, C., Onstott, T.C., Pearce, N., Pratt, L.M., Sephton, M.A., Siljeström, S., Sugahara, H., Suzuki, S., Suzuki, Y., van Zuilen, M. and Viso, M. (2022) COSPAR Sample Safety Assessment Framework (SSAF). *Astrobiology* 22, S-186-S-216.

Lagain, A., Benedix, G.K., Servis, K., Baratoux, D., Doucet, L.S., Rajsic, A., Devillepoix, H.A.R., Bland, P.A., Towner, M.C., Sansom, E.K., Miljkovic, K. (2021) The Tharsis mantle source of depleted shergottites revealed by 90 million impact craters, *Nature communications* 12: 6352.

Lammer, H., Chassefière, E. Karatekin, Ö., Morschhauser, A., Niles, P.B., Mousis, O., Odert, P., Möstl, U.V., Breuer, D., Dehant, V., Grott, M., Gröller, H., Hauber, E., Binh San Pham, L. (2013) Outgassing History and Escape of the Martian Atmosphere and Water Inventory, *Space Science Reviews* 174, 113-154.

Lapen, T.J., Righter, M., Brandon, A.D., Debaille, V., Beard, B.L., Shafer, J.T., Peslier, A.H. (2010) A younger age for ALH84001 and its geochemical link to Shergottite sources in Mars. *Science* 328, 347-351.

Lapen, T.J., Righter, M., Andreasen, R., Irving, A.J., Satkoski, A.M., Beard, B.L., Nishizumi, K., Jull, A.J.T., Caffee, W. (2017) Two billion years of magmatism recorded from a single Mars meteorite ejection site. *Science Advances* 3 (2), DOI: 10.1126/sciadv.1600922.

Lasaga, A., 1998. Kinetic Theory in the Earth Sciences. Princeton University Press, Princeton, NJ.

Liu, Y., Tice, M. M., Schmidt, M. E., Treiman, A. H., Kizovski, T. V., Hurowitz, J. A., ...

1183 & Zorzano, M. P. (2022) An olivine cumulate outcrop on the floor of Jezero crater, Mars, *Science* 377, 1513-1519, DOI: 10.1126/science.abo27.

Madigan, M.T., Bender, K.S., Buckley, D.H., Sattley, W.M., Stahl, D.A., Brock, T.D. (2022) Brock biology of microorganisms, 16th edition, New York (N.Y.) : Pearson ; Harlow (United Kingdom) : Pearson Education limited. Copyright 2022, pp. 1124.

Madsen, M.B., Goetz, W., Bertelsen, P., Binau, C. S., Folkmann, F., Gunnlaugsson, H. P., í Hjøllum, J., Hviid, S. F., Jensen, J., Kinch, K. M., Leer, K., Madsen, D. E., Merrison, J., Olsen, M., Arneson, H. M., Bell III, J. F., Gellert, R., Herkenhoff, K. E., Johnson, J. R., Johnson, M. J., Klingelhöfer, G., McCartney, E., Ming, D. W., Morris, R. V., Proton, J. B., Rodionov, D., Sims, M., Squyres, S. W., Wdowiak, T., Yen, A. S. (2009) Overview of the magnetic properties experiments on the Mars Exploration Rovers. *J. Geophysical Res. Planets* 114, https://doi.org/10.1029/2008JE003098.

Maki, J. N., D. Gruel, C. McKinney, M. A. Ravine, M. Morales, D. Lee, R. Willson, et al. (2020) "The Mars 2020 Engineering Cameras and Microphone on the Perseverance Rover: A Next-Generation Imaging System for Mars Exploration." *Space Science Reviews* 216, 137. https://doi.org/10.1007/s11214-020-00765-9.

Mandon, L., Quantin-Nataf, C., Thollot, P., Mangold, N., Lozac'h, L., Dromart, G., Beck, P., Dehouck, E., Breton, S., Millot, C., Volat, M. (2020) Refining the age, emplacement and alteration scenarios of the olivine-rich unit in the Nili Fossae region, Mars, *Icarus* 336, 113436.

Mandon, L., Quantin-Nataf, C., Royer, C., Beck, P., Fouchet, T., Johnson, J.R., Forni, O., Montmessin, F., Pilorget, C., Poulet, F., Le Mouélic, S., Dehouck, E., Beyssac, O., Brown, A., Tarnas, J., Maurice, S., Wiens, R.C. and the SuperCam team (2022) Infrared reflectance of rocks and regolith at Jezero crater one year of SuperCam observations, In Proceedings of the 53rd Lunar and Planetary Science Conference (LPSC). Lunar and Planetary Institute, United States of America.

Mangold N., Gupta S., Gasnault O., Dromart G., Tarnas J. D., Sholes S. F., Horgan B., Quantin-Nataf C., Brown A. J., Le Mouélic S., Yingst R. A., Bell J. F., Beyssac O., Bosak T., Calef F., Ehlmann B. L., Farley K. A., Grotzinger J. P.,-Lewis K., Holm-Alwmark S., Kah L. C., Martinez-Frias J., McLennan S. M., Maurice S., Núñez J. I., Ollila A. M., Pilleri P., Rice J. W., Rice M., Simon J. I., Shuster D. L., Stack K. M., Sun V. Z., Treiman A. H., Weiss B. P., Wiens R. C., Williams A. J., Williams N. R., Williford K. H. (2021) Perseverance rover reveals an ancient delta-lake system and flood deposits at Jezero crater, Mars, *Science*, 10.1126/science.abl4051

Maurice, S., R. C. Wiens, P. Bernardi, P. Caïs, S. Robinson, T. Nelson, O. Gasnault, et al. (2020) "The SuperCam Instrument Suite on the Mars 2020 Rover: Science Objectives and Mast-Unit Description." *Space Science Reviews* 217, 47. https://doi.org/10.1007/s11214-021-00807-w.

McCubbin, F.M., Nekvasil, H., Harrington, A.D., Elardo, S.M., Lindsley, D.H. (2008) Compositional diversity and stratification of the Martian crust: Inferences from crystallization experiments on the picrobasalt Humphrey from Gusev Crater, Mars. *J. Geophysical Res. Planets* 113, https://doi.org/10.1029/2008JE003165.

McCubbin, F.M., Smirnov, A., Nekvasil, H., Wang, J., Hauri, E. and Lindsley, D.H. (2010) Hydrous magmatism on Mars: A source of water for the surface and subsurface during the Amazonian. *Earth and Planetary Science Letters* 292, 132-138.

McCubbin, F.M., Hauri, E.H., Elardo, S.M., Vander Kaaden, K.E., Wang, J. and Shearer, C.K. (2012) Hydrous melting of the martian mantle produced both depleted and enriched shergottites. *Geology* 40, 683-686.

McCubbin, F.M., Boyce, J.W., Srinivasan, P., Santos, A.R., Elardo, S.M., Filiberto, J., Steele, A. and Shearer, C.K. (2016) Heterogeneous distribution of H_2O in the martian interior: Implications for the abundance of H_2O in depleted and enriched mantle sources. *Meteoritics & Planetary Science* 51, 2036-2060.

McCubbin, F.M., Lewis, J.A., Barnes, J.J., Elardo, S.M. and Boyce, J.W. (2021) The abundances of F, Cl, and H_2O in eucrites: Implications for the origin of volatile depletion in the asteroid 4 Vesta. *Geochimica et Cosmochimica Acta* 314, 270-293.

McKay, D.S., Gibson, E.K., Thomas-Keprta, K.L., Vali, H., Romanek, C., Clemett, S.J., Chillier, X.F., Maechling, C.R., Zare, R.N. (1996) *Science* 273, 924-930.

McMahon, S., Bosak, T., Grotzinger, J. P.,Milliken, R. E., Summons, R. E., Daye, M., Newman, S.A., Fraemann, A., Williford, K.H., Briggs, D.E.G. (2018). A field guide to finding fossils on Mars, *J. Geophysical Res. Planets*,123, 1012–1040 https://doi.org/10.1029/2017JE005478

McSween, H.Y., Ruff, S.W., Morris, R.V., Bell, J.F., Herkenhoff, K.E., Gellert, R., Stockstill, K.R., Tornabene, L.L., Squyres, S.W., Crisp, J.A., Christensen, P.R., McCoy, T.J., Mittlefehldt, D.W. and Schmidt, M. (2006) Alkaline volcanic rocks from the Columbia Hills, Gusev crater, Mars. *J. Geophysical Res. Planets* 111, 15.

Meyer, M.A., Kminek, G., Beaty, D.W., Carrier, B.L., Haltigin, T.H., Hays, L.E., Agee, C.B., Busemann, H., Cavalazzi, B., Cockell, C.S., Debaille, V., Glavin, D.P., Grady, M.M., Hauber, E., Hutzler, A., Marty, B., McCubbin, F.M., Pratt, L.M., Regberg, A.B., Smith, A.L., Smith, C.L., Summons, R.E., Swindle, T.D., Tait, K.T., Tosca, N.J., Udry, A., Usui, T., Velbel, M.A., Wadhwa, M., Westall, F. and Zorzano, M.-P. (2022) Final Report of the Mars Sample Return Science Planning Group 2 (MSPG2). *Astrobiology* 22, S-5-S-26.

Meslin, P.-Y., Forni, O. , Beck, P. , Cousin, A. , Beyssac, O. , Lopez-Reyes, G. , Benzerara, K., Ollila, A., Mandon, L., Wiens, R.C., Clegg, S., Montagnac, G., Clavé, E., Manrique, J.-A., Chide, B., Maurice, S., Gasnault, O., Lasue, J., Quantin-Nataf, C., Dehouck, E., Sharma, S.K., Arana, G., Madariaga, J.M., Castro, K., Schröder, S., Mangold, N., Poulet, F., Johnson, J., Le Mouélic, S., Zorzano, M.-P., and the SuperCam Team (2022) Evidence for perchlorate and sulfate salts in Jezero crater, Mars, from SuperCam observations, In Proceedings of the 53rd Lunar and Planetary Science Conference (LPSC). Lunar and Planetary Institute, United States of America.

Millan, M., Teinturier, S., Malespin, C. A., Bonnet, J. Y., Buch, A., Dworkin, J. P., Eigenbrode, J. L., Freissinet, C., Glavin, D. P., Navarro-González, R., Srivastava, A., Stern, J. C., Sutter, B., Szopa, C., Williams, A. J., Williams, R. H., Wong, G. M., Johnson S. S., Mahaffy P. R. (2022) Organic molecules revealed in Mars's Bagnold Dunes by Curiosity's derivatization experiment. *Nature Astronomy* 6, 129-140.

Mills, R.D., Simon, J.I., DePaolo, D.J. (2018) Calcium and neodymium radiogenic isotopes of igneous rocks: Tracing crustal contributions in felsic magmas related to super-eruptions and continental rifting, *Earth and Planetary Science Letters* 495, 242-250.

Moeller, R.C., Jandura, L., Rosette, K., Robinson, M., Samuels, J., Silverman, M., Brown, K., Duffy, E., Yazzie, A., Jens, E., Brockie, I., White, L., Goreva, Y., Zorn, T., Okon, A., Lin, J., Frost, M., Collins, C., Williams, J.B., Steltzner, A., Chen, F., Biesiadecki (2021) The Sampling and Caching Subsystem (SCS) for the Scientific Exploration of Jezero Crater by the Mars 2020 Perseverance Rover. *Space Sci Rev* 217, 5. https://doi.org/10.1007/s11214-020-00783-7

Moore, W.B., Simon, J.I., Webb, A.A.G. (2017) Heat-pipe planets. *Earth and Planetary Science Letters* 474, 13-19.

Moriwaki, R., Usui, T., Simon, J.I., Jones, J.H., Yokoyama, T., Tobita, M. (2017) Coupled Pb isotopic and trace element systematics of the Tissint meteorite: Geochemical signatures of the depleted shergottite source mantle. *Earth and Planetary Science Letters* 474, 180-189.

Moriwaki, R., Usui, T., Tobita, M., Yokoyama, T. (2020) Geochemically heterogeneous Martian mantle inferred from Pb isotope systematics of depleted shergottites. *Geochimica et Cosmochimica Acta* 274, 157-171.

Morris, R.V., Klingelhofer, G., Schroder, C., Rodionov, D.S., Yen, A., Ming, D.W., de Souza, P.A. Jr., Wdowiak, T., Fleischer, I., Gellert, R., Bernhardt, B., Bonnes, U., Cohen, B.A., Evlanov, E.N., Foh, J., Gutlich, P., Kenkeleit, E., McCoy, T., Mittlefehldt, D.W., Renz, F., Schmidt, M.E., Zubkov, B., Squyres, W., Arvidson, R.E. (2006) Mössbauer mineralogy of rock, soil, and dust at Meridiani Planum, Mars: Opportunity's journey across sulfate-rich outcrop, basaltic sand and dust, and hematite lag deposits. *J. Geophysical Res. Planets* 111, https://doi.org/10.1029/2006JE002791.

Mosenfelder, J.L. Mosenfelder, Rossman, G.R., Johnson, E.A. (2015) Hydrous species in feldspars: A reassessment based on FTIR and SIMS. *American Mineralogist* 100, 1209-1221.

Murphy, M.A.E., Beegle, L.W., Bhartia, R., DeFlores, L., Abbey, W., Razzell Hollis, J., Asher, S., Berger, E., Bykov, S., Burton, A., Fox, A, Fries, M., Conrad, P., Clegg, S., Edgett, K. S., Ehlmann, B., Kah, L., Lee, C., Minitti, M., Roppel, R., Sharma, S., Siljeström, S., Smith, C., Sobron, P., Steele, A., Wiens, R., Williford, K., Wogsland, B., Kennedy, M. R., Yingst, R. A. (2022) The first 300 sols of the SHERLOC investigation on the Mars 2020 rover, In Proceedings of the 53rd Lunar and Planetary Science Conference (LPSC). Lunar and Planetary Institute, United States of America.

Oelkers, E.H., 2001. An experimental study of forsterite dissolution rates as a function of temperature and aqueous Mg and Si concentrations. *Chemical Geology* 175, 485-494.

Olsen, A.A., Hausrath, E.M., Rimstidt, D. (2015) Forsterite dissolution rates in Mg-sulfate-rich Mars-analog brines and implications of the aqueous history of Mars. *J. Geophysical. Res. Planets* 120, 388-400.

Paniello, R., Day, J.M.D., Moynier, F. (2012) Zinc isotopic evidence for the origin of the Moon, *Nature* 490, 376-379.

Peslier, A.H. (2010) A review of water contents of nominally anhydrous natural minerals in the mantles of Earth, Mars, and the Moon, *Journal of Volcanology and Geothermal Research* 197, 239-258.

Peters, TJ, Simon, JI, Jones, JH, Usui, T, Moriwaki, R, Economos, RC, Schmitt, AK, McKeegan, KD (2015) Tracking the martian mantle signature in olivine-host melt inclusions of basaltic shergottites Yamato 980459 and Tissint, *Earth and Planetary Science Letters* 418, 91-102.

Pokrovsky, O.S., Schott, J., 2000. Kinetics and mechanism of forsterite dissolution at 25°C and pH from 1 to 12. *Geochimica et Cosmochimica Acta* 64, 3313-3325.

Pinet, P. C., and Chevrel , S.D. 1990. Spectral identification of geological units on the surface of Mars related to the presence of silicates from Earth-based near-infrared telescopic charge-coupled device imaging, *J. Geophysical Res. Plants* 95, 14,435-14,446. https://doi.org/10.1029/JB095iB09p14435.

Pritchett, B.N., Madden, M.E.E., Madden, A.S. (2012) Jarosite dissolution rates and maximum lifetimes in high salinity brines: Implications for Earth and Mars. *Earth and Planetary Science Letters* 357-358, 327-336.

Quantin-Nataf, C., Holm-Alwmark, S., Lasue, J., Calef, F. J., Shuster, D., Kinch, K. M., Stack, K. M., Sun, V., Williams, N. R., Dehouck, E., Brown, A. (2021) The Complex Exhumation History of Jezero Crater Floor Unit, 52nd Lunar and Planetary Science Conference, held virtually, 15-19 March, 2021. LPI Contribution No. 2548.

Reeves, E.P., Fiebig, J. (2020) Abiotic synthesis of methane and organic compounds in Earth's Lithosphere. *Elements* 16, 25-31.

Rice, M.S., Johnson, J.R., Million, C.C., St. Clair, M., Horgan, B.N., Vaughan, A., Núñez, J.I., Garczynski, B., Curtis, S., Kinch, K.M., Hayes, A., Bell, J.F. (2022) Summary of Mastcam-Z visible to near infrared (VNIR) multispectral observations from Perseverance's Mission in Jezero crater, Mars, In Proceedings of the 53rd Lunar and Planetary Science Conference (LPSC). Lunar and Planetary Institute, United States of America.

Robie, R.A., Hemingway, B.S., Fisher, J.R., 1979. Thermodynamic properties of minerals and related substances at 298.15°K and 1 Bar (105 Pascals) pressure and at higher temperatures. *United States Geological Survey Bulletin* 1452, 456.

Rosso, J.J., Rimstidt, J.D., 2000. A high resolution study of forsterite dissolution rates. *Geochimica et Cosmochimica Acta* 64, 797-811.

Royer, C., Fouchet, T., Montmessin, F., Poulet, F., Forni, O., Johnson, J. R., Gasnault, O., Mandon, L., QuantinNataf, C., Beck, P., Ollila, A. M., Pilorget, C., Bernardi, P., Reess, J.-M., Newell, R. T., Maurice, S., Wiens, R. C. and the SuperCam team (2022) The detection of spectral signatures with IRS/SuperCam, Perseverance rover: instrument performance, In Proceedings of the 53rd Lunar and Planetary Science Conference (LPSC). Lunar and Planetary Institute, United States of America.

Rubin, A. E., Warren, P. H., Greenwood, J. P., Verish, R. S., Leshin, L. A., Hervig, R. L., et al. (2000). Los Angeles: The most differentiated basaltic martian meteorite. *Geology* 28(11), 1011–1014.

Saal, A.E., Hauri, E.H., Langmuir, C.H. and Perfit, M.R. (2002) Vapour undersaturation in primitive mid-ocean-ridge basalt and the volatile content of Earth's upper mantle. *Nature* 419, 451-455.

Santos, A. R., Agee, C. B., McCubbin, F. M., Shearer, C. K., Burger, P. V., Tart.se, R., & Anand, M. (2015). Petrology of igneous clasts in Northwest Africa 7034: Implications for the petrologic diversity of the martian crust. *Geochimica et Cosmochimica Acta* 157, 56–85.

Sautter, V., Toplis, M.J., Beck, P., Mangold, N., Wiens, R., Pinet, P., Cousin, A., Maurice, S., LeDeit, L., Hewins, R., Gasnault, O., Quantin, C., Forni, O., Newsom, H., Meslin, P.-Y., Wray, J., Bridges, N., Payré, V., Rapin, W. and Le Mouélic, S. (2016) Magmatic complexity on early Mars as seen through a combination of orbital, in-situ and meteorite data. *Lithos* 254–255, 36-52.

Schon, S.C., Head, J.W., Fassett, C.I. (2012) An overfilled lacustrine system and progradational delta in Jezero crater, Mars: Implications for Noachian climate, *Planetary and Space Science,* 67 (1) 28-45.

Scheller, E.L., Razzell Hollis, J., Cardarelli, E.L., Steele, A., Beegle, L.W., Bhartia, R., Conrad, P., Uckert, K., Sharma, S., Ehlmann, B.L., Abbey, W.J., Asher, S.A., Benison, K.C., Berger, E.L., Beyssac, O., Bleefeld, B.L., Bosak, T., Brown, A.J., Burton, A.S., Bykov, S.V., Cloutis, E., Fairén, A.G., DeFlores, L., Farley, K.A., Fey, D.M., Fornaro, T., Fox, A.C., Fries, M., Hickman-Lewis, K., Hug, W.F., Huggett, J.E., Imbeah, S., Jakubek, R.S., Kah, L.C., Kelemen, P., Kennedy, M.R., Kizovski, T., Lee, C., Liu, Y., Mandon, L., McCubbin, F.M., Moore, K.R., Nixon, B.E., Núñez, J.I., Rodriguez Sanchez-Vahamonde, C., Roppel, R.D., Schulte, M., Sephton, M.A., Sharma, S.K., Siljeström, S., Shkolyar, S., Shuster, D.L., Simon, J.I., Smith, R.J., Stack, K.M., Steadman, K., Weiss, B.P., Werynski, A., Williams, A.J., Wiens, R.C., Williford, K.H., Winchell, K., Wogsland, B., Yanchilina, A., Yingling, R., Zorzano, M.-P. (2022) Aqueous alteration processes and implications for organic geochemistry in Jezero crater, Mars, *Science.*

Schmidt, M. E., Allwood, A., Christian, J., Clark, B., Flannery, David, Hennecke, J., Herd, C. D. K., Hurowitz, J. A., Kizovski, Tanya V., Liu, Y., McLennan, S. M., Nachon, Marion, Pedersen, D. A. K., Shuster, D. L., Simon, J. I., Tice, M., Tosca, Nicholas, Treiman, A. H., Udry, Arya, Van Bommel, Scott, & Wadhwa, Meenakshi (2022) Highly Differentiated Basaltic Lavas Examined by PIXL in Jezero Crater. In Proceedings of the 53rd Lunar and Planetary Science Conference (LPSC). Lunar and Planetary Institute, United States of America.

Sephton, M.A., Wright, I.P., Gilmour, I., de Leeuw, J.W., Grady, M.M., Pillinger, C.T. (2002) High molecular weight organic matter in martian meteorites. *Planetary and Space Science* 50, 711-716.

Shahrzad, S., Kinch, K.M., Goudge, T.A., Fassett, C., Needham, D.H., Quantin-Nataf, C., Knudsen, C.P. (2019) Crater statistics on the dark-toned, mafic floor unit in Jezero crater, Mars. *Geophysical Research. Letters* 46 (5) 2408-2416.

Sharma S, Beegle LW, Bhartia R, and the SHERLOC Team (2022) 400 Sols of SHERLOC on Mars, GeoRaman 2022.

Sharma S, Roppel R, Murphy A, Beegle LW, Bhartia R, Steele A, Razzell Hollis J, Siljeström S, McCubbin FM, Asher SA, Abbey WJ, Allwood AC, Berger EL, Bleefeld BL, Burton AS, Bykov SV, Cardarelli EL, Conrad PG, Corpolongo A, Czaja AD, DeFlores LP, Edgett K, Farley KA, Fornaro T, Fox AC, Fries MD, Harker D, Hickman-Lewis K, Huggett J, Imbeah S, Jakubek RS, Kah LC, Lee C, Liu Y, Magee A, Minitti M, Moore KR, Pascuzzo A, Rodriquez C, Scheller EL, Shkolyar S, Stack KM, Steadman K, Tuite M, Uckert K, Werynski A, Wiens RC, Wiliams AJ, Winchell K, Wu M, Yanchilina A. (2022) Mapping organic-mineral associations in Jezero crater: Implications for Martian Organic Geochemistry, submitted to *Nature*.

Sholes, S.F., Stack K.M., Kah, L.C., Simon, J.I., Mangold, N. (2022) Topographic trends of the geologic units in Jezero Crate: Lake levels, potential shorelines, and the crater floor units, In

Proceedings of the 53rd Lunar and Planetary Science Conference (LPSC). Lunar and Planetary Institute, United States of America.

Shuster, D.L., Vasconcelos, P.M., Heim, J.A., Farley, K.A. (2005) Weathering geochronology by (U-Th)/He dating of goethite. *Geochimica et Comochimica Acta* 69, 659-673.

Shuster, D.L., Farley, K.A., Vasconcelos, P.M., Balco, G., Monteiro, H.S., Waltenberg, K., Stone, J.O. (2012) Cosmogenic 3He in hematite and goethite from Brazilian "canga" duricrust demonstrates the extreme stability of these surfaces. *Earth and Planetary Science Letters* 329-330, 41-50.

Simon, J.I., Christoffersen, R., Wang, J., Mouser*, M.D., Mills, R.D., Ross, D.K. Rahman, Z. (2020) Volatiles in lunar felsite clast: Impact-related delivery of hydrous materials to an ancient dry lunar crust. *Geochimica et Cosmochimica Acta* 276, 299-326.

Simon, J.I. (2022). Calcium isotope constraints on recycled carbonates in subduction-related magmas, In *Isotopic constraints on earth system processes*, pp. 43-56. https://doi.org/10.1002/9781119595007.ch3

Stack, K.M., Williams, N.R., Calef, F., Sun, V.Z., Williford, K.H., Farley, K.A., Eide, S., Flannery, D., Hughes, C., Jacob, S.R., Kah, L. C., Meyen, F., Molina, A., Nataf, C. Q.,Rice, M., Russell, P., Scheller, E., Seeger, C.H., Abbey, W.J., Adler, J.B., Amundsen, H., Anderson, R. B., Angel, S.M., Arana, G., Atkins, J., Barrington, M., Berger, T., Borden, R., Boring, B., Brown, A., Carrier, B.L., Conrad, P., Dypvik, H.,Fagents, S.A., Gallegos, Z.E., Garczynski, B., Golder, K., Gomez, F., Goreva, Y., Gupta, S., Hamran, S.-E., Hicks, T., Hinterman, E.D., Horgan, B.N., Hurowitz, J., Johnson, J.R., Lasue, J., Kronyak, R.E., Liu, Y., Madariaga, J.M., Mangold, N., McClean, J., Miklusicak, N., Nunes, D., Rojas, C., Runyon, K., Schmitz, N., Scudder, N., Shaver, E.,SooHoo, J., Spaulding, R., Stanish, E., Tamppari, L.K., Tice, M.M., Turenne, N., Willis, P.A., Aileen, Y.R. (2020) Photogeologic Map of the Perseverance Rover Field Site in Jezero Crater Constructed by the Mars 2020 Science Team. *Space Science Reviews* 216 (8) doi.org/10.1007/s11214-020-00739-x

Steele, A., McCubbin, F.M., Fries, M., Kater, L., Boctor, N.Z., Fogel, M.L., Conrad, P.G., Glamoclija, M., Spencer, M., Morrow, A.L., Hammond, M.R., Zare, R.N., Vicenzi, E., Siljeström, S., Bowden, R., Herd, C.D.K., Mysen, B.O., Shirey, S.B., Amundsen, H.E.F., Treiman, A.H., Bullock, E.S. and Jull, A.J.T. (2012) A reduced organic carbon component in martian basalts. *Science* 337, 212-215.

Steele, A., McCubbin, F.M. and Fries, M.D. (2016) The provenance, formation, and implications of reduced carbon phases in Martian meteorites. *Meteoritics & Planetary Science* 51, 2203-2225.

Steele, A., Benning, L.G., Wirth, R., Siljeström, S., Fries, M.D., Hauri, E., Conrad, P.G., Rogers, K., Eigenbrode, J., Schreiber, A., Needham, A., Wang, J.H., McCubbin, F.M., Kilcoyne, D. and Blanco, J.D.R. (2018) Organic synthesis on Mars by electrochemical reduction of CO_2 *Science Advances* 4, eaat5118.

Steele, A., Benning, L.G., Wirth, R., Schreiber, A., Araki, T., McCubbin, F.M., Fries, M.D., Nittler, L.R., Wang, J., Hallis, L.J., Conrad, P.G., Conley, C., Vitale, S., O'Brien, A.C., Riggi, V. and Rogers, K. (2022) Organic synthesis associated with serpentinization and carbonation on early Mars. *Science* 375, 172-177.

Steiner, M.H., Hausrath, E.M., Madden, M.E., Tschauner, O., Ehlmann, B.L., Olsen, A.A., Gainey, S.R., Smith, J.S. (2016) Dissolution of nontronite in chloride brines and implications for the aqueous history of Mars. *Geochimica et Cosmochimica Acta* 195, 259-276.

Sun V. Z., Hand K. P., Stack K. M., Farley K. A., Milkovich S., Kronyak R., Simon J. I., Hickman-Lewis K., Shuster D., Bell III J. F., Gupta S., Herd C.D. K., Maurice S., Paar G., C. Wiens R., and the Mars 2020 Science Team (2022) Exploring the Jezero crater floor: overview of results from the Mars 2020 Perseverance Rover's first science campaign, In Proceedings of the 53rd Lunar and Planetary Science Conference (LPSC). Lunar and Planetary Institute, United States of America.

Swindle, T.D., Atreya, S., Busemann, H., Cartwright, J.A., Mahaffy, P., Marty, B., Pack, A. and Schwenzer, S.P. (2022) Scientific Value of Including an Atmospheric Sample as Part of Mars Sample Return (MSR). *Astrobiology* 22, S-165-S-175.

Summons, R.E., Amend, J.P., Bish, D., Buick, R., Cody, G.D., Des Marais, D.J., Dromart, G., Eigenbrode, J.L., Knoll, A.H., Sumner, D.Y. (2011) Preservation of martian organic and environmental records: final report of the Mars biosignature working group, *Astrobiology*, 157-181. http://doi.org/10.1089/ast.2010.0506

Tait, K.T., McCubbin, F.M., Smith, C.L., Agee, C.B., Busemann, H., Cavalazzi, B., Debaille, V., Hutzler, A., Usui, T., Kminek, G., Meyer, M.A., Beaty, D.W., Carrier, B.L., Haltigin, T.H., Hays, L.E., Cockell, C.S., Glavin, D.P., Grady, M.M., Hauber, E., Marty, B., Pratt, L.M., Regberg, A.B., Smith, A.L., Summons, R.E., Swindle, T.D., Tosca, N.J., Udry, A., Velbel, M.A., Wadhwa, M., Westall, F. and Zorzano, M.-P. (2022) Preliminary Planning for Mars Sample Return (MSR) Curation Activities in a Sample Receiving Facility (SRF). *Astrobiology* 22, S-57-S-80.

Tait, K. T., & Day, J. M. (2018). Chondritic late accretion to Mars and the nature of shergottite reservoirs. *Earth and Planetary Science Letters* 494, 99-108.

Tanaka, K. L., Skinner, J. A. Jr., Dohm, J. M., Irwin, R. P. III, Kolb, E. J., Fortezzo, C. M., Platz, T., Michael, G. G., Hare, T. M. (2014). Geologic map of Mars. Retrieved from http://pubs.usgs.gov/sim/3292/

Teng, F.-Z., Dauphas, N., Helz, R.T., Gao, S., Huang, S. (2011) Diffusion-driven magnesium and iron isotope fractionation in Hawaiian olivine, *Earth and Planetary Science Letters* 308, 317-324.

Teng, F.-Z., Dauphas, N., & Watkins, J. M. (2017). Non-traditional stable isotopes: Retrospective and prospective, in *Reviews in Mineralogy and Geochemistry* 82(1), 1–26. https://doi.org/10.2138/rmg.2017.82.1

Tice et al., M.M., Hurowitz, J. A., Allwood, A.C., Jones, M.W., Brendan, M., Orenstein, J., Davidoff, S., Wright, A.P., Pedersen, David, A.K., Henneke, J., Tosca, N.J., Moore, K.R., Clark, B.C., McLennan, S.M., Flannery, D.T., Steele, A., Brown, A.J., Zorzano, M.-P., Hickman-Lewis, K., Liu, Y., VanBommel, S.J., Schmidt, M.E., Kizovski, T.V., Treiman, A.H., O'Neil, L., Fairén, A.G., Shuster, D.L., Gupta, S. and the PIXL Team (2022) Alteration History of Séítah Formation Rocks Inferred by PIXL X-ray Fluorescence, X-ray Diffraction, and Multispectral Imaging on Mars, *Science Advances* 8 (47) DOI: 10.1126/sciadv.abp9084.

Tomascak, P.B. (2004) Developments in the Understanding and Application of Lithium Isotopes in the Earth and Planetary Sciences, *Reviews in Mineralogy & Geochemistry,* Vol. 55, pp. 153-195.

Treiman, A.H., Bish, D.L., Vaniman, D.T., Chipera, S.J., Blake, D.F., Ming, D.W., Morris, R.V., Bristow, T.F., Morrison, S.M., Baker, M.B., Rampe, E.B., Downs, R.T., Filiberto, J., Glazner, A.F., Gellert, R., Thompson, L.M., Schmidt, M.E., Le Deit, L., Wiens, R.C., McAdam, A.C., Achilles, C.E., Edgett, K.S., Farmer, J.D., Fendrich, K.W., Grotzinger, J.P., Gupta, S., Morookian, J.M., Newcombe, M.E., Rice, M.S., Spray, J.G., Stolper, E.M., Sumner, D.Y., Vasavada, A.R., Yen, A.S. (2015) *J. Geophysical Res. Planets* 121 (1), 75-106.

Udry, A., Howarth, G. H., Lapen, T. J., & Righter, M. (2017). Petrogenesis of the NWA 7320 enriched martian gabbroic shergottite: Insight into the martian crust. *Geochimica et Cosmochimica Acta* 204(3), 1–18. https://doi.org/10.1016/j.gca.2017.01.032.

Udry A., Howarth, G.H., Herd, C.D.K., Day, J.M.D., Lapen, T.J., Filiberto, J. (2020) What martian meteorites reveal about the interior and surface of Mars, *J. Geophysical. Res. Planets* 125 (12) e2020JE006523.

Udry A., Sautter V., Cousin, A., Wiens R. C., Forni O., Benzerara K., Beyssac O., Nachon M., Dromart G., Quantin C., Mandon L., Clavé E., Pinet P., Ollila A., Bosak T., Mangold N., Dehouck E., Johnson J., Schmidt M., Horgan B., Gabriel T., McLennan S., Maurice S., Simon J.I., Herd C. D. K., Madiaraga J. M. (2022) Mars 2020 Perseverance SuperCam Perspective on the Igneous Nature of the Máaz formation at Jezero crater, Mars. Journal of Geophysical Research: Planets, 127, e2022JE007440.

Usui, T., McSween, H.Y. and Clark, B.C. (2008) Petrogenesis of high-phosphorous Wishstone Class rocks in Gusev Crater, Mars. *J. Geophysical Res. Planets* 113, 13.

Usui, T., Alexander, C.M.O.D., Wang, J., Simon, J.I. and Jones, J.H. (2012) Origin of water and mantle–crust interactions on Mars inferred from hydrogen isotopes and volatile element abundances of olivine-hosted melt inclusions of primitive shergottites. *Earth and Planetary Science Letters* 357–358, 119-129.

Usui, T., Alexander, C.M.O'D., Wang, J., Simon, J.I., Jones, J.H. (2015) Meteoritic evidence for a previously unrecognized hydrogen reservoir on Mars. *Earth and Planetary Science Letters* 410, 140-151.

Van Herk, J., Pietersen, H.S., Schuiling, R.D., 1989. Neutralization of industrial waste acids with olivine - The dissolution of forsteritic olivine at 40-70º C. Chemical Geology 76, 341-352.

Vervelidou, F., Lesur, V., Grott, M., Morshhauser, A., Lillis, R. (2017) Constraining the date of the martian dynamo shutdown by means of crater magnetization signatures. *J. Geophysical Res. Planets* 122, 2,294-2,311, https://doi.org/10.1002/2017JE005410.

Wacey, D., Mcloughlin, N., Brasier, M.D. (2009). Looking Through Windows onto the Earliest History of Life on Earth and Mars. In: Seckbach, J., Walsh, M. (eds) From Fossils to

Astrobiology. Cellular Origin, Life in Extreme Habitats and Astrobiology, vol 12. Springer, Dordrecht. https://doi.org/10.1007/978-1-4020-8837-7_3

Walton, E.L., Kelly, S.P., Herd, C.D.K. (2008) Isotopic and petrographic evidence for young Martian basalts, *Geochimica et Cosmochimica Acta* 72 (23), 5819-5837.

Warren, P.H., Kallemeyn, G.M. (1994) Siderophile trace elements in ALH84001, other SNC meteorites and eucrites: Evidence of heterogeneity, possibly time-linked, in the mantle of Mars, *Meteoritics & Planetary Science* 31 (1), 97-105.

Watkins, J.M., DePaolo, D.J., Huber, C., Ryerson, F.J. (2009) Liquid composition-dependence of calcium isotope fractionation during diffusion in molten silicates, *Geochimica et Cosmochimica Acta* 73, 7341-7359.

Wiens, Roger C., Sylvestre Maurice, Scott H. Robinson, Anthony E. Nelson, Philippe Cais, Pernelle Bernardi, Raymond T. Newell, et al. (2020) "The SuperCam Instrument Suite on the NASA Mars 2020 Rover: Body Unit and Combined System Tests." *Space Science Reviews* 217, 4. https://doi.org/10.1007/s11214-020-00777-5.

Wiens et al., (2022) Compositionally and Density Stratified Igneous Terrain in Jezero Crater, Mars, *Science Advances* 8, DOI: 10.1126/sciadv.abo3399.

Weiss, B.P., Kim, S.S., Kirschvink, J.L., Kopp, R.E., Sankaran, M., Kobayshi, A., Komeili, A. (2004) Magnetic tests for magnetosome chains in Martian meteorite ALH84001. *PNAS* 101(22), 8,281-8,284, https://doi.org/10.1073/pnas.0402292101.

Werner, S.C. (2008) The early martian evolution—Constraints from basin formation ages. *Icarus* 195, 45-60.

Westall, F., Foucher, F., Bost, N., Bertrand, M., Loizeau, D., Vago, J.L., Kminek, G., Gaboyer, F., Campbell, K. A., Bréhéret, J.-G., Gautret, P., Cockell, C. S. (2015) *Astrobiology*, doi.org/10.1089/ast.2015.1374.

Westall, F. and Brack, A. (2018) The Importance of Water for Life. *Space Science Reviews* 214.

Williford, K. H., Farley, K. A., Stack, K. M., Allwood, A. C., Beaty, D., Beegle, L. W. , Bhartia, R., Brown, A. J., de la Torre Juarez, M., Hamran, S.-E., Hecht, M. H., Hurowitz, J. A., Rodriguez-Manfredi, J. A., Maurice, S., Milkovich, S., Wiens, R. C. (2018) Chapter 11 - The NASA Mars 2020 Rover Mission and the Search for Extraterrestrial Life, Editor(s): Nathalie A. Cabrol, Edmond A. Grin, From Habitability to Life on Mars, Elsevier, Pages 275-308, ISBN 9780128099353, https://doi.org/10.1016/B978-0-12-809935-3.00010-4.

Wogelius, R.A., Walther, J.V., 1992. Olivine dissolution kinetics at near-surface conditions. *Chemical Geology* 97, 101-112.

Yen, A. S., Mittlefehldt, D. W., McLennan, S. M., Gellert, R., Bell III, J. F., McSween Jr., H. Y., Ming, D. W., McCoy, T. J., Morris, R. V., Golombek, M., Economou, T., Madsen, M. B., Wdowiak, T., Clark, B. C., Jolliff, B. L., Schröder, C., Brückner, J., Zipfel, J., Squyres, S. W. (2006) Nickel on Mars: Constraints on meteoritic material at the surface. *J. Geophys. Res.* 111, 12S11, doi:10.1029/2006JE002797.

Zastrow and Glotch (2021) Distinct Carbonate Lithologies in Jezero Crater, Mars. *Geophysical Research Letters*, 10.1029/2020GL092365.

Zhang, L., Wang, Q., Ding., X., Li, W.-C. (2021) Diverse serpentinization and associated abiotic methanogenesis within multiple types of olivine-hosted fluid inclusions in orogenic peridotite from northern Tibet. *Geochimica et Cosmochimica* Acta 296, 1-17.

Figure 1.

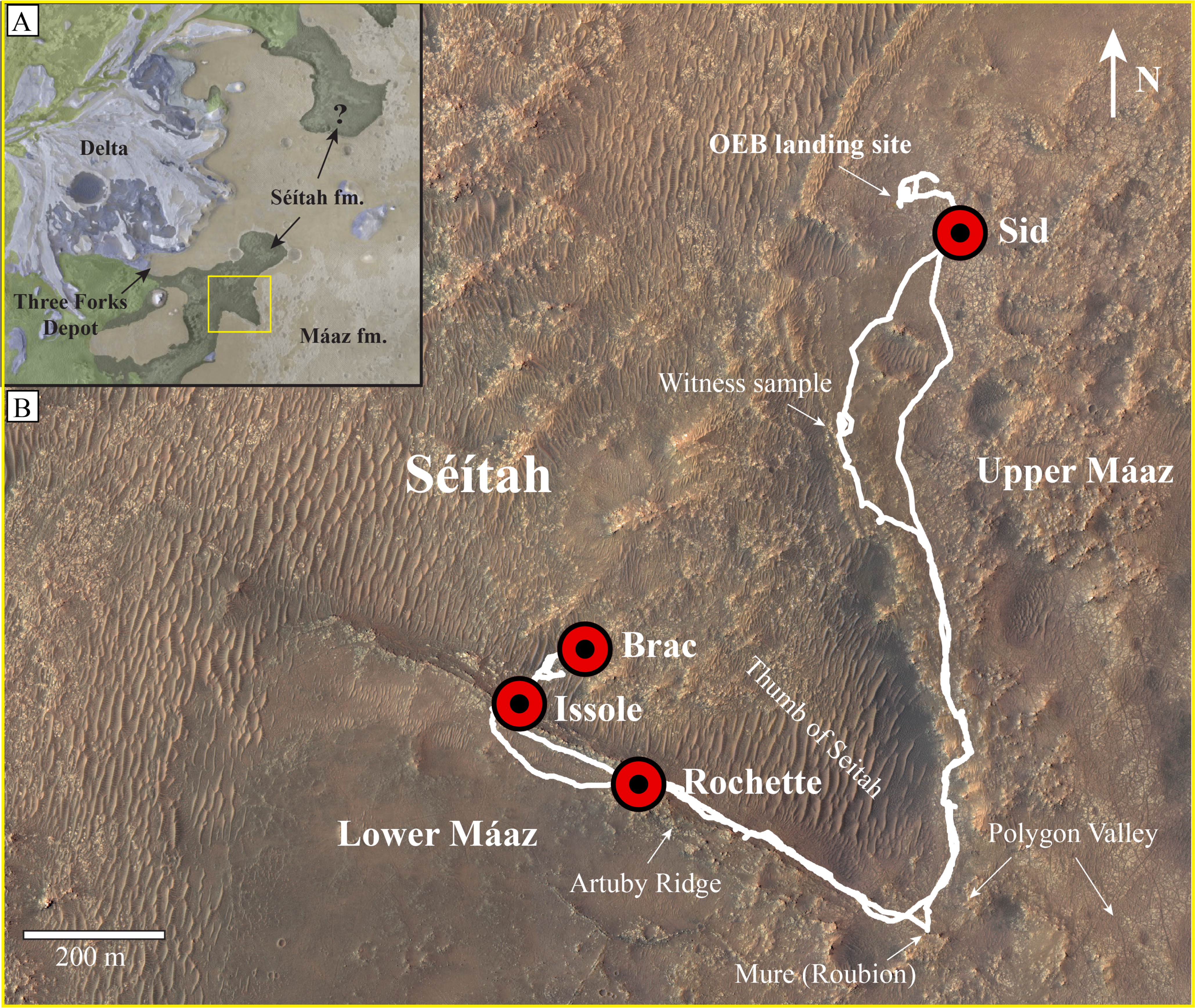

A
Delta
Séítah fm.
?
Three Forks
Depot
Máaz fm.
B
N
OEB landing site
Sid
Witness sample
Séítah
Upper Máaz
Brac
Issole
Thumb of Séítah
Rochette
Lower Máaz
Polygon Valley
Artuby Ridge
200 m
Mure (Roubion)

Figure 2.

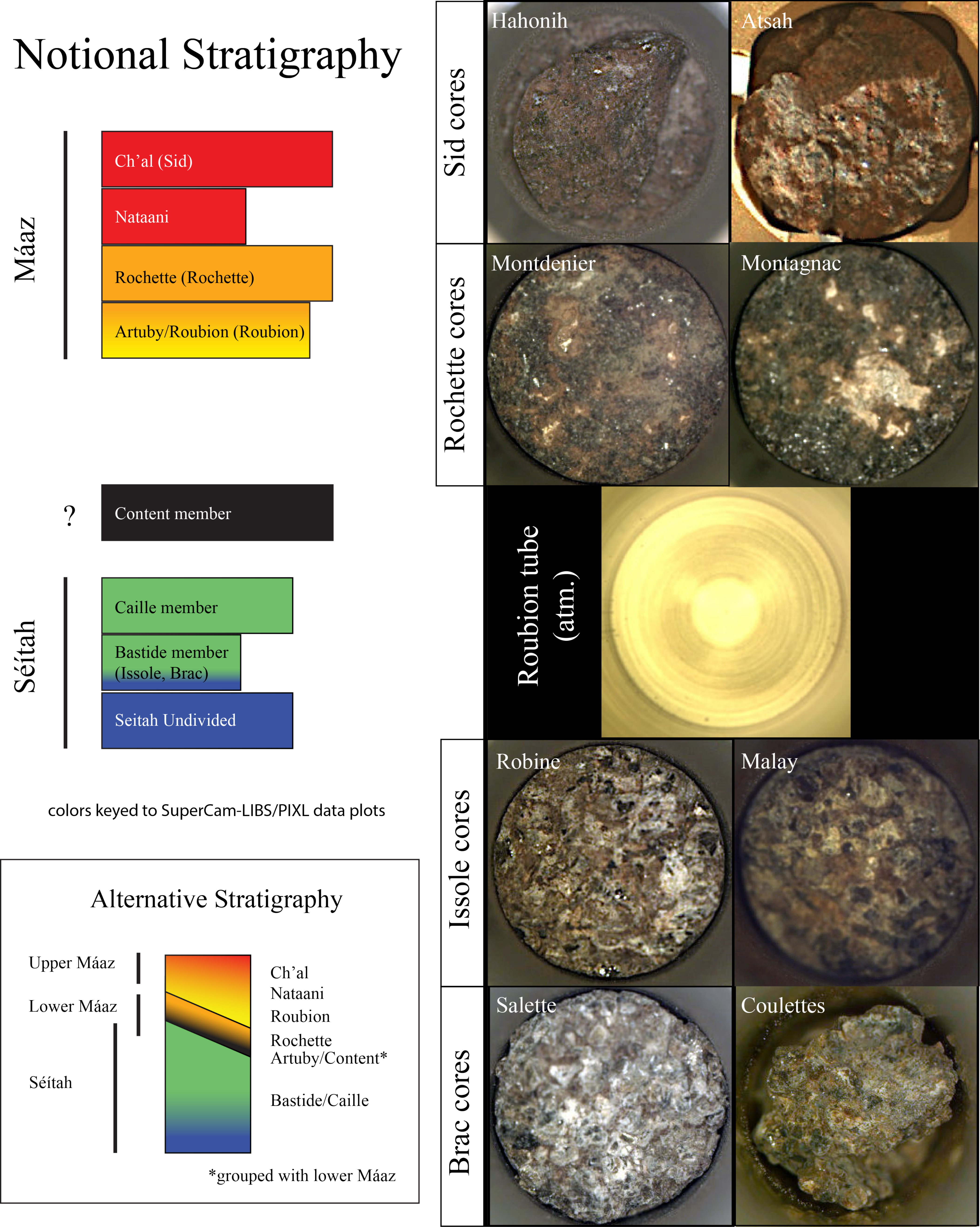
Notional Stratigraphy
Máaz
Ch'al (Sid)
Nataani
Rochette (Rochette)
Artuby/Roubion (Roubion)
?
Content member
Séítah
Caille member
Bastide member (Issole, Brac)
Seitah Undivided
colors keyed to SuperCam-LIBS/PIXL data plots
Alternative Stratigraphy
Upper Máaz
Lower Máaz
Séítah
Ch'al
Nataani
Roubion
Rochette
Artuby/Content*
Bastide/Caille
*grouped with lower Máaz
Sid cores
Hahonih
Atsah
Rochette cores
Montdenier
Montagnac
Roubion tube (atm.)
Issole cores
Robine
Malay
Brac cores
Salette
Coulettes

Figure 3.

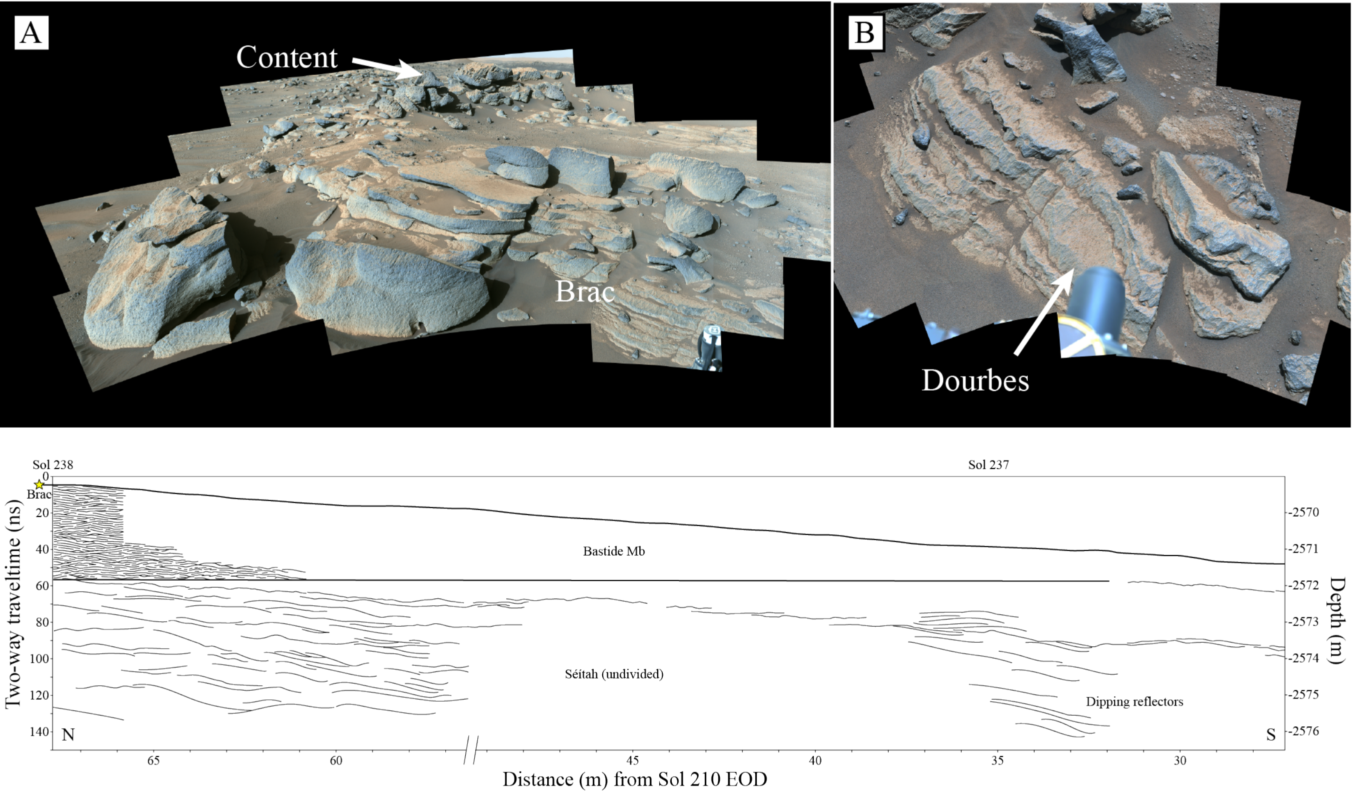
A
Content
Brac
B
Dourbes
Sol 238
Sol 237
Brac
Bastide Mb
Séítah (undivided)
Dipping reflectors
N
S
Two-way traveltime (ns)
Depth (m)
Distance (m) from Sol 210 EOD
0
20
40
60
80
100
120
140
-2570
-2571
-2572
-2573
-2574
-2575
-2576
65
60
45
40
35
30

Figure 4.

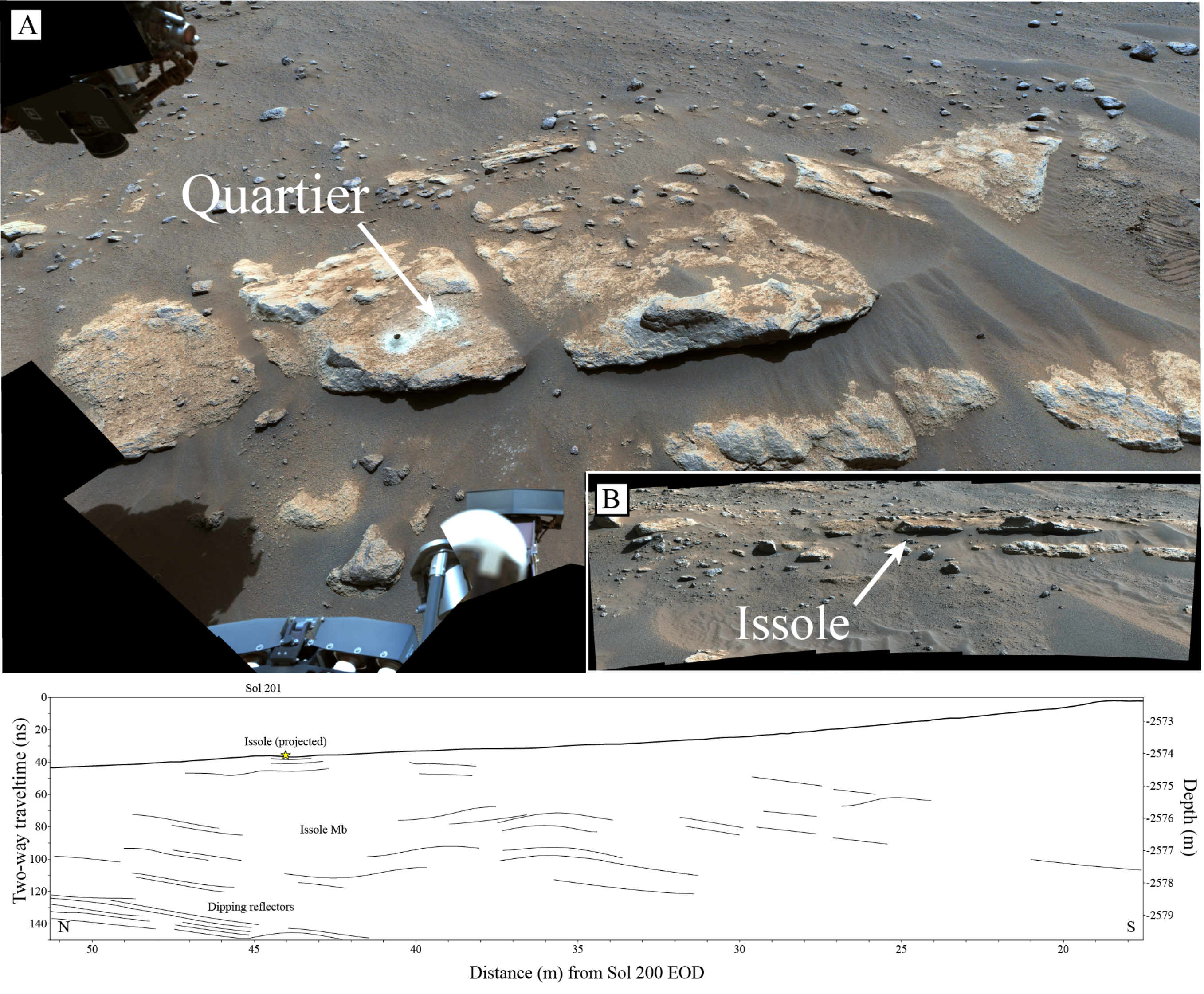
A
Quartier
B
Issole
Sol 201
Issole (projected)
Issole Mb
Dipping reflectors
N
S
Two-way traveltime (ns)
0
20
40
60
80
100
120
140
Depth (m)
-2573
-2574
-2575
-2576
-2577
-2578
-2579
50
45
40
35
30
25
20
Distance (m) from Sol 200 EOD

Figure 5.

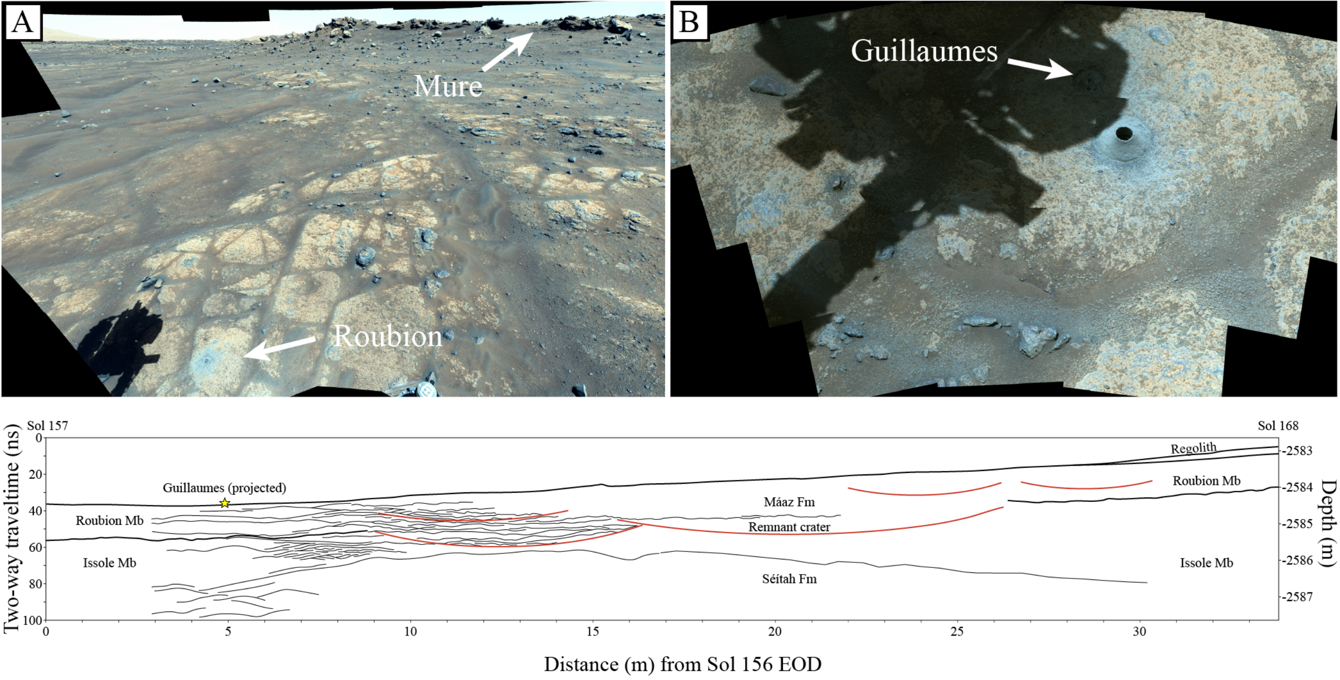
A
Mure
Roubion
B
Guillaumes
Sol 157
Sol 168
Two-way traveltime (ns)
0
20
40
60
80
100
Guillaumes (projected)
Roubion Mb
Issole Mb
Máaz Fm
Remnant crater
Séítah Fm
Regolith
Roubion Mb
Issole Mb
-2583
-2584
-2585
-2586
-2587
Depth (m)
0
5
10
15
20
25
30
Distance (m) from Sol 156 EOD

Figure 6.

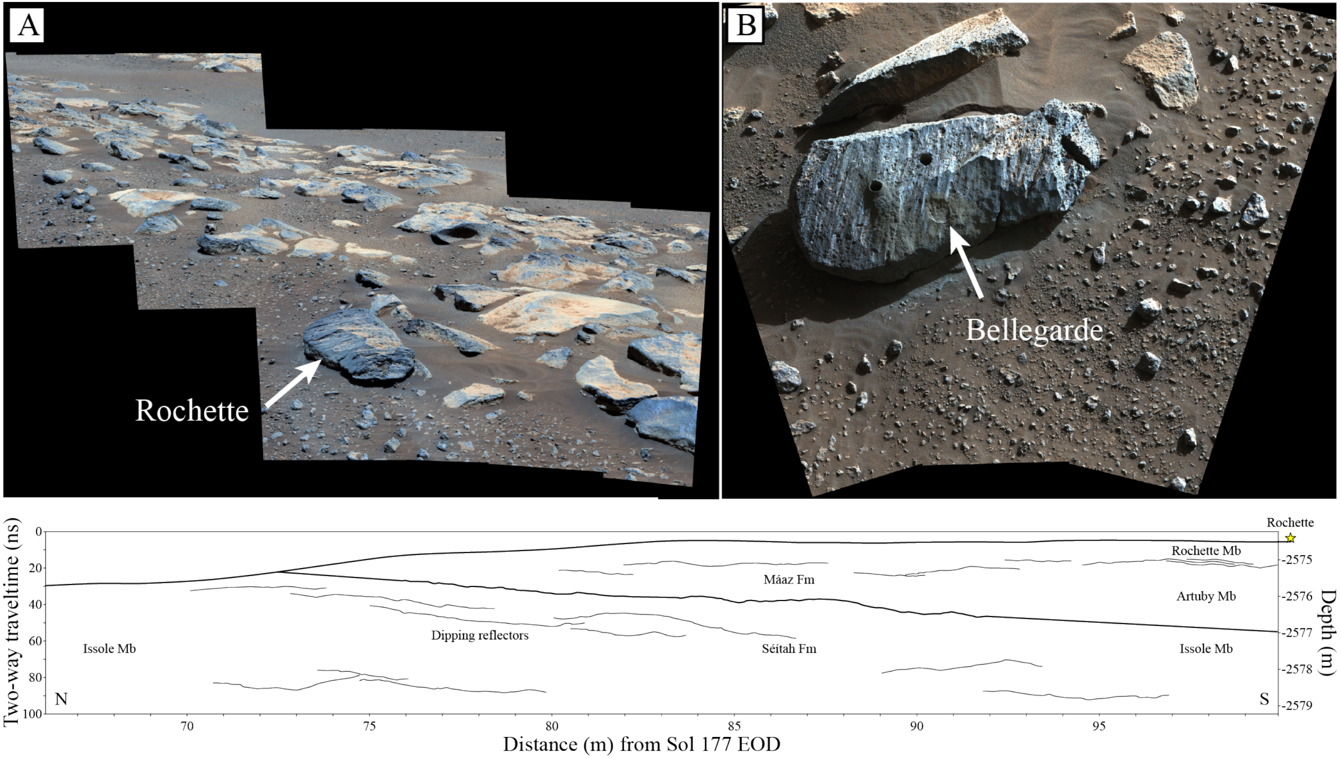

A
Rochette
B
Bellegarde
Rochette
Rochette Mb
Máaz Fm
Artuby Mb
Dipping reflectors
Issole Mb
Séítah Fm
Issole Mb
N
S
Two-way traveltime (ns)
0
20
40
60
80
100
Depth (m)
-2575
-2576
-2577
-2578
-2579
70
75
80
85
90
95
Distance (m) from Sol 177 EOD

Figure 7.

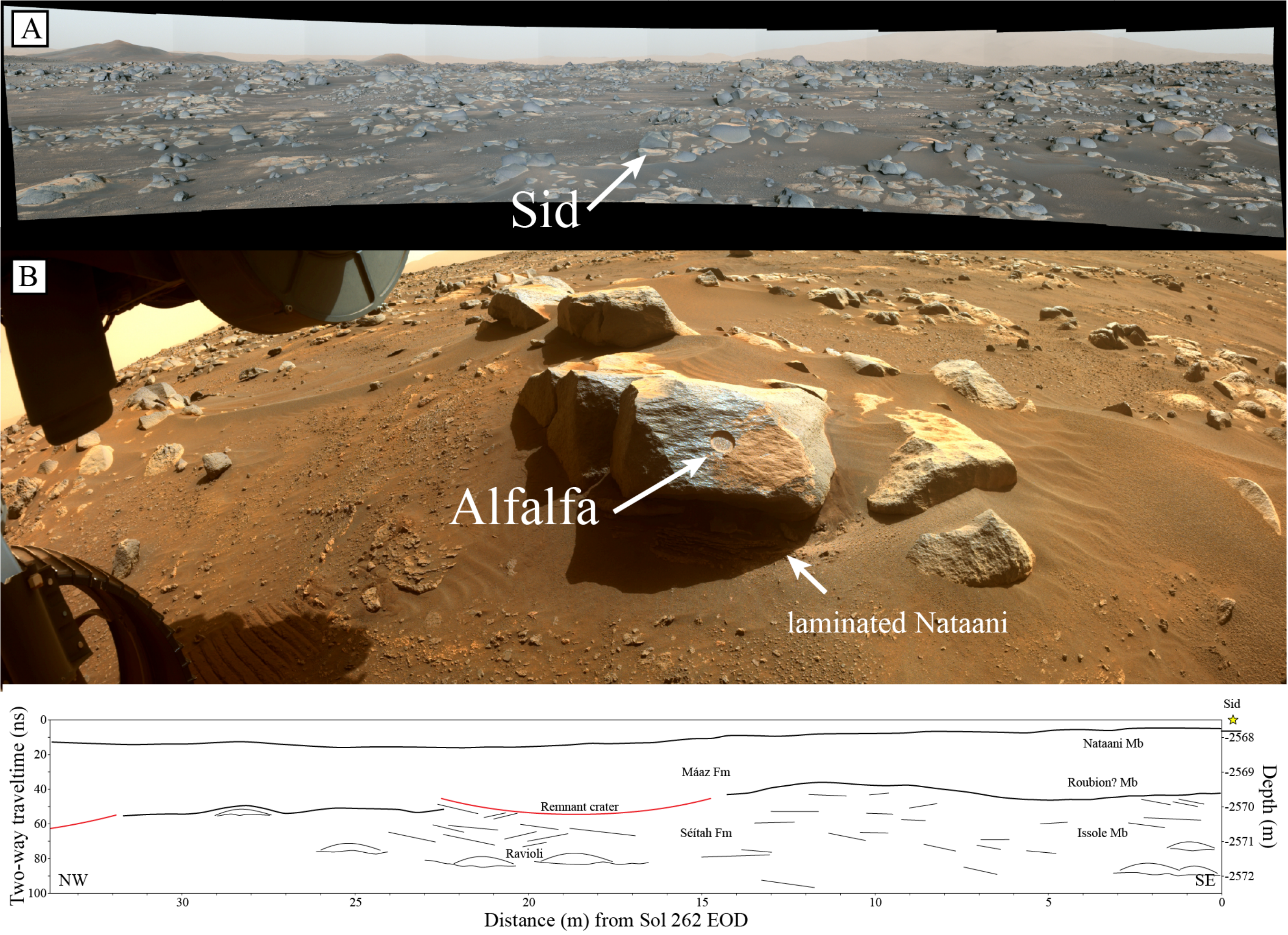

A
Sid
B
Alfalfa
laminated Nataani
Sid
Two-way traveltime (ns)
Depth (m)
Nataani Mb
Máaz Fm
Roubion? Mb
Remnant crater
Séítah Fm
Issole Mb
Ravioli
NW
SE
Distance (m) from Sol 262 EOD

Figure 8.

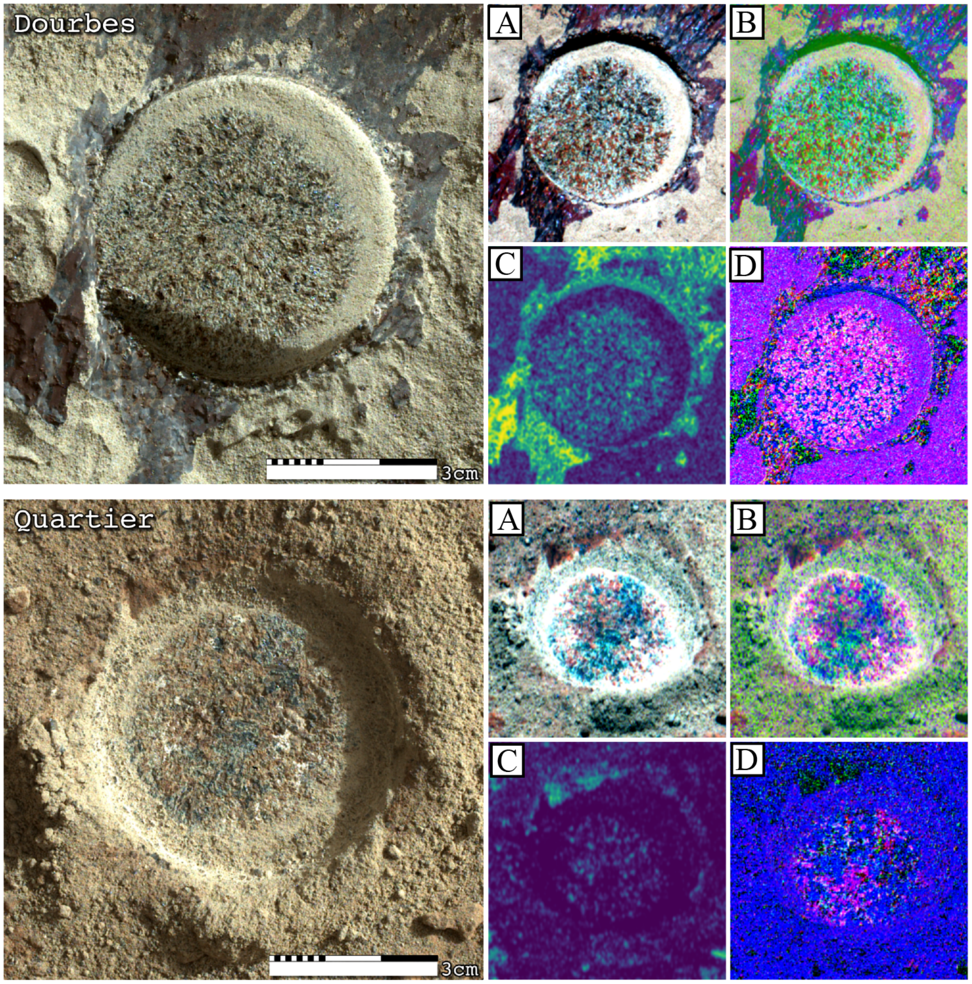

Dourbes
A
B
C
D
3cm
Quartier
A
B
C
D
3cm

Figure 9.

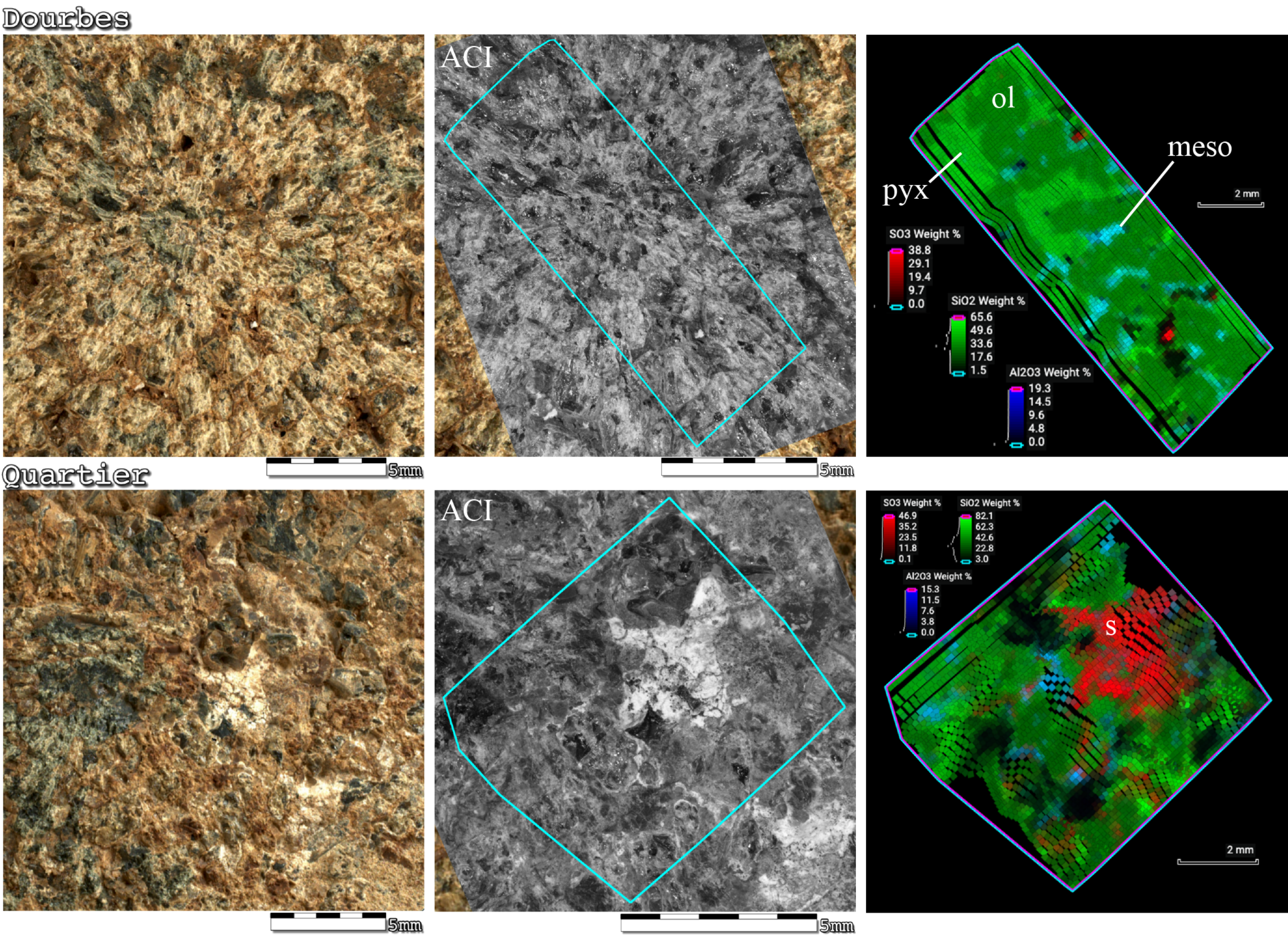

Dourbes
ACI
ol
meso
pyx
2 mm
SO3 Weight %
38.8
29.1
19.4
9.7
0.0
SiO2 Weight %
65.6
49.6
33.6
17.6
1.5
Al2O3 Weight %
19.3
14.5
9.6
4.8
0.0
5mm
5mm
Quartier
ACI
SO3 Weight %
46.9
35.2
23.5
11.8
0.1
SiO2 Weight %
82.1
62.3
42.6
22.8
3.0
Al2O3 Weight %
15.3
11.5
7.6
3.8
0.0
S
2 mm
5mm
5mm

Figure 10.

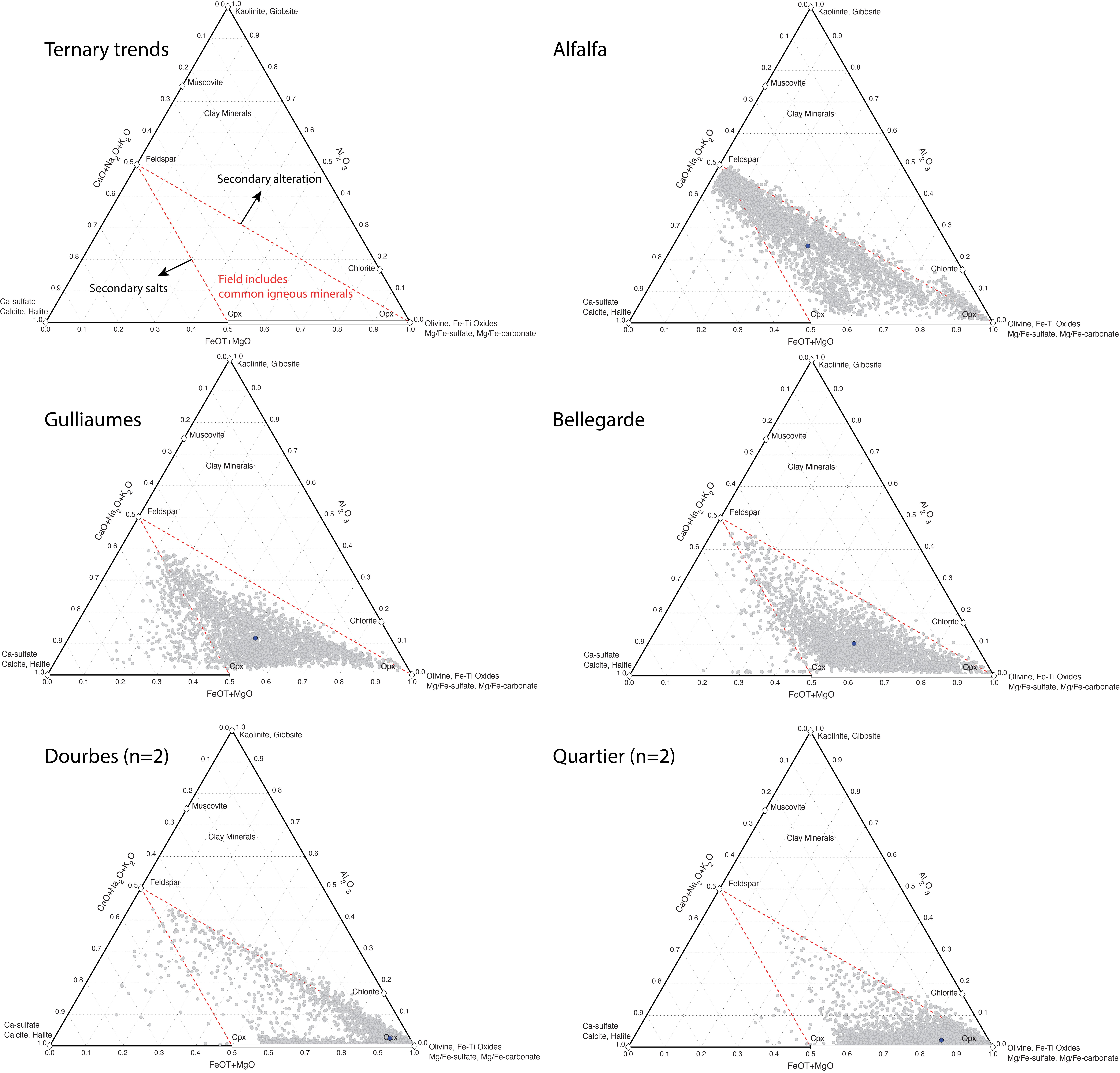

Ternary trends
Kaolinite, Gibbsite
Muscovite
Clay Minerals
Feldspar
Secondary alteration
Secondary salts
Field includes
common igneous minerals
Chlorite
Ca-sulfate
Calcite, Halite
Cpx
Opx
Olivine, Fe-Ti Oxides
Mg/Fe-sulfate, Mg/Fe-carbonate
CaO+Na2O+K2O
Al2O3
FeOT+MgO
Alfalfa
Gulliaumes
Bellegarde
Dourbes (n=2)
Quartier (n=2)

Figure 11.

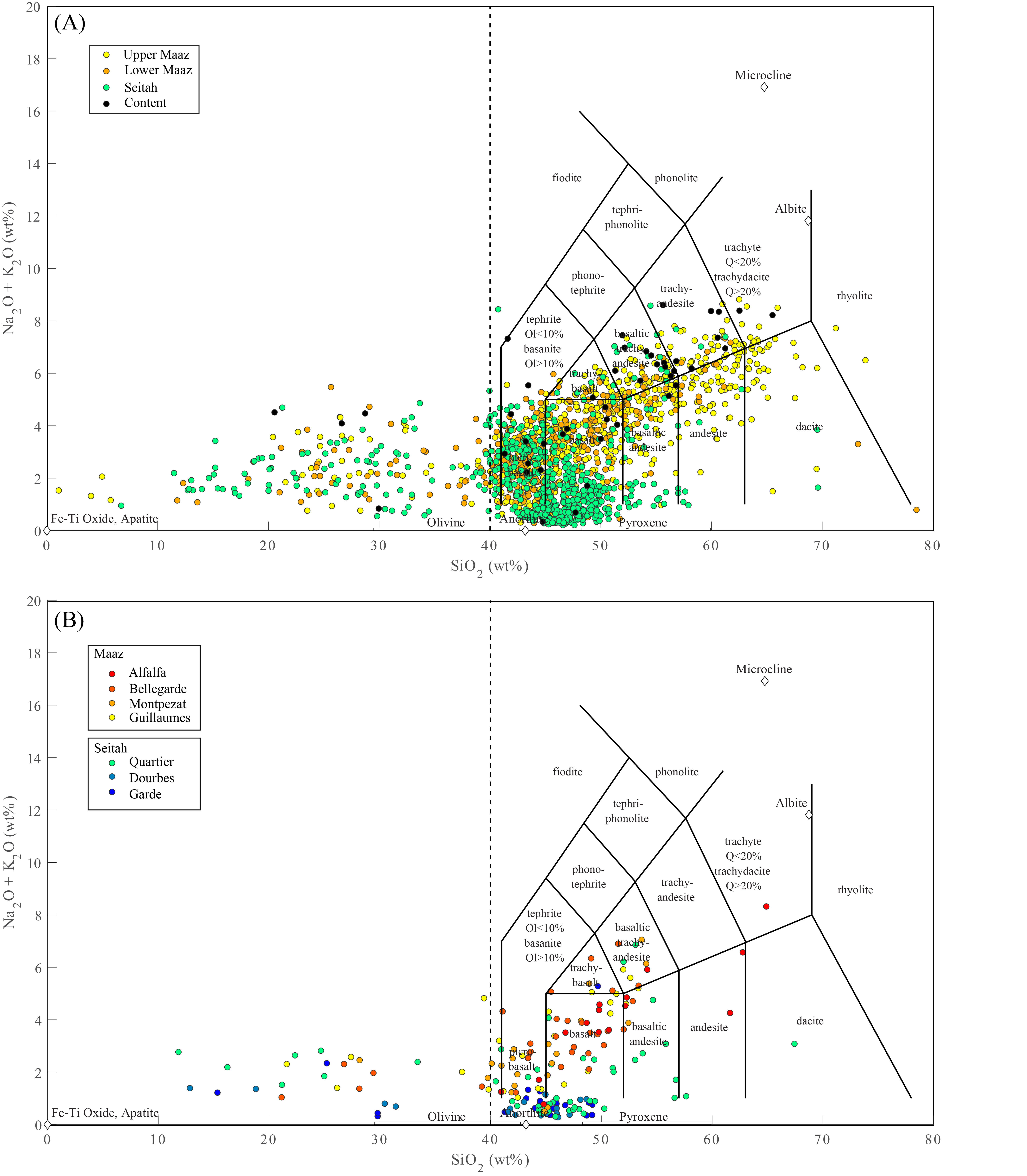
(A)
Upper Maaz
Lower Maaz
Seitah
Content
Microcline
Albite
fiodite
phonolite
tephri-
phonolite
phono-
tephrite
trachyte
Q<20%
trachydacite
Q>20%
trachy-
andesite
rhyolite
tephrite
Ol<10%
basanite
Ol>10%
basaltic
trachy-
andesite
trachy-
basalt
basalt
basaltic
andesite
andesite
dacite
Fe-Ti Oxide, Apatite
Olivine
Anorthite
Pyroxene
Na2O + K2O (wt%)
SiO2 (wt%)
(B)
Maaz
Alfalfa
Bellegarde
Montpezat
Guillaumes
Seitah
Quartier
Dourbes
Garde
picro-
basalt

Figure 12.

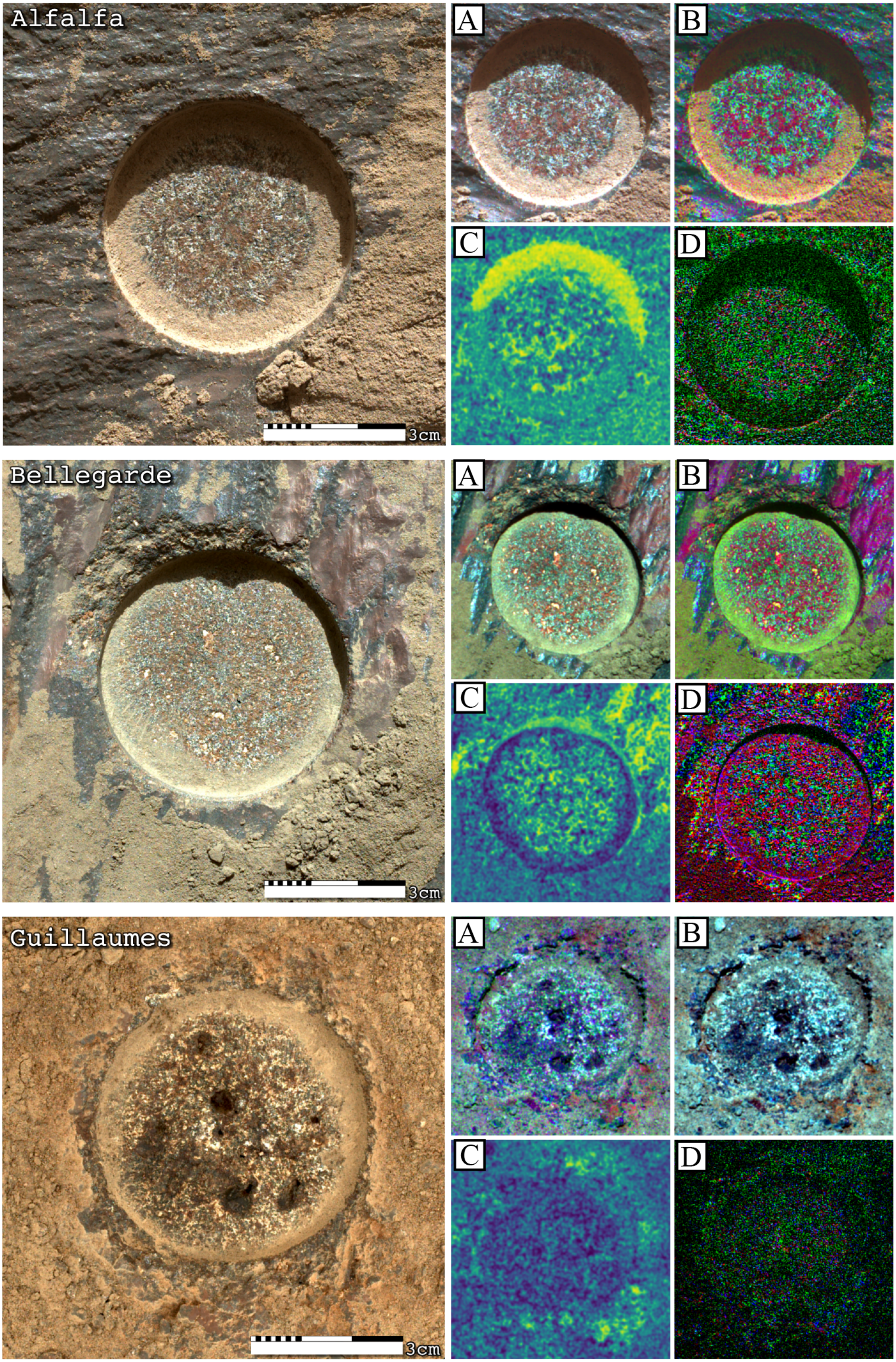
Alfalfa
A
B
C
D
3cm
Bellegarde
A
B
C
D
3cm
Guillaumes
A
B
C
D
3cm

Figure 13.

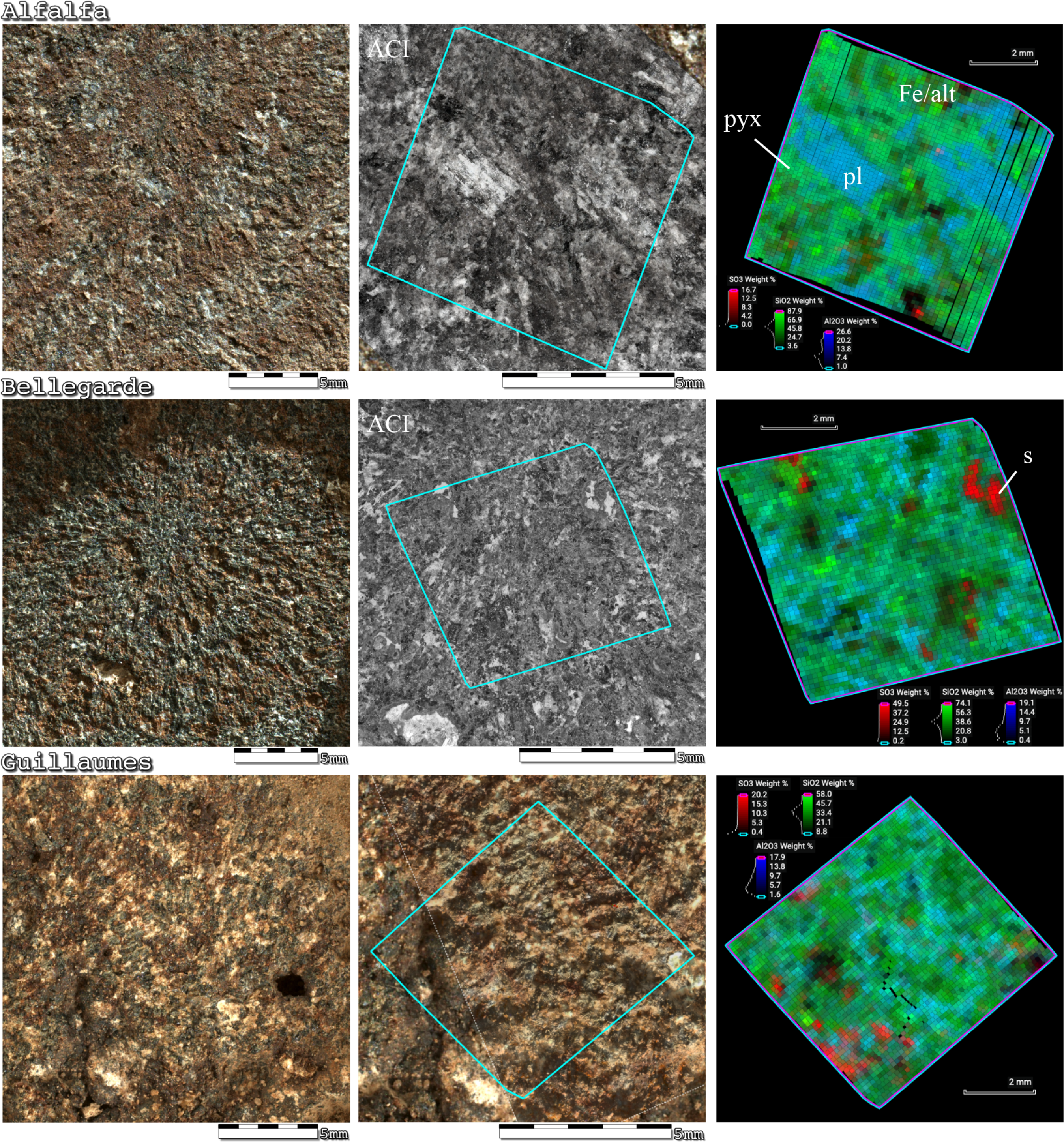
Alfalfa
ACI
5mm
5mm
pyx
Fe/alt
pl
2 mm
SO3 Weight %
16.7
12.5
8.3
4.2
0.0
SiO2 Weight %
87.9
66.9
45.8
24.7
3.6
Al2O3 Weight %
26.6
20.2
13.8
7.4
1.0
Bellegarde
ACI
5mm
5mm
2 mm
s
SO3 Weight %
49.5
37.2
24.9
12.5
0.2
SiO2 Weight %
74.1
56.3
38.6
20.8
3.0
Al2O3 Weight %
19.1
14.4
9.7
5.1
0.4
Guillaumes
5mm
5mm
SO3 Weight %
20.2
15.3
10.3
5.3
0.4
SiO2 Weight %
58.0
45.7
33.4
21.1
8.8
Al2O3 Weight %
17.9
13.8
9.7
5.7
1.6
2 mm

Figure 14.

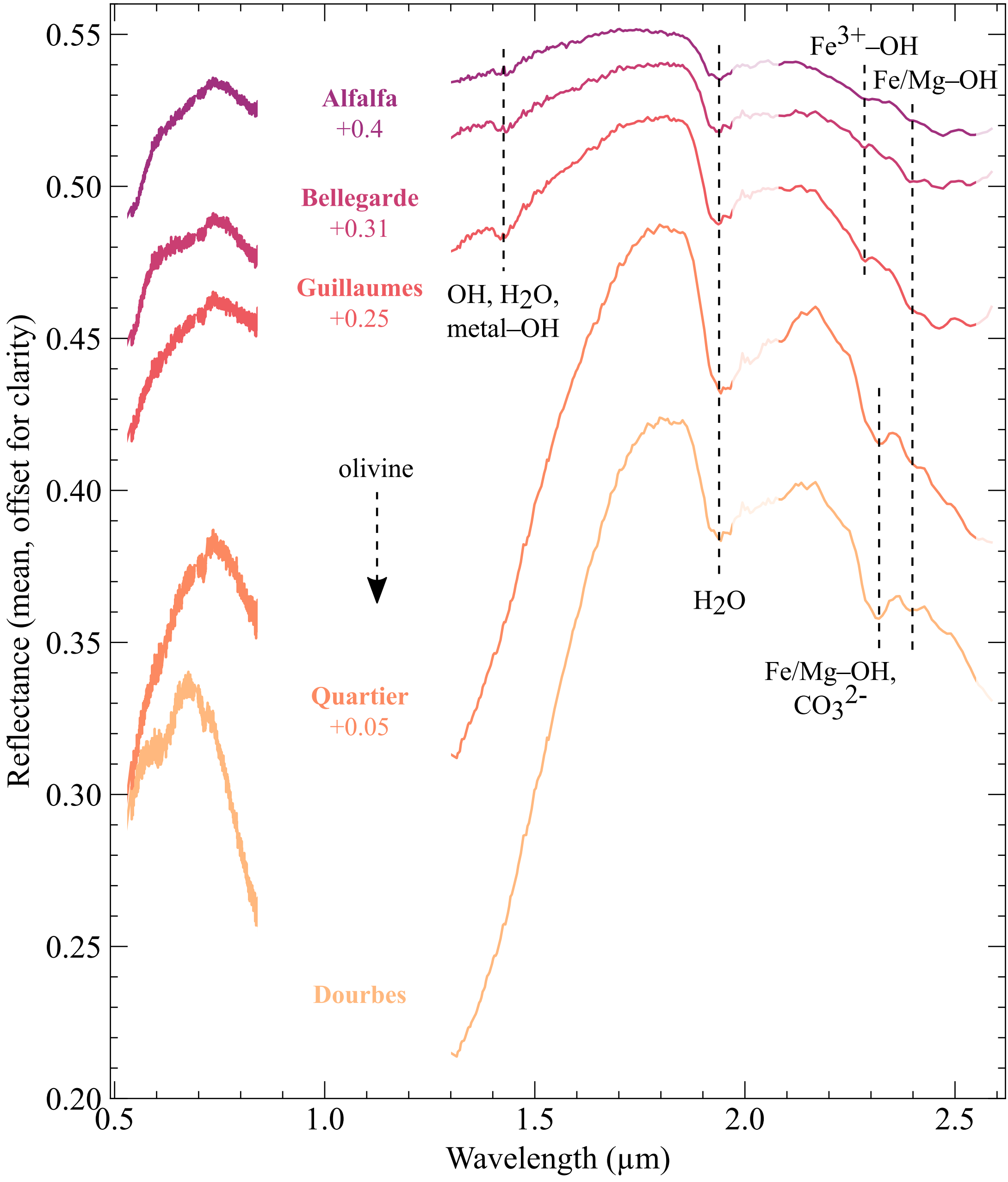

Alfalfa
+0.4
Bellegarde
+0.31
Guillaumes
+0.25
Quartier
+0.05
Dourbes
olivine
OH, H2O,
metal–OH
H2O
Fe3+–OH
Fe/Mg–OH
Fe/Mg–OH,
CO3 2-
Reflectance (mean, offset for clarity)
Wavelength (μm)
0.55
0.50
0.45
0.40
0.35
0.30
0.25
0.20
0.5
1.0
1.5
2.0
2.5

Figure 15.

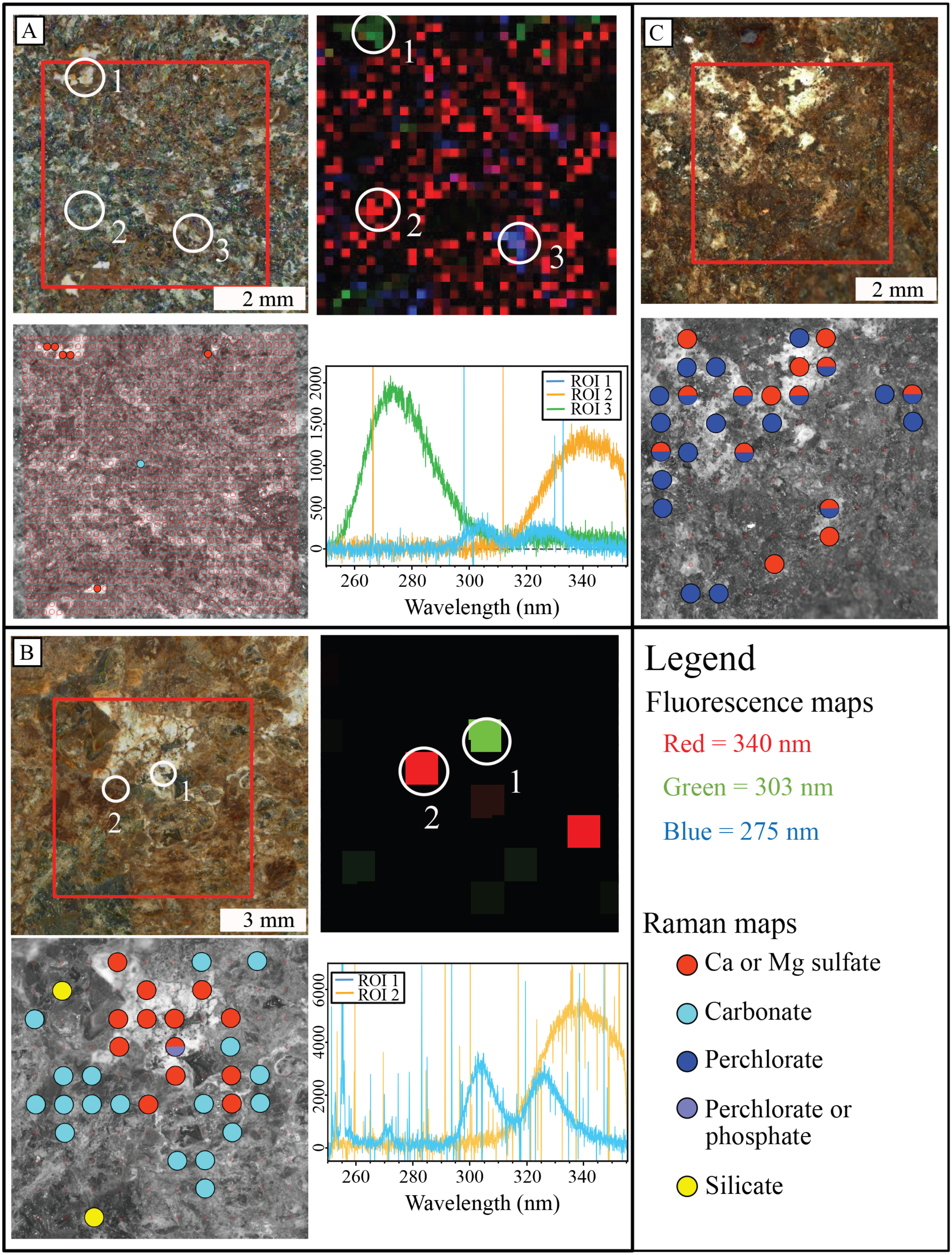

A
1
2
3
2 mm
ROI 1
ROI 2
ROI 3
Wavelength (nm)
B
3 mm
C
Legend
Fluorescence maps
Red = 340 nm
Green = 303 nm
Blue = 275 nm
Raman maps
Ca or Mg sulfate
Carbonate
Perchlorate
Perchlorate or phosphate
Silicate

Figure 16.

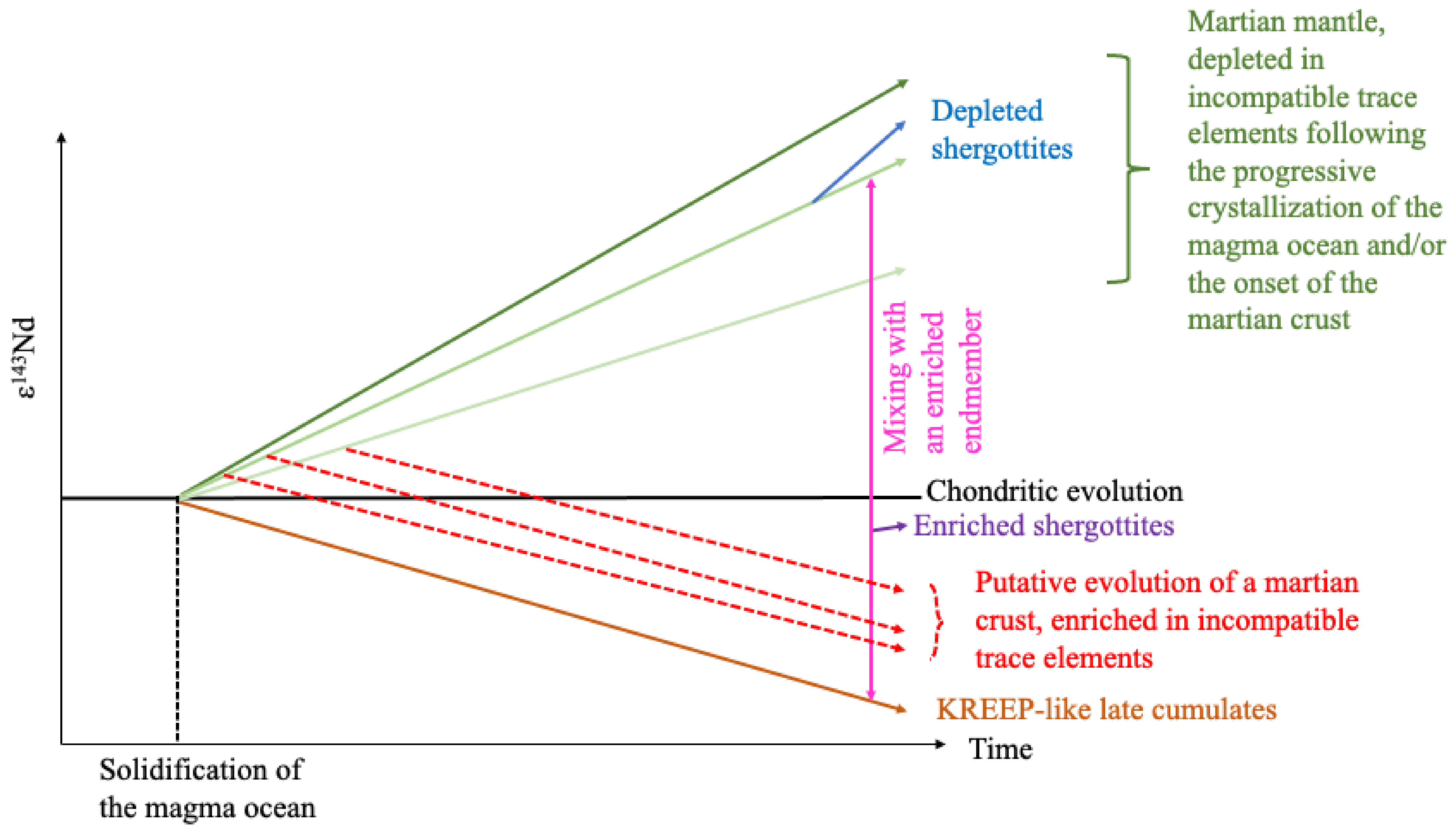

Martian mantle, depleted in incompatible trace elements following the progressive crystallization of the magma ocean and/or the onset of the martian crust
Depleted shergottites
Mixing with an enriched endmember
ε143Nd
Chondritic evolution
Enriched shergottites
Putative evolution of a martian crust, enriched in incompatible trace elements
KREEP-like late cumulates
Time
Solidification of the magma ocean

Figure 17.

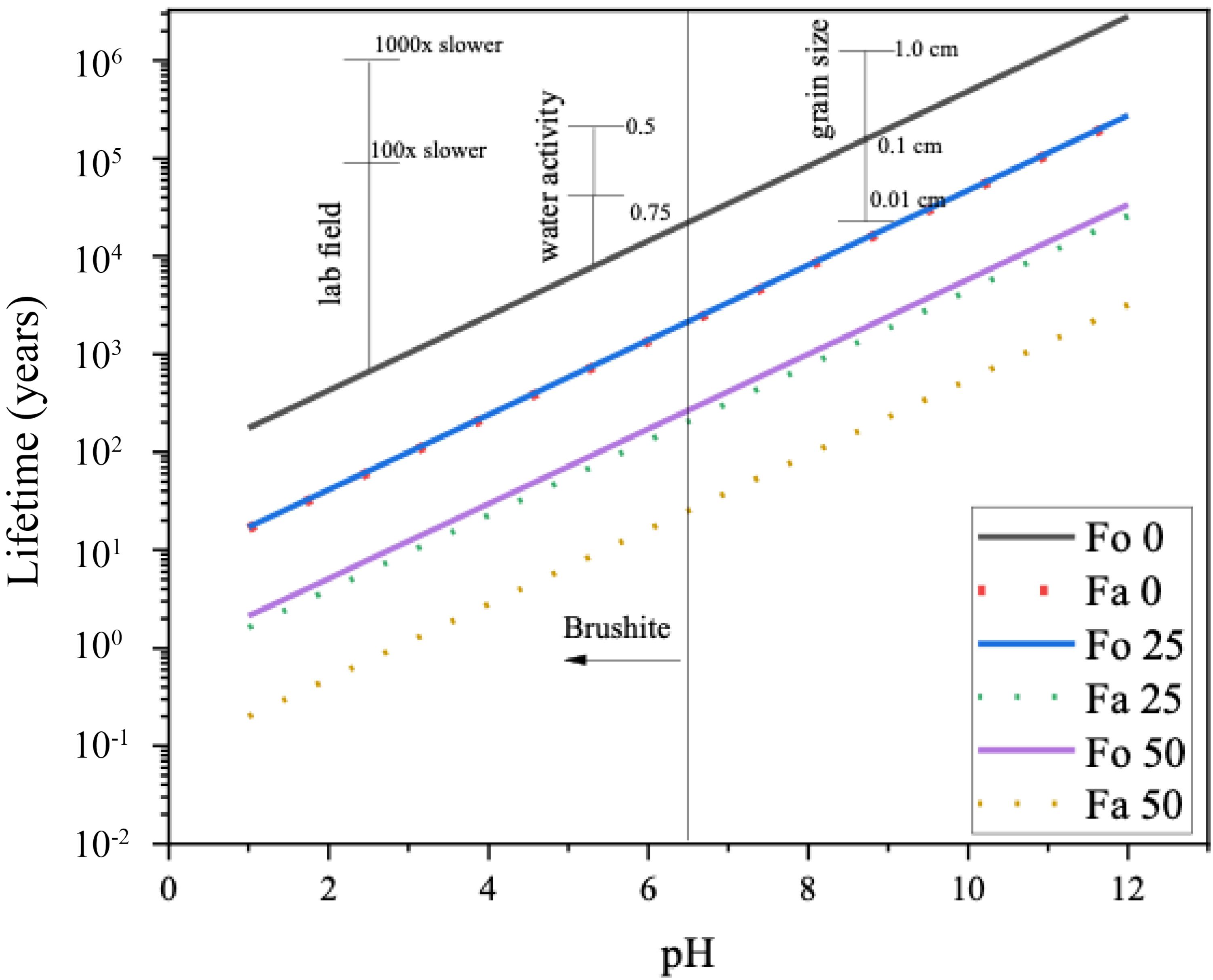

Lifetime (years)
pH
1000x slower
100x slower
lab field
water activity
0.5
0.75
grain size
1.0 cm
0.1 cm
0.01 cm
Brushite
Fo 0
Fa 0
Fo 25
Fa 25
Fo 50
Fa 50

Table 1. STOP list for Nominal Sampling Sol Path

Instrument	ZCAM	WATSON	WATSON	SHERLOC	PIXL	ZCAM	SCAM	WATSON	SCAM	ZCAM
Nominal Sol #	S-6	S-4 and S-3	S-3	S-3	S-3	S-2	S-2	S+1	S+1	S+1
Target	Workspace, includes both abrasion and coring targets	Abraded site	Coring targets	Abraded site, co-registered with PIXL	Abraded site, co-registered with WATSON, SHERLOC	Abraded site	Abraded site	Borehole #1	Borehole #1, Tailings/ Inner Wall	Borehole #1 Tailings
Rationale	Workspace Documentation	Rock texture documentation; for close approach	Coring target documentation (pre-drill), each core site for paired samples		Lithology, chemistry, and mineralogy documentation	Required to support SCAM observations	Lithology documentation	Borehole documentation, only 1 borehole imaging for paired samples	Rock borehole/tailings chemistry and mineralogy	Chemistry and mineralogy

S=sol that first core is collected. Second core collected following S+1 Borehole and Tailings observations and has no additional STOP list observations.

Table 2. Perseverance Crater Floor core characteristics

Core Name(s)	**Formation**	**Member**	**Outcrop**	**Abrasion**	**Rock Type**	**Lat., Lon., Elev.**	**Length (cm)**	**Headspace Gas (mol)***	**Sol & Time Sealed**
Roubion	Máaz	Roubion	Roubion	Guillaumes	Igneous basalt	18.42769° 77.45165° -2585.0 m	0 (disaggregated)	$4.9x10^{-6}$	SOL-0164M14:12:47.041
Montdenier Montagnac	Máaz	Rochette	Rochette	Bellegarde	Igneous basalt	18.43074° 77.44437° -2574.6 m	59.6 mm 61.5 mm	$1.2x10^{-6}$ $1.3x10^{-6}$	SOL-0190M12:29:34.349 SOL-0196M15:53:23.786
Salette Coulettes	Séítah	Bastide	Brac	Dourbes	Ultramafic cumulate	77.44301° 18.43397° –2569.2 m	62.9 mm 33.5 mm	$1.1x10^{-6}$ $2.5x10^{-6}$	SOL-0262M15:30:24.958 SOL-0271M15:25:59.868
Robine Malay	Séítah	Issole	Issole	Quartier	Ultramafic cumulate	77.44133° 18.43264° –2574.3 m	60.8 mm 30.7 mm	$1.1x10^{-6}$ $2.7x10^{-6}$	SOL-0295M15:32:36.230 SOL-0337M14:58:24.024
Hahonih Atsah	Máaz	Ch'ał	Sid	Alfalfa	Igneous andesite	77.45242° 18.44386° -2568.3 m	65.5 mm 60.0 mm	$1.0x10^{-6}$ $1.3x10^{-6}$	SOL-0371M14:53:54.458 SOL-0377M13:58:03.427

*In order to characterize the gas content of the tube and the environment to which solid samples were most recently exposed, a suite of atmospheric measurements are made to supplement the "STOP" list activities (see Appendix VII).

Witness tube (M2020-109-1 WB1) sealed 16:25:55 LMST, Sol 120, Ls 61.4, Lat. 18.43907°, Lon. 77.44940°, Elev. -2568.073 m

Table 3. Summary of Crater Floor sample characteristics

Sample	**Lithologic Description**	**Petrologic Description**	**Primary Mineralogy**	**Secondary Mineralogy**	**Organic Materials**	**Key Returned Sample Science Rationale**
Roubion	Polygonal, low-lying, granular-weathering "pavers" in lower elevation Máaz fm.	~0.5-1.0 mm evenly sized grains, and holes, possibly secondary cavity-filled or primary mineral replacement	Fe-rich augitic pyroxene (possible second mafic phase), plagioclase, Fe-Cr-Ti oxides (PIXL)	Fe/Mg-phyllosilicates (SuperCam-VISIR, SuperCam-Raman) Ca/Mg-sulfate (PIXL, SHERLOC) halides (PIXL) perchlorate (PIXL, SHERLOC)	One- and two or more-ring aromatic molecules	*Atmosphere:* modern composition & weathering agents
Montdenier & Montagnac	Variably massive to layered to pitted resistant cap rocks along Artuby ridge	~0.2-0.5 mm evenly sized grains, possibly secondary cavity-filled or primary mineral replacement	Fe-rich augitic pyroxene (possible second mafic phase), plagioclase, Fe-Cr-Ti oxides (PIXL)	Fe/Mg-phyllosilicates (SuperCam-VISIR) Ca/Mg-sulfate (PIXL, SHERLOC) halides (PIXL) perchlorate (PIXL), perchlorate or phosphate (SHERLOC), Na-perchlorate (SuperCam-Raman) silicate (SHERLOC)	Mix of organic compounds or a single heterocyclic compound; One- and two or more-ring aromatic molecules	*Igneous Petrogenesis:* elemental and isotopic composition of crustal ± mantle melts & emplacement mechanisms *Aqueous Alteration*: secondary mineralogy & weathering history *Geochronology*: timing constraints on crater and regional geology Paleomagnetism: timing of planetary dynamo *Astrobiology:* salt minerals relate to potentially habitable conditions
Salette & Coulettes	Layered rocks comprising middle-lower part of Martre outcrop	1-3.5 mm olivine-rich cumulate	Olivine intercumlate pyyroxene (PIXL, SHERLOC)	Fe/Mg-phyllosilicates (SuperCam-VISIR, PIXL) Ca/Mg-sulfate (PIXL, SHERLOC, SCAM?) carbonate (SHERLOC) ferric oxide (WATSON-ACI, Mastcam-Z) perchlorate (PIXL), perchlorate or phosphate (SHERLOC), silicate (SHERLOC).	Two or more-ring aromatic molecules	*Igneous Petrogenesis: elemental and isotopic composition of crustal ± mantle melts & emplacement mechanisms* *Aqueous Alteration*: secondary mineralogy and weathering history Geochronology: age relationship with Máaz fm. *Paleomagnetism*: timing of planetary dynamo *Astrobiology:* carbonate and salt minerals relate to potentially habitable conditions
Robine & Malay	Layered rocks comprising middle-lower part of Martre outcrop	1-3.5 mm olivine-rich cumulate	Olivine intercumlate pyyroxene (PIXL), olivine (SHERLOC)	Fe/Mg-phyllosilicates (SuperCam-VISIR), Ca/Mg-sulfate (PIXL, SHERLOC) Fe-(hydr)oxides (WATSON-ACI, Mastcam-Z) Mg/Ca/Fe-carbonate (SuperCam-VISIR, SHERLOC) perchlorate or phosphate (SHERLOC), silicate (SHERLOC), carbonate (SHERLOC)	Mix of organic compounds or a single heterocyclic compound; Two or more-ring aromatic molecules	*Igneous Petrogenesis: elemental and isotopic composition of crustal ± mantle melts & emplacement mechanisms* *Aqueous Alteration:* secondary mineralogy and weathering history *Geochronology*: age relationship with Máaz fm. *Paleomagnetism:* timing of planetary dynamo *Astrobiology:* carbonate and salt minerals relate to potentially habitable conditions
Hahonih & Atsah	Massive, blocky, "hummocky" rocks found predominantly east of OEB	~0.5-3.5 mm porphryitic texture, relatively large euhedral feldspars, a few mm long, within a finer-grained (~0.5-1.0 mm) matrix	Fe-rich augitic pyroxene (possible second mafic phase), plagioclase, Fe-Cr-Ti oxides (PIXL), pyroxene (SHERLOC)	Fe-phyllosilicates (SuperCam-VISIR, PIXL), Mg-OH (SuperCam-VISIR), Al-phyllosilicate? - SuperCam-VISIR), ferric oxide (Mastcam-Z, SuperCam-LIBS, WATSON-ACI?), akaganeite (SuperCam-VISIR?), carbonate (SHERLOC), perchlorate or phosphate (SHERLOC), silicate (SHERLOC)	One- and two or more- ring aromatic molecules	*Igneous Petrogenesis: elemental and isotopic composition of crustal ± mantle melts & emplacement mechanisms* *Aqueous Alteration:* secondary mineralogy and weathering history *Geochronology:* stratigraphic constraint on age of Jezero delta & Mars crater calibration defined by uppermost surface of Máaz fm. *Paleomagnetism:* timing of planetary dynamo

Table 4. Bulk sum averages for PIXL scan areas

	Guillaumes (sol 167)			Bellegarde (sol 187)			Dourbes (sol 257)			Dourbes2 (sol 270)			Quartier1 (sol 294)			Quartier2 (sol 301)			Montpezat2 (sol 350)			Alfalfa (sol 369)		
	wt %	**1s error (wt%)**	**std**	**wt %**	**1s error (wt%)**	**std**	**wt %**	**1s error (wt%)**	**std**	**wt %**	**1s error (wt%)**	**std**	**wt %**	**1s error (wt%)**	**std**	**wt %**	**1s error (wt%)**	**std**	**wt %**	**1s error (wt%)**	**std**	**wt %**	**1s error (wt%)**	**std**
Na_2O	5.71	0.72	3.10	4.76	0.56	1.59	1.70	0.56	0.38	2.24	0.54	2.21	2.27	0.77	1.39	1.93	0.60	1.21	3.40	0.97	1.70	5.28	0.66	2.29
MgO	2.63	0.56	1.08	2.19	0.64	1.16	19.73	0.99	2.14	18.53	0.93	1.97	15.86	0.80	3.80	13.13	0.66	2.68	6.15	0.31	1.75	0.76	0.32	0.52
Al_2O_3	7.56	0.38	3.02	6.96	0.35	3.62	1.96	0.51	5.16	3.08	0.56	5.96	1.50	0.44	1.87	2.35	0.55	1.88	5.82	0.29	2.77	11.88	0.60	5.69
SiO_2	38.28	1.92	7.12	43.78	2.19	10.65	40.36	2.02	3.11	38.08	1.91	4.10	34.13	1.71	14.70	41.36	2.07	7.30	44.95	2.25	6.16	57.16	2.86	11.32
P_2O_5	1.64	0.54	1.41	2.75	0.56	2.46	0.29	0.25	8.83	0.74	0.29	9.20	0.42	0.24	1.76	0.29	0.25	0.57	1.09	0.43	1.45	0.98	0.37	1.51
SO_3	2.69	0.56	2.90	3.21	0.56	5.84	0.52	0.21	1.13	1.15	0.36	3.33	8.61	0.46	11.60	1.70	0.47	1.81	0.93	0.35	0.47	1.96	0.51	1.16
Cl	3.50	0.54	4.14	1.52	0.44	0.84	0.62	0.34	1.81	0.74	0.25	0.74	1.15	0.48	0.85	0.96	0.36	0.60	0.79	0.27	0.71	1.05	0.34	1.51
K_2O	0.75	0.26	0.47	1.06	0.34	0.76	0.12	0.14	0.90	0.26	0.23	0.56	0.12	0.14	0.33	0.21	0.21	0.40	0.73	0.25	0.69	1.93	0.51	1.28
CaO	7.80	0.39	3.86	7.64	0.38	4.34	3.89	0.49	5.93	1.58	0.45	1.26	2.75	0.56	4.48	6.09	0.31	5.92	9.08	0.46	4.97	4.42	0.40	3.42
TiO_2	1.48	0.54	2.27	2.49	0.58	2.18	0.39	0.24	1.08	0.32	0.23	2.91	0.25	0.23	0.79	1.01	0.33	2.29	1.06	0.42	2.03	0.68	0.29	1.61
Cr_2O^3	0.03	0.06	0.07	0.01	0.03	0.02	0.30	0.25	1.33	0.22	0.21	1.03	0.05	0.06	0.33	0.30	0.24	1.25	0.07	0.09	0.16	0.02	0.05	0.02
MnO	0.47	0.20	0.37	0.44	0.23	0.21	0.73	0.31	0.28	0.62	0.22	0.23	0.70	0.24	0.28	0.59	0.24	0.23	0.52	0.21	0.31	0.32	0.25	0.38
FeO-T	18.76	0.94	10.94	23.26	1.16	11.27	30.01	1.50	10.48	30.04	1.50	10.12	30.16	1.51	13.56	26.35	1.32	10.95	20.86	1.04	12.31	11.34	0.57	13.66

Journal of Geophysical Research--Planets

Supporting Information for

Samples Collected from the Floor of Jezero Crater with the Mars 2020 Perseverance Rover

J. I. Simon[1*], K. Hickman-Lewis[2,3], B. A. Cohen[4], L.E. Mayhew[5], D.L. Shuster[6], V. Debaille[7], E. M. Hausrath[8], B.P. Weiss[9], T. Bosak[9], M.-P. Zorzano[10], H. E. F. Amundsen[11], L.W. Beegle[12]†, J.F. Bell III[13], K. C. Benison[14], E. L. Berger[15], O. Beyssac[16], A.J. Brown[17], F. Calef[12], T. M. Casademont[11], B. Clark[18], E. Clavé[19], L. Crumpler[20], A. D. Czaja[21], A. G. Fairén[10,22], K. A. Farley[23], D. T. Flannery[24], T. Fornaro[25], O. Forni[26], F. Gómez[10], Y. Goreva[12], A. Gorin[7], K. P. Hand[12], S.-E. Hamran[11], J. Henneke[27], C. D. K. Herd[28], B. H. N. Horgan[29], J. R. Johnson[30], J. Joseph[31], R. E. Kronyak[12], J. M. Madariaga[32], J. N. Maki[12], L. Mandon[33], F. M. McCubbin[34], S. M. McLennan[35], R. C. Moeller[12], C. E. Newman[36], J. I. Núñez[29], A. C. Pascuzzo[37], D. A. Pedersen[28], G. Poggiali[38], P. Pinet[26], C. Quantin-Nataf[39], M. Rice[40], J. W. Rice Jr.[13], C. Royer[19], M. Schmidt[41], M. Sephton[42], S. Sharma[12], S. Siljeström[43], K. M. Stack[12], A. Steele[44], V. Z. Sun[12], A. Udry[8], S. VanBommel[45], M. Wadhwa[12,13], R. C. Wiens[29], A. J. Williams[46], K. H. Williford[47]

[1]Center for Isotope Cosmochemistry and Geochronology, Astromaterials Research and Exploration Science, NASA Johnson Space Center, Houston, TX, USA.
[2]The Natural History Museum, London, UK.
[3]Dipartimento BiGeA, Università di Bologna, Bologna, Italy.
[4]NASA Goddard Space Flight Center, Greenbelt, MD, USA.
[5]University of Colorado Boulder, Dept. of Geological Sciences, Boulder, CO, USA.
[6]University of California at Berkeley, Berkeley CA, USA.
[7]Universitélibre de Bruxelles, Belgium.
[8]Department of Geosciences, University of Nevada Las Vegas, Las Vegas, NV, USA.
[9]Dept. of Earth, Atmospheric, and Planetary Sciences, Massachusetts Institute of Technology, Cambridge, MA, USA.
[10]Centro de Astrobiologia (CAB), CSIC-INTA, Carretera de Ajalvir km 4, 28850 Torrejón de Ardoz, Madrid, Spain.
[11]University of Oslo, Norwegian Research Council, Oslo, Norway.
[12]Jet Propulsion Laboratory – California Institute of Technology, Pasadena, CA, USA.
[13]Arizona State University, Tempe, AZ, USA.
[14]West Virginia University, Morgantown, WV, USA.
[15]Texas State University – Jacobs JETS – NASA Johnsons Space Center, Houston, TX, USA.
[16] Institut de Minéralogie, Physique des Matériaux et Cosmochimie, CNRS UMR 7590, Sorbonne Université, Muséum National d'Histoire Naturelle, Paris, France.
[17]Plancius Research, Severna Park, MD, USA.
[18]Space Science Institute, Boulder, CO, USA.
[19]CELIA - Université de Bordeaux, CNRS, CEA, France.
[20]New Mexico Museum of Natural History & Science, Albuquerque, NM, USA.

[21]University of Cincinnati, Department of Geology, Cincinnati, OH, USA.
[22]Dept. Astronomy, Cornell University, Ithaca, NY, USA.
[23]California Institute of Technology, Pasadena, CA, USA.
[24]Queensland University of Technology, Brisbane, Australia.
[25]INAF-Astrophysical Observatory of Arcetri, Largo E. Fermi 5, 50125 Florence, Italy.
[26]Institut de Recherche en Astrophysique et Planétologie (IRAP), Université de Toulouse, CNRS, UPS, CNES, Toulouse, France.
[27]Danmarks Tekniske Universitet, National Space Institute, Lyngby, Denmark.
[28]Department of Earth and Atmospheric Sciences, University of Alberta, Edmonton, Canada.
[29]Department of Earth, Atmospheric, and Planetary Sciences, Purdue University, West Lafayette, IN, USA.
[30]Johns Hopkins University Applied Physics Laboratory, Laurel, MD, USA.
[31]Cornell University, Ithaca, NY, USA.
[32]Department of Analytical Chemistry, University of the Basque Country (UPV/EHU), 48940 Leioa, Spain.
[33]LESIA, Observatoire de Paris, Université PSL, CNRS, Sorbonne Université, Université de Paris, Meudon, France.
[34]Astromaterials Research and Exploration Science, NASA Johnson Space Center, Houston, TX, USA.
[35]Department of Geosciences, Stony Brook University, Stony Brook, USA.
[36]Aeolis Research, Chandler, AZ, USA.
[37]Malin Space Science Systems, San Diego, CA, USA.
[38]INAF-Astrophysical Observatory of Arcetri, Firenze, Italia, USA.
[39]Laboratoire de Géologie de Lyon, Université Lyon, Bâtiment Géode, Villeurbanne, France.
[40]Western Washington University, Bellingham, WA, USA.
[41]Department of Earth Sciences, Brock University, St. Catharines, ON, Canada.
[42]Department of Earth Science and Engineering, Imperial College London, London, UK.
[43]RISE Research Institutes of Sweden, Stockholm, Sweden.
[44]Earth and Planetary Laboratory, Carnegie Institution for Science, Washington D.C., USA.
[45]McDonnell Center for the Space Sciences, Department of Earth and Planetary Sciences, Washington University in St. Louis, St. Louis, MO, USA.
[46]Department of Geological Sciences, University of Florida, Gainesville, FL, USA.
[47]Blue Marble Space Institute of Science, Seattle, WA, USA.

* Corresponding author: Justin I. Simon (justin.i.simon@nasa.gov)
†formerly

Contents of this file

Supplemental Figures S2-10. Mastcam-Z anaglyph mosaics for sample outcrop targets and select geologic units.
Supplemental Figure S11. Geologic mapping of sampled outcrops.
Supplemental Figures S12-16. Autofocus and Context Images merged with PIXL X-ray maps.

Supplemental Table S1. WATSON image products table.
Supplemental Tables S2-6. SuperCam-LIBS data for Total Alkali versus Silica plots.

Introduction

This contribution includes a variety of geospatially located data, including context far-field and workspace images (Mastcam-Z, Figs. 3-7; Figs. S2-10 color anaglyphs, Fig. S11 context mapping, NASA PDS doi:10.17189/q3ts-c749), subsurface radar data (RIMFAX, Figs. 3-7, NASA PDS doi:10.17189/1522644), rock target close up images (WATSON, Figs. 8, 9, 12, and 13; Table S1, NASA PDS doi:10.17189/1522643), sample core images (CacheCam, Fig. 2, NASA PDS doi:10.17189/q3ts-c749), major element compositional laser ionization breakdown spectroscopy (SuperCam-LIBS, Fig. 11, Tables S2-6, NASA PDS doi:10.17189/1522646), X-ray fluorescence measurements that allow compositional mapping (PIXL, Figs. 9, 10, and 13; Figs. S12-16 distorted WATSON ACIs merged with X-ray fluorescence maps of SiO_2, Al_2O_3, and SO_3 abundance and distribution; and bulk sum analyses, Table 4, NASA PDS doi:10.17189/1522645), hydration and alteration phase identification by visible and infrared spectroscopy (SuperCam-VISIR, Fig. 14, NASA PDS doi:10.17189/1522646), mineral and organic compound identification and mapping (SHERLOC-Raman/Fluorescence, Fig. 15, NASA PDS doi:10.17189/1522643), and atmospheric conditions at the time of sampling Roubion, the atmospheric sample (MEDA, Fig. S1, NASA PDS doi:10.17189/1522849).

Text S1. Headspace gas volume.

The estimated amount of headspace gas in moles, n, is computed from the ideal gas law and assuming the rover ambient temperature (T) at the time of sealing and the ambient pressure (P) as follows: $n = P (V_{tube} – V_{rock})/ RT$ where R is the gas constant, where V_{tube} is 12 cm^3 and V_{rock} is derived from the penetration depth of the volume probe, a rod inserted into the tube after sample acquisition. A full-length core is typically 6 cm long, although some samples have shorter lengths. The volume is computed from the estimated length of the sample multiplied by an assumed cylindrical cross section corresponding to the coring bit inner diameter d = 13.4 mm. However, void spaces – filled by gas- between core fragments may exist, and thus, the true sample and gas volume may differ from these estimates.

The estimated Rover-Ambient Pressure and Temperature are obtained from MEDA. MEDA measurements were not included within the STOP list as a requirement to be implemented on the sampling and sealing sols, however MEDA measurements have been taken as a background measurement at periodic hourly intervals, every sol (see Fig. S1). When MEDA measurements were not acquired on the same sol as sample sealing (often the case given energy limitations), the average values of pressure and

temperature are estimated from the closest sol or sols. The reported temperature is the minimum of MEDA ATS 4 and 5, the sensors located 0.84 m above the surface. The Sample tubes are sealed in the Adaptive Caching Assembly (ACA). Mechanisms in this subsystem are actively heated, so sealing occurs at temperatures higher than ambient conditions around the rover. The actual temperature of the gas upon sealing is difficult to estimate because the ACA is substantially warmer than the rover surroundings, typically by almost 100 K. For consistency, we assume rover ambient temperature in this calculation, recognizing that it is an upper limit of the number of moles. A lower limit would be obtained by using the reported ACA temperature in the above equation, which is typically 40°C -35°C.

Figure S1. **Atmospheric pressure and temperature plot for Roubion.**

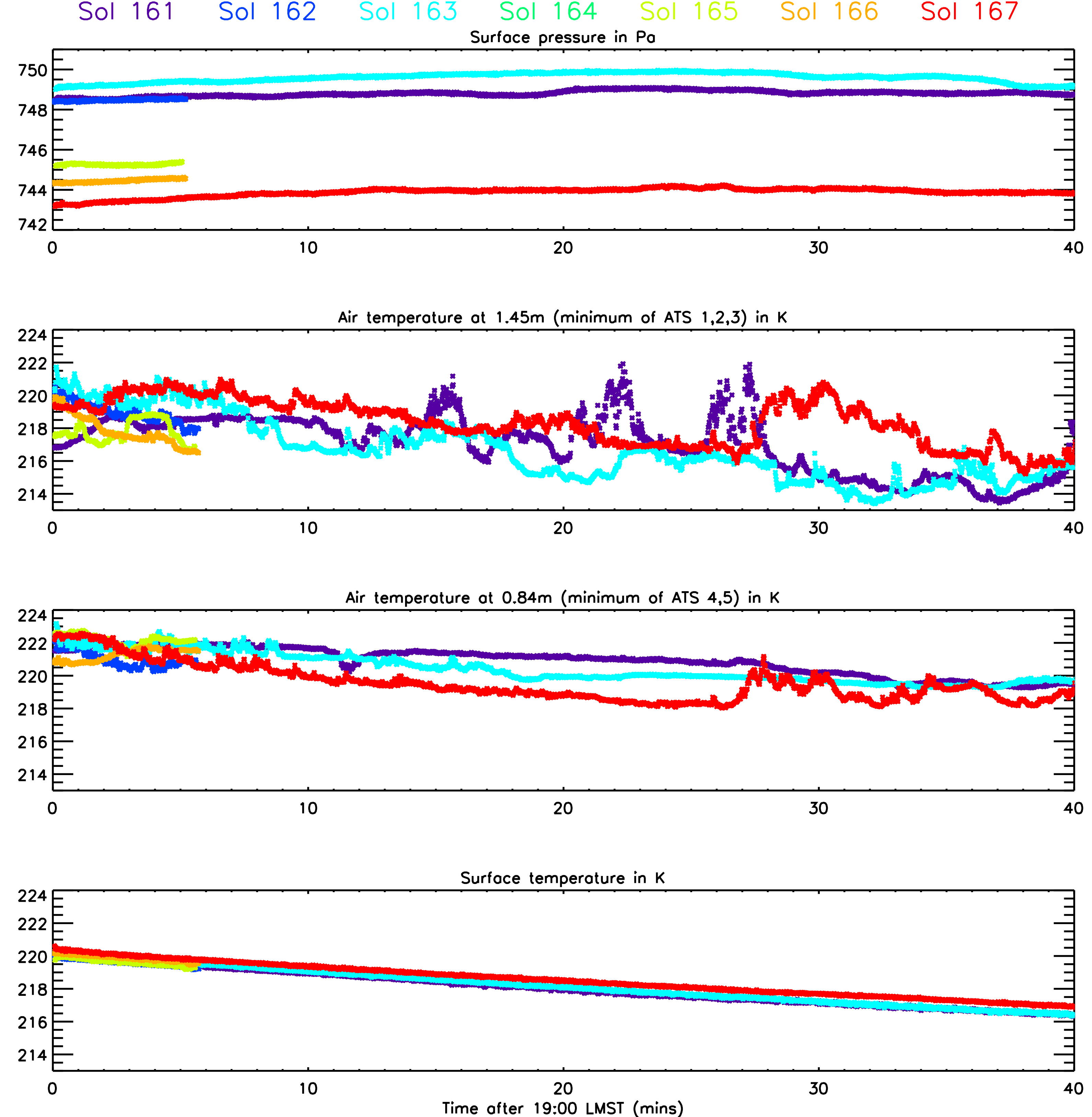

Sol 161 Sol 162 Sol 163 Sol 164 Sol 165 Sol 166 Sol 167
Surface pressure in Pa
Air temperature at 1.45m (minimum of ATS 1,2,3) in K
Air temperature at 0.84m (minimum of ATS 4,5) in K
Surface temperature in K
Time after 19:00 LMST (mins)

Figures S2-10. Mastcam-Z anaglyph mosaics for sample outcrop targets and select geologic units.

Stereoscopic 3D “anaglyphs” can be viewed through “color-coded” “anaglyph glasses” to reveal an integrated stereoscopic view of the sample outcrop targets and select Jezero Crater floor units shown in Figure 3-7. These include images for: Brac, Issole, Rochette, Roubion, and Sid, as well as, outcrop targets and Bastide, Rochette, Roubion, and Ch’ał member units.

Brac

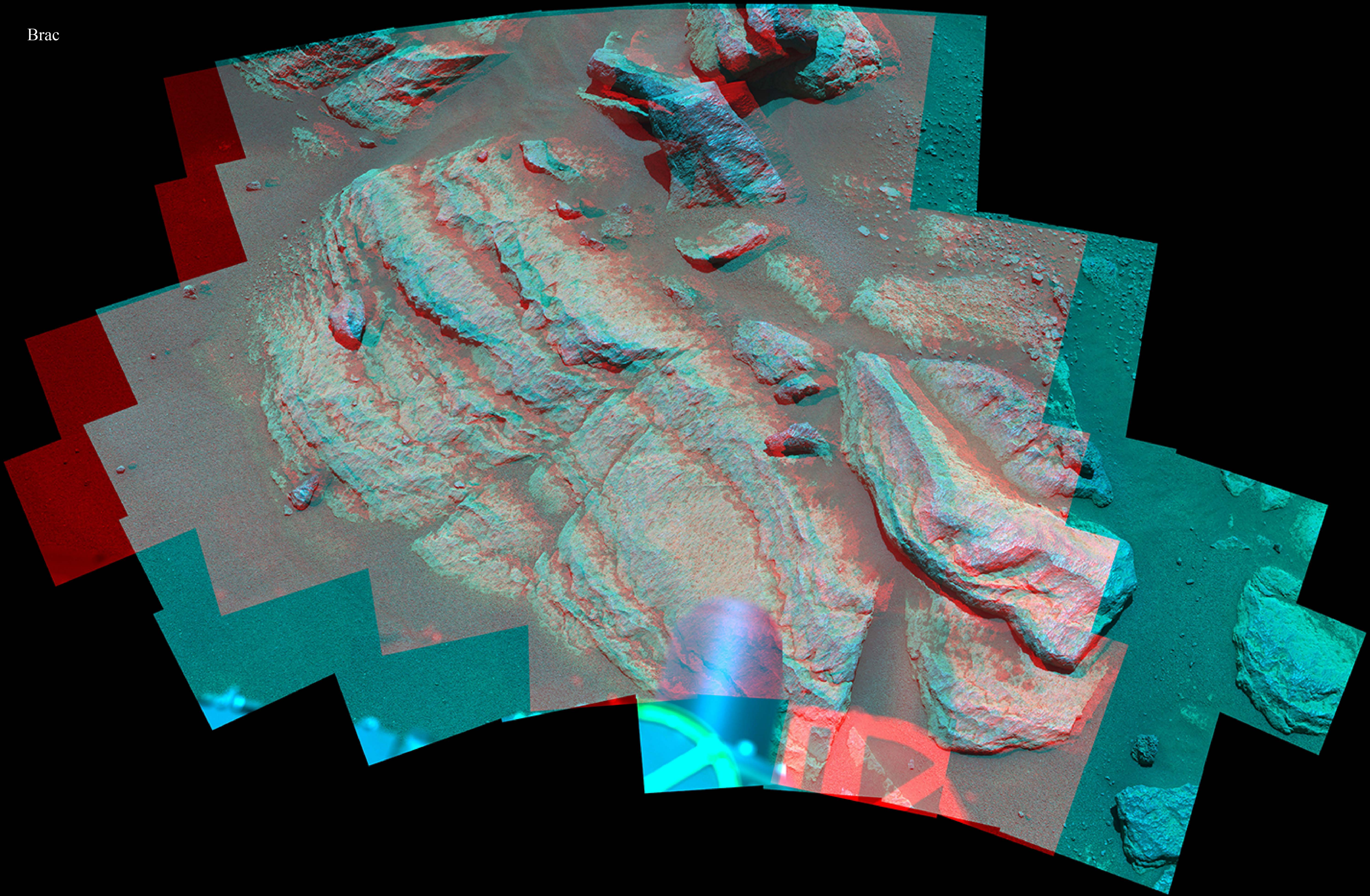

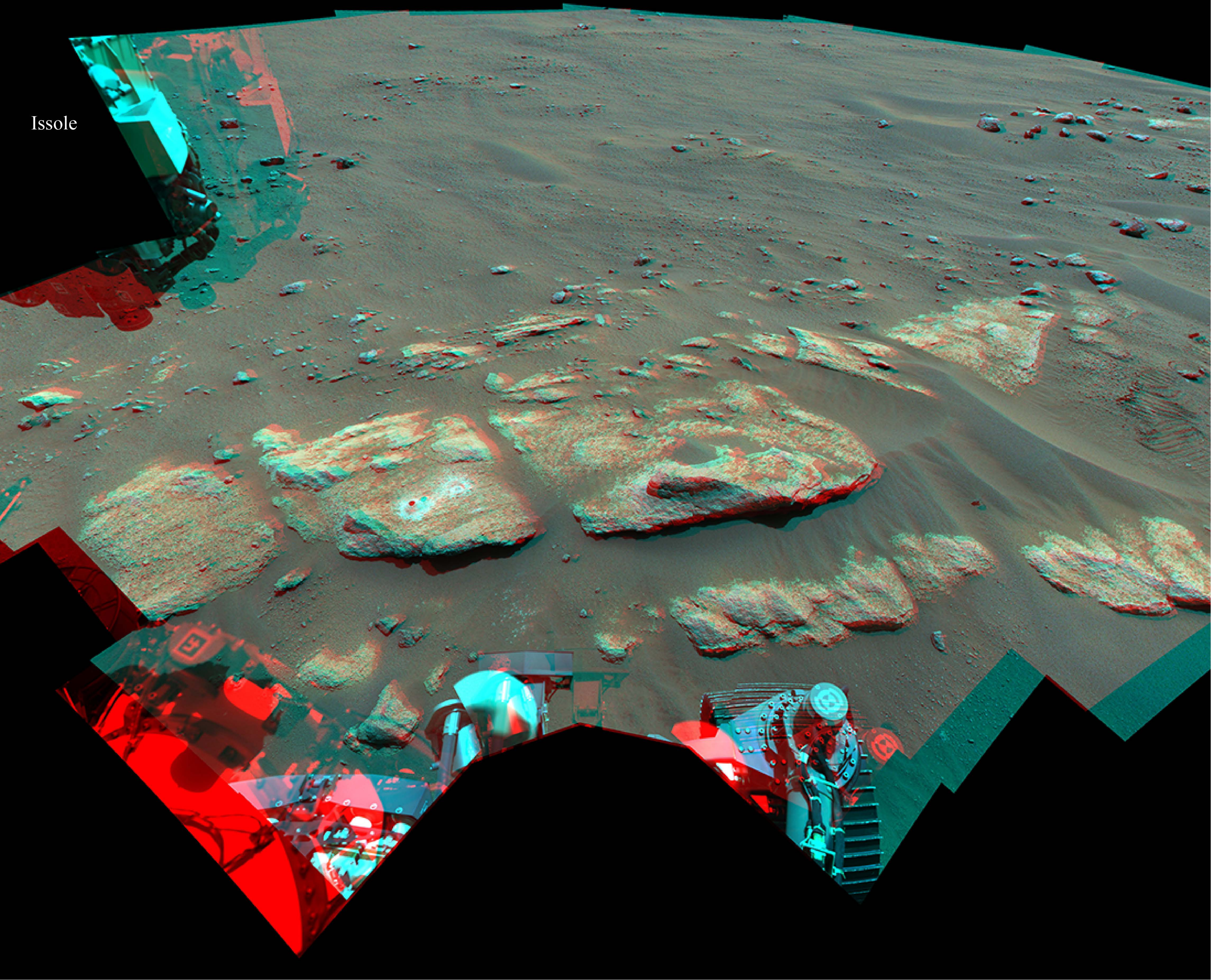
Issole

Rochette

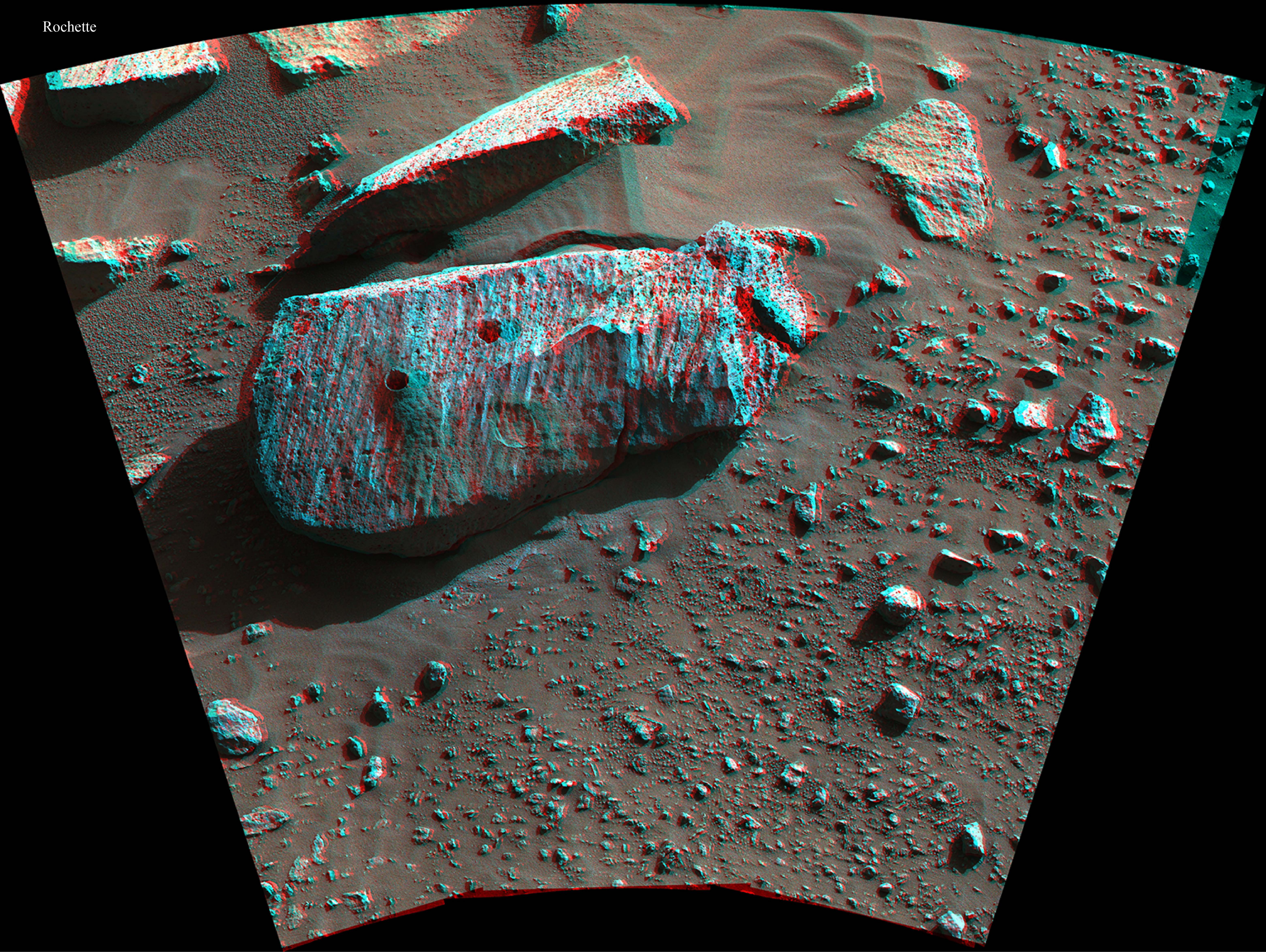

Roubion

Sid

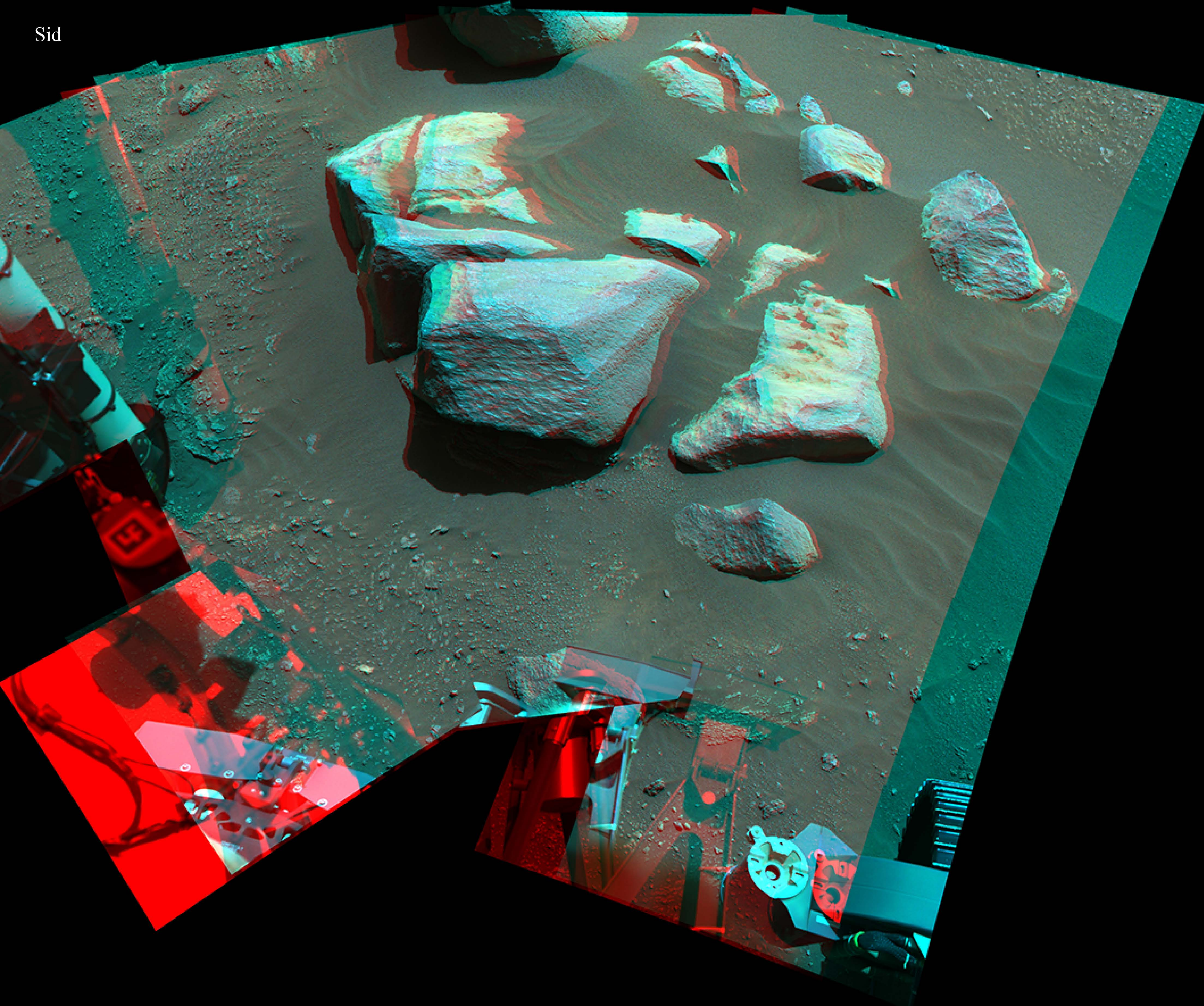

Bastide member

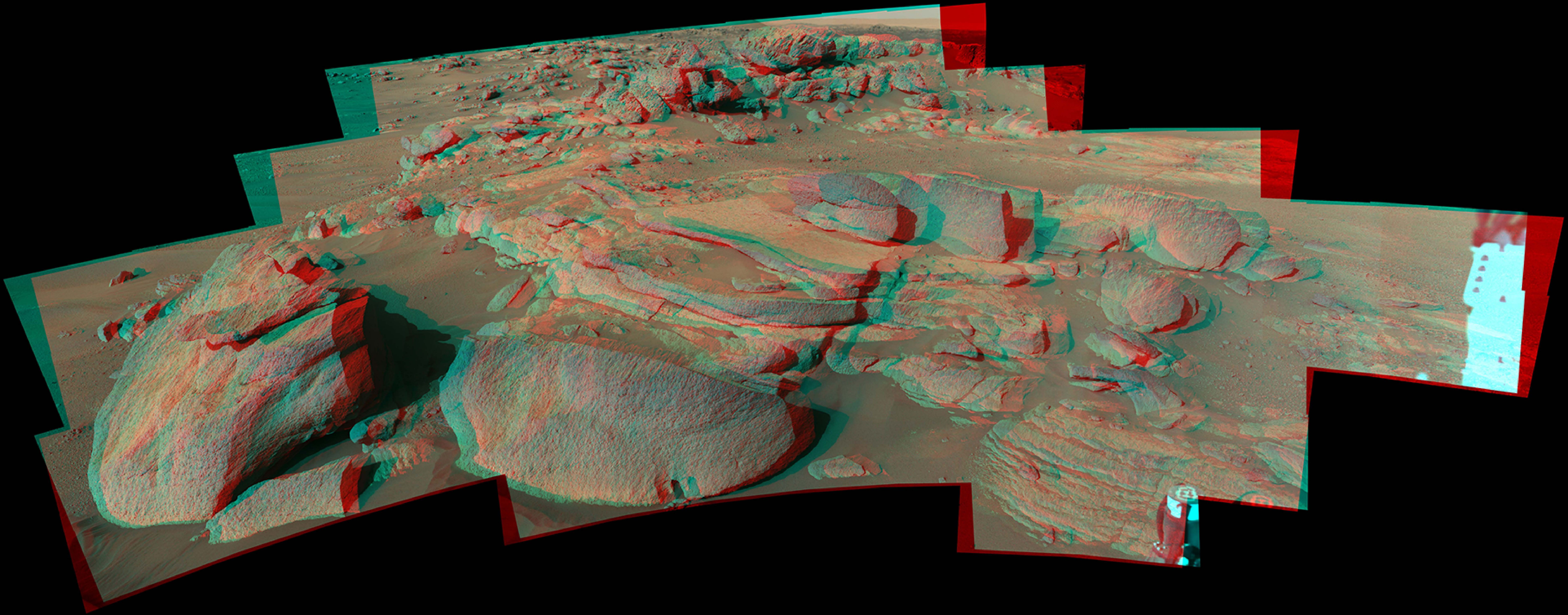

Rochette member

Roubion member

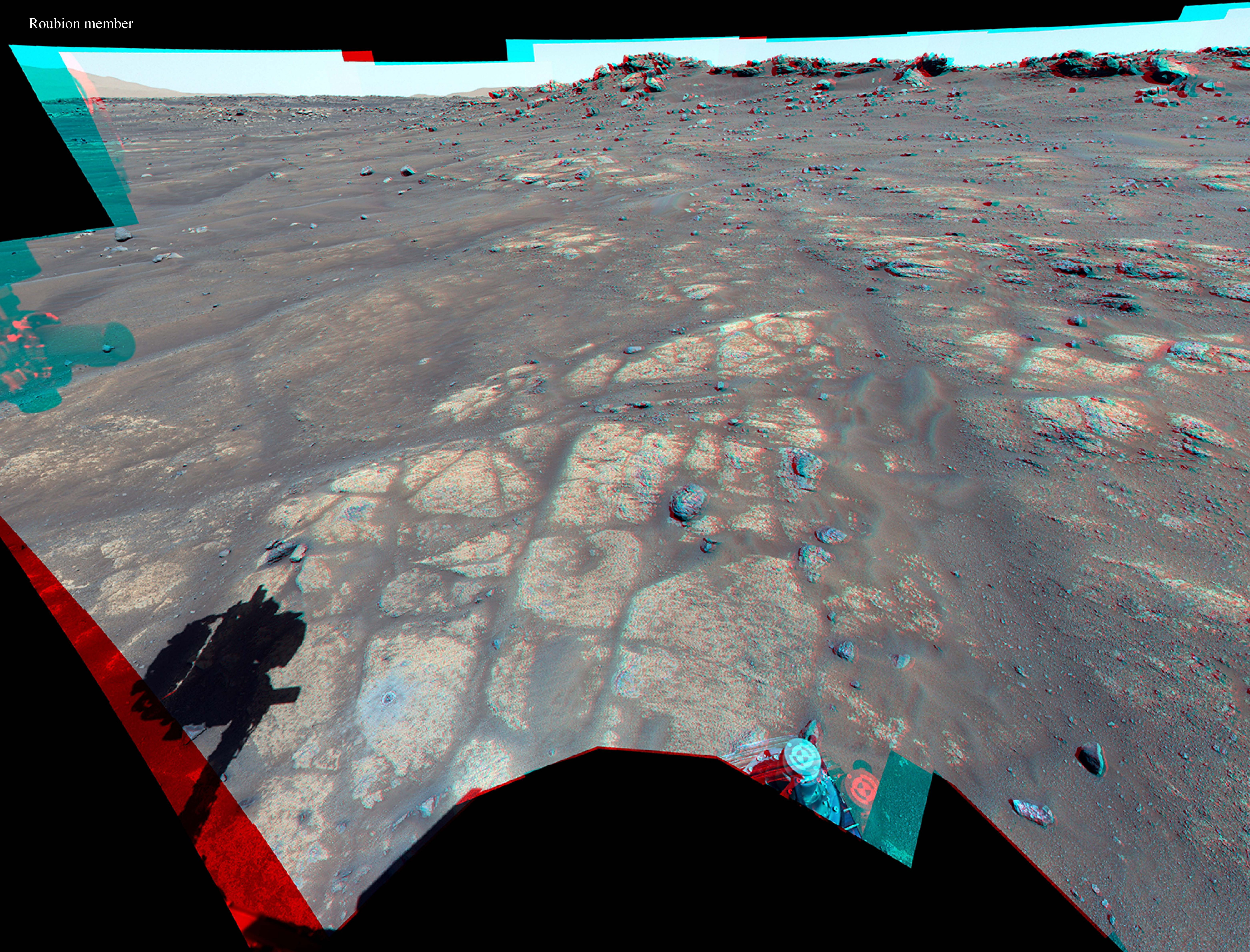

Ch'ał member

Figure S11. Geologic mapping of sampled outcrops.

***In situ* geologic context mapping (GXM, Crumpler et al. this volume) provide geologic context including the local extent of bedrock outcrops, stratigraphy, attitude, and structure from imaging and rover-based remote sensing, and the lithology based on in situ proximity science. Included here are subsections from the larger 120 m-wide map of Crumpler et al. (this volume), along the traverse from the perspectives of the Mars 2020/ Perseverance rover and Ingenuity helicopter that contain the sample outcrop targets. These include local maps for: Brac, Issole, Rochette, Roubion, and Sid outcrop sample targets.**

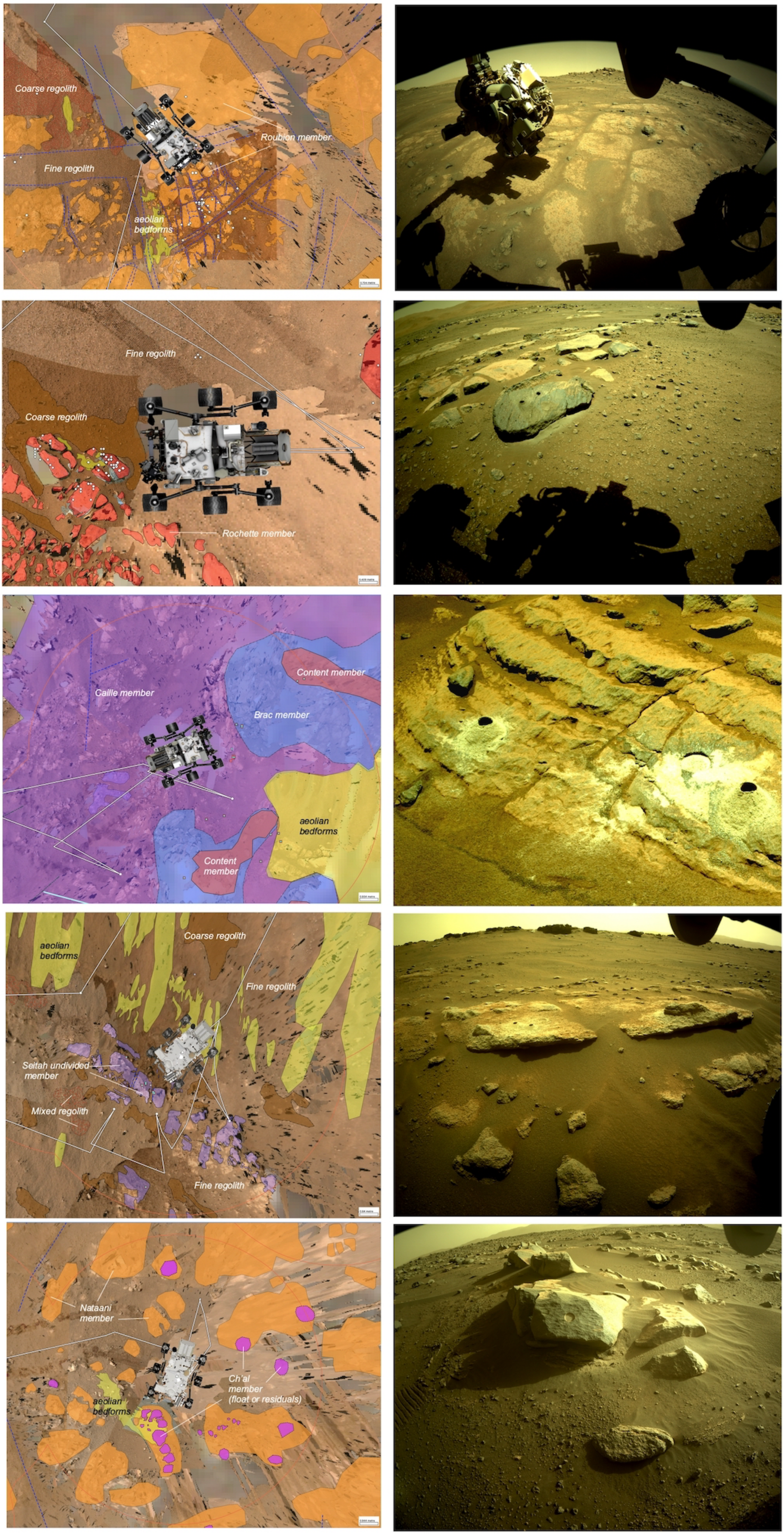
Coarse regolith
Roubion member
Fine regolith
aeolian bedforms
Fine regolith
Coarse regolith
Rochette member
Content member
Caille member
Brac member
aeolian bedforms
Content member
aeolian bedforms
Coarse regolith
Fine regolith
Seitah undivided member
Mixed regolith
Fine regolith
Nataani member
Ch'al member (float or residuals)
aeolian bedforms

Figures S12-16. Autofocus and Context Images merged with PIXL X-ray maps.

In order to accurately match each Autofocus and Context Image (ACI) to the PIXL X-ray compositional maps the ACI images must be slightly distorted. This distortion is not performed on the high-resolution ACI included in Figs. 9 and 12, but applied here where the ACI is merged with the individual PIXL composition maps of SO_3, SiO_2, and Al_2O_3 abundances. These include images that contain the PIXL scan areas within the Dorbes, Quartier, Guillaumes, Bellegarde, and Alfalfa abrasion sites.

Dourbes

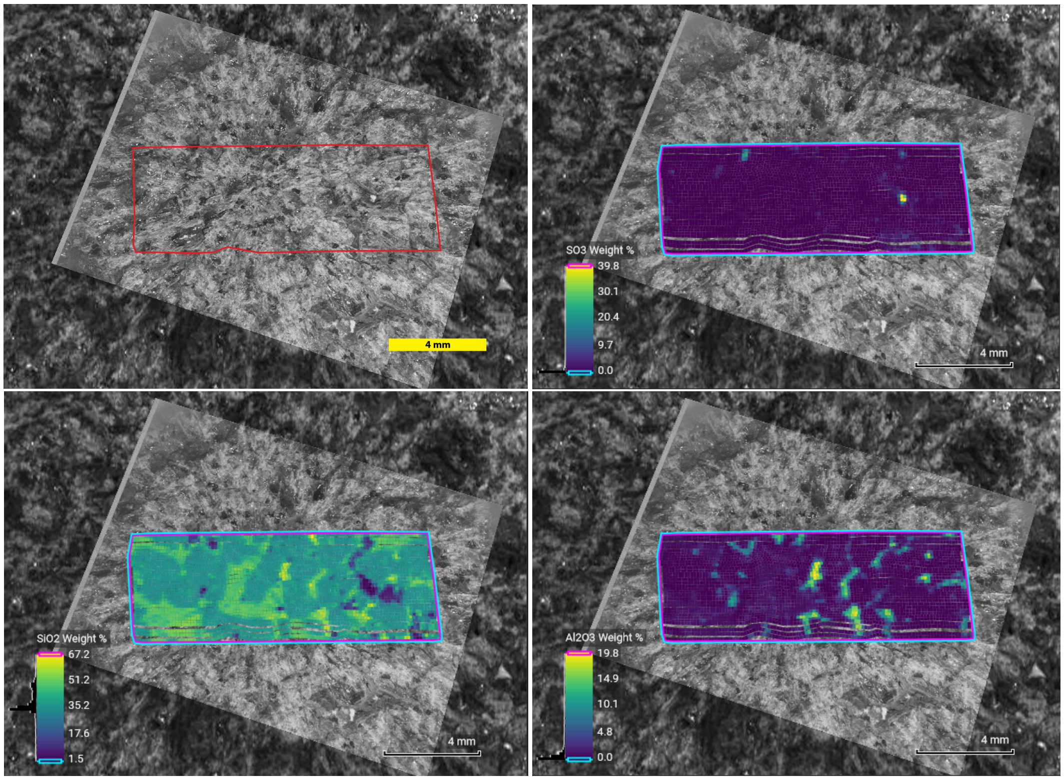

Quartier

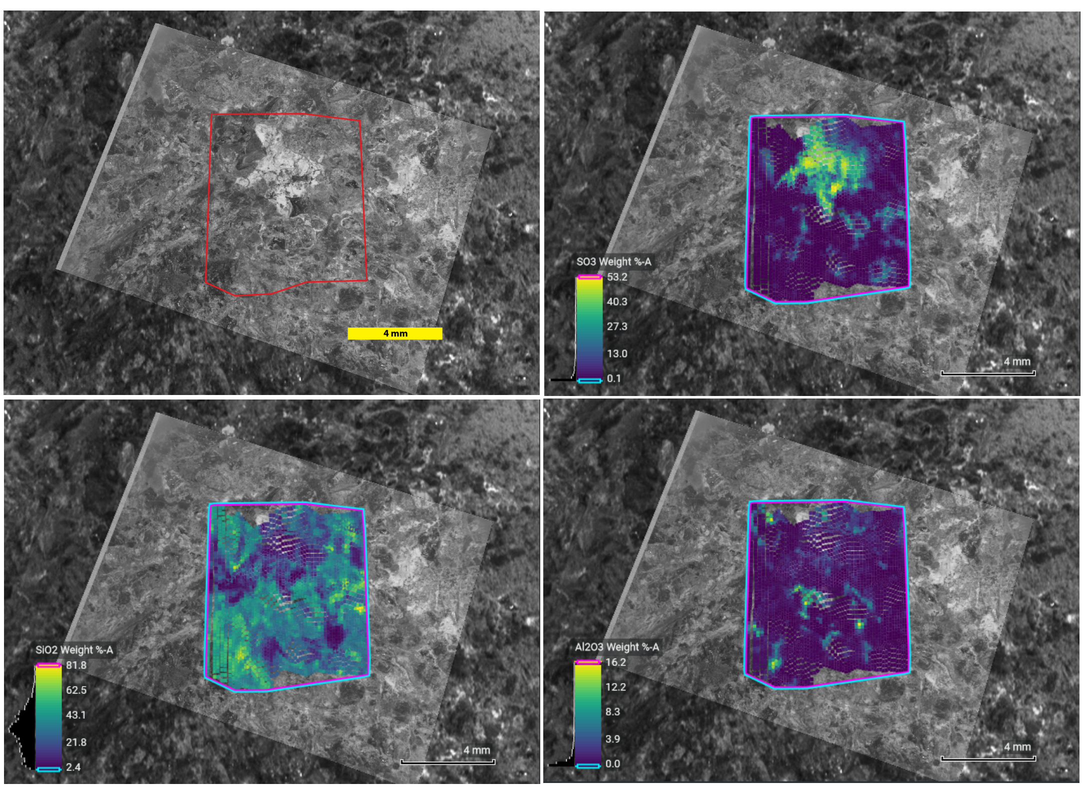

Guillaumes

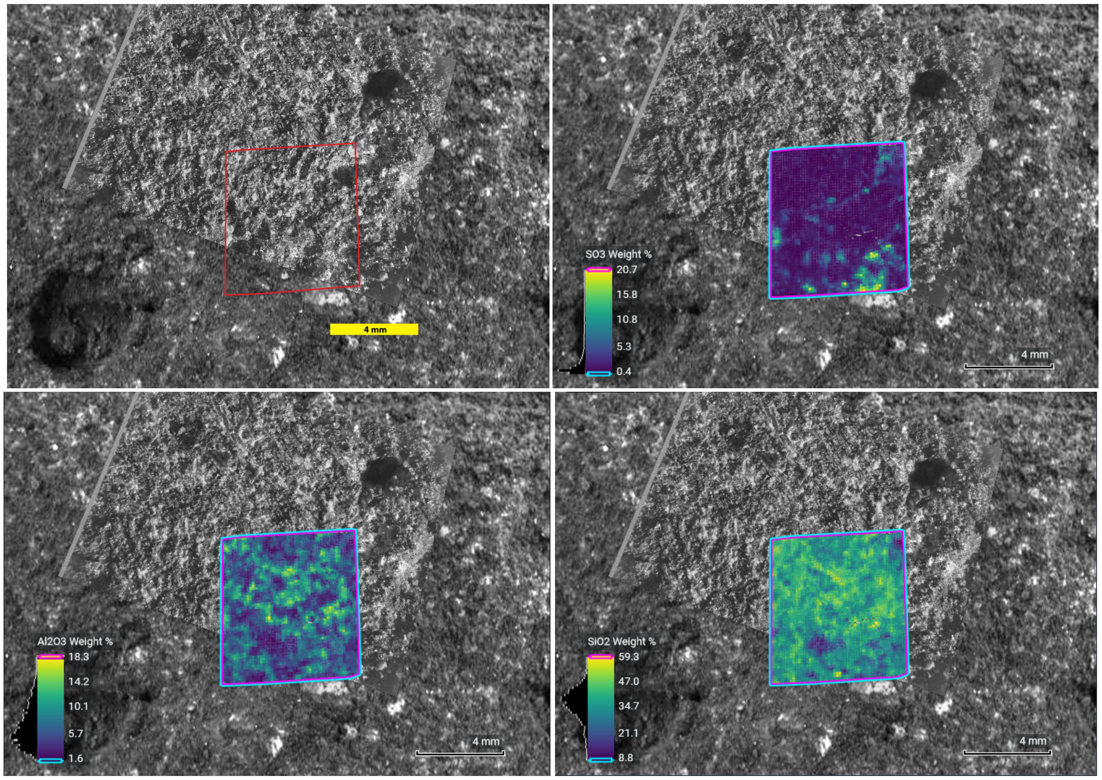

Bellegarde

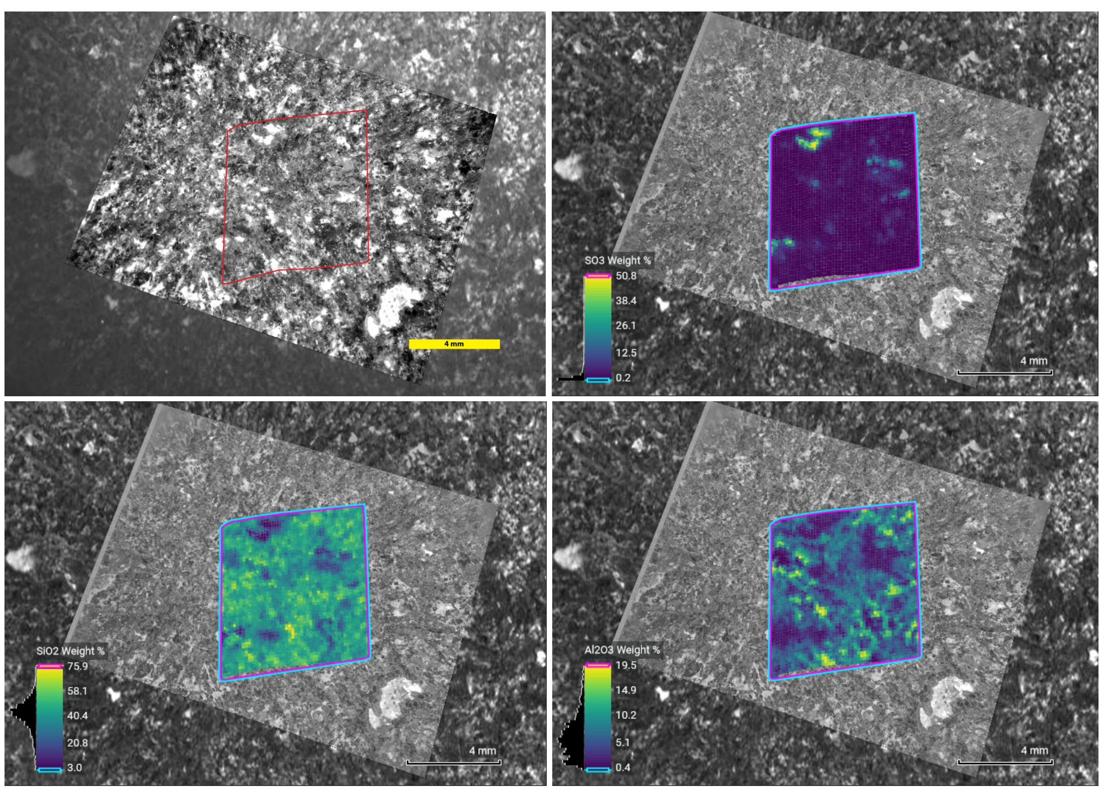

Alfalfa

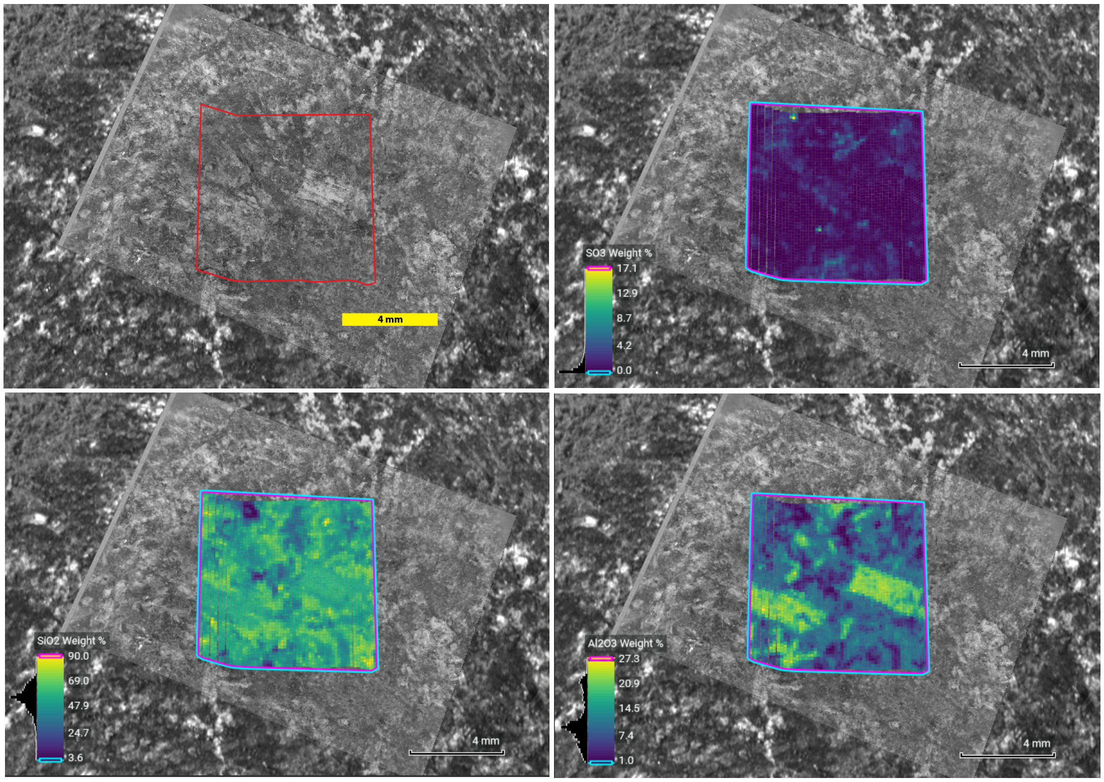
4 mm
SO3 Weight %
17.1
12.9
8.7
4.2
0.0
4 mm
SiO2 Weight %
90.0
69.0
47.9
24.7
3.6
4 mm
Al2O3 Weight %
27.3
20.9
14.5
7.4
1.0
4 mm

Table S1. WATSON image products table.

This supplemental table includes parameters pertinent to when, where, and how the WATSON images were obtained for the sample outcrop abrasion sites for Figs. 8, 9, and 12. These include images for: Dorbes, Quartier, Guillaumes, Bellegarde, and Alfalfa.

Fm.	Target Name	Latitude (˚N)	Longitude (˚E)	Figure	WATSON Source Image ID[a]	Camera Position/Acquisition Details	Range (cm)[b]	Pixel Scale (µm/pixel)	Solar Longitude (˚)		Imaging Sol	LTST	LMST	Solar Azimuth (˚from N)	Solar Elevation (˚above local horizon)	Illumination Conditions	Corresponding Raw, EDR, Products[c]
Séítah (Cf-f1/2	**Dourbes**	18.433964	77.443019	Fig 3a	SIF_0267_0690660838_722RAD_N0080000SRLC02504_0000LMJ01	Camera at ~25 cm standoff.	25.79 ± 0.8	99.5 ± 6.3	*early autumn*	129.94	267	17:42:45	17:16:05	286.9	9.9	low-angle sunlight and partially shadowed by abrasion patch rim.	SI_0267_0690660838_722ECM_N0080000SRLC02504_0000LMJ01
				Fig 4a	SI1_0269_0690819616_429RAD_N0080000SRLC00062_000095J02	Focus merge of an 8-image focus stack. Camera at ~4.7 cm standoff.	4.55 ± 0.1	23.4 ± 0.6		129.94	267	17:51:57	17:25:17	287.5	7.8	low-angle sunlight and partially shadowed by abrasion patch rim.	SI1_0267_0690661387_277ECM_N0080000SRLC00528_0000LUJ01**
	Quartier	18.432661	77.441373	Fig 3a	SIF_0292_0692874625_558RAD_N0090000SRLC02504_0000LUJ01	Camera at ~25 cm standoff.	26.13 ± 0.9	100.7 ± 6.3		142.49	292	16:16:15	15:48:43	277.4	28.2	sunlit and partially shadowed by abrasion patch rim.	SI_0292_0692874625_558ECM_N0090000SRLC02504_0000LUJ01
				Fig 4a	SI1_0293_0692961922_273RAD_N0090000SRLC00012_000095J01	Focus merge of an 8-image focus stack. Camera at ~4.3 cm standoff.	4.13 ± 0.1	21.8 ± 0.4		142.97	293	14:39:07	14:08:22	270.5	51.8	fully shadowed by rover.	SI1_0293_0692957385_726ECM_N0090000SRLC00479_0000LMJ01**
Máaz (Cf-fr)	**Alfalfa**	18.443901	77.452435	Fig 3b	SIF_0367_0699524997_886RAD_N0110108SRLC02504_0000LMJ01	~25 cm standoff	26.48 ± 0.9	101.9 6.4	*late autumn*	183.56	367	14:20:23	13:40:25	243.5	50.0	sunlit and partially shadowed by abrasion patch rim.	SI_0367_0699524997_886ECM_N0110108SRLC02504_0000LMJ01
				Fig 4b	SI1_0370_0699810275_101RAD_N0110108SRLC00036_000095J01	Focus merge of an 8-image focus stack. Camera at ~4.2 cm standoff.	4.0± 0.1	21.3 ± 0.4		185.34	370	15:14:22	14:34:19	251.6	37.8	sunlit.	SI1_0370_0699794625_511ECM_T0110108SRLC00451_000300J01**
	Guillaumes	18.427695	77.451650	Fig 3b	SIF_0160_0681145225_101RAD_N0060000SRLC08006_0000LMJ01	~25 cm standoff	26.8 ± 0.9	103.1 ± 6.5	*summer*	79.95	160	12:55:49	12:44:35	297.8	75.7	fully shadowed by rover.	SI_0160_0681145225_101ECM_N0060000SRLC08006_0000LMJ01
				Fig 4b	SI1_0161_0681260126_714RAD_N0060000SRLC00056_000095J02	Focus merge of an 8-image focus stack. Camera at ~4.2 cm standoff.	3.89 ± 0.1	20.9 ± 0.4		80.44	161	14:59:04	14:47:38	286.7	48.1	fully shadowed by rover.	SI1_0161_0681241566_730ECM_N0060000SRLC08008_0000LUJ01**
	Bellegarde	18.430739	77.444366	Fig 3b	SIF_0185_0683368050_667RAD_N0070000SRLC02502_0000LMJ01	~25 cm standoff	26.8 ± 0.9	103.1 ± 6.5		91.26	185	13:56:02	13:40:45	288.9	62.4	sunlit and partially shadowed by abrasion patch rim.	SI_0185_0683368050_667ECM_N0070000SRLC02502_0000LMJ01
				Fig 4b	SI1_0186_0683472720_546RAD_N0070000SRLC00005_000095J01	Focus merge of an 8-image focus stack. Camera at ~4.4 cm standoff.	4.21 ± 0.1	22.1 ± 0.5		91.76	186	16:32:07	16:16:40	289.4	27.2	sunlit and partially shadowed by rover and abrasion patch rim.	SI1_0186_0683466419_660ECM_N0070000SRLC00439_0000LUJ01**

[a] RAD products are reduced data records producted by JPL-IDSO's image processing pipeline. They have been radiometrically corrected and flat-fielded. They have not been photometrically corrected.

[b] Range is the distance between the camera lens and where the camera is focused on the target. It describes the distances implied by the presence of in-focus elements.

[c] For the focus merges images, the image metadata shown in this table is sourced from the 5th image(**) in the focus merge image's corresponding 8-image focus stack

Tables S2-6. SuperCam-LIBS data for Total Alkali versus Silica plots.

This supplemental data file includes the SiO_2, TiO_2, Al_2O_3, FeO_T, MgO, CaO, Na_2O and total wt.% values for the analyzed natural and abraded site sample outcrop targets. The values are those plotted on the TAS diagrams in Fig. 11. These data sets have been calibrated and filtered for data quality (i.e., <6.5 m distance, >1e14 signal intensity, and target focus), see Wiens et al. (2022).